Constructing realistic Szekeres models from initial and final data

Anthony Walters

Department of Mathematics and Applied Mathematics

University of Cape Town

Supervised by Prof. Charles Hellaby

Thesis submitted for the degree of

Master of Science

February 2012

Abstract

The Szekeres family of inhomogeneous solutions, which are defined by six arbitrary metric functions, offers a wide range of possibilities for modelling cosmic structure. Within this family, the quasispherical case is the best understood, and is interpreted as being an arrangement on non-concentric mass shells, each a density dipole. Here we present a model construction procedure for the quasispherical case using given data at initial and final times. Of the six arbitrary metric functions, the three which are common to both Szekeres and Lemaître-Tolman models are determined by the model construction procedure of Krasinski & Hellaby. For the remaining three functions, which are unique to Szekeres models, we derive exact analytic expressions in terms of more physically intuitive quantities - density profiles and dipole orientation angles. Using MATLAB, we implement the model construction procedure and simulate the time evolution.

Acknowledgements

I am most grateful to my supervisor, Prof. Charles Hellaby, for all his patience and careful guidance over the course of this project. To my parents and friends for their continuous support and encouragement. And, to the National Research Foundation and the National Astrophysics and Space Science Program, for their financial support.

Contents

List of Figures

List of Tables

LIST OF TABLES

1

Introduction

Einstein's theory of General Relativity (GR) is widely regarded within the scientific community to be the best current description of gravitational phenomena, having been confirmed by a wide range of observational tests [1, 2, 3, 4, 5, 6]. While this is not to say that it is necessarily a complete or fundamental theory of gravity, as is evident by the numerous attempts to modify it [7, 8, 9, 10, 11, 12], but rather, it does a good job of explaining, and in some cases predicting, observations rather elegantly. It is thus of great importance to fully understand it's behaviour, and one key method is to investigate exact solutions. In general, the Einstein Field Equations (EFEs) are a set of 10 partial differential equations which are very nonlinear, and so, difficult to solve. Typically a number of assumptions are made about the symmetries of the spacetime or the form of the metric, in order to reduce the complexity of the system. Of the thousands of exact solutions available in the literature [13], only a handful of these are physically realistic and can be reasonably applied to astrophysics and cosmology. Assumptions of isotropy together with the Copernican Principle (the assumption that we live in a non-special place in the Universe), point to the Freedmann-Lemaitre-Robertson-Walker (FLRW) geometry as being a good approximation to the behaviour of the Universe on large scales. And, in the mainstream of modern cosmology, almost all observations are analysed and interpreted within this framework.

The current view on structure formation is that particle creation within a period called 'inflation' is responsible for setting up the initial perturbations from which the structure we observe today has evolved. Inflation was originally proposed by Guth [14] in 1981 to solve the problems of initial conditions (flatness and horizon problems), although its

true merit is said to be setting up inhomogeneities in the Universe [15]. The theory posits that the early Universe underwent a period of accelerated expansion, during which quantum fluctuations in the inflaton field set up density perturbations. After inflation, modes which have not been 'frozen out' of causal contact begin to oscillate due to the competing forces of gravity and pressure, setting up a characteristic length scale. This process in the early Universe is referred to as the Acoustic Oscillations. Once the Universe is sufficiently cool, protons capture free electrons to form neutral hydrogen, thus allowing photons to free-stream away and leaving the dark matter and baryons clustered at that characteristic scale. With the absence of pressure, the perturbations begin to collapse under gravitational instability and go on to form cosmic structures, such as voids, walls, filaments, clusters of galaxies etc.

In the study of the evolution of cosmic structure, the standard formalisms which are used are either N-body simulations, for the post decoupling universe, or linear perturbation theory for earlier times. N-body simulations, describing the evolution of a large number of gravitationally interacting particles, are typically used to investigate the formation of non-linear structures, and, although they have done a good job of reproducing the filamentary structure of the universe observed by large scale galaxy surveys, they fall short of being a sufficiently good theory of structure formation and evolution. Firstly, they neglect pressure, and so are only applicable to the universe at times after recombination. And secondly, they are intrinsically non-relativistic - they use a Newtonian approximation to describe the gravitational interaction. As a result, forces are mediated instantly, and mass does not affect the path of light - so accurate ray tracing is not possible. On the other hand, while linear perturbation theory has proved very useful in numerous studies (e.g. the interpretation of the Cosmic Microwave Background power spectrum), it too has its limitations. The approach is to consider a FLRW background upon which small perturbations exist, the evolution of which are governed by the linearised EFEs. The authors of [16] assert that the linear approach should be considered 'a first-order approximation, whose domain of validity is in the early, nearly homogeneous universe'. They argue that although the so-called curvature contrast is very small, $\phi/c^2 << 1$, for galaxy clusters, the density contrast must also be very small in order to remain safely within the linear regime, which is certainly not the case. Going to higher order approximations, as some propose to do,

also poses problems since they are only valid with some range of convergence, the proof for the existence of which is as yet unknown. Moreover, evolution equations become very complex at higher orders, often forcing investigations to focus on one particular phenomenon, setting all other terms to zero. A further drawback to the perturbative approach is that some authors [17, 18, 19, 20] have shown certain spacetimes to be unstable to linearisation. Thus, the study of realistic exact solutions should be seen as complimentary to perturbation theory and N-body simulations, since one would expect to find behaviours manifest in one formalism, and not the other.

When attempting to specify a realistic model of the Universe, it is important to be able to relate quantities that characterise the model to observables in the real Universe. The traditional approach when studying dynamics is to specify the initial conditions of the system, i.e. initial data at some initial time, say t_1, and then evolve it forward in time to some later instant, say t_2. In the case of cosmology one may like to take decoupling as t_1, and the present as t_2, so as to be able to compare one's model with observations. The trouble is that our observations of the last scattering surface can only weakly constrain some of the initial conditions - others must be evolved backwards, from observations at the current time back to t_1, which is often not possible. What ends up happening is one assumes an ansatz for the metric functions and attempts to 'tweak' them to fit observations. The ability to specify a model from a combination of both initial and final data is thus of great utility when trying to construct realistic models from observable data.

Perhaps the most popular inhomogeneous exact solution used in cosmology today is the Lemaitre-Tolman (LT) model. First published in 1933 by Lemaitre [21, 22], and then by Tolman [23] and later popularised by Bondi [24], it has since found numerous applications in the fields of astrophysics and cosmology. It is a spherically symmetric non-static solution to the EFEs with a dust source, and can be thought of as an assembly of concentric spherical mass shells, each with their own evolution. Soon after his publication of the LT solution, Lemaitre [25] used it in an attempt to explain the formation of the galaxies (then called 'nebulae'). He demonstrated that, with the appropriate choice of initial mass distribution, a comoving region around the origin can recollapse, whilst the surrounding region will keep expanding forever. A similar approach was later taken by Bonnor [26], in 1956. Reasoning against the perturbative approach taken by

his contemporaries, Bonnor noted "the field equations are themselves non-linear, and it is at first sight possible that this non-linearity may lead to some process which speeds up (or slows down) the process of condensation in a way not obvious in the linear approximation". He used an LT model to create a transition region between two regions of FLRW space-time, with matching conditions applied at the boundaries. The central FLRW region, with the mass of a typical galaxy, was to represent the condensation, and the outer FLRW region representing the expanding universe outside the condensation. In doing so, he essentially made the assumption that the initial density fluctuation (the interior region) included all dust particles that would enter the future galaxy, and the outer edge of the condensation had to be comoving with the background flow ever after. At the time acoustic oscillation theory had not yet been developed, and the initial fluctuations were assumed to be those of equilibrium statistical physics, of the order 10^{-34}. When calculating the evolution of such a structure, he found that observed structures could not have formed from such an initial fluctuation in the time since decoupling. If it were to have formed in the required amount of time, initial fluctuations of order 10^{-5} would be required, however this would then lead to a condensation with mass much less than a typical galaxy. Nonetheless, this work was very important as the model was constructed from data at both the initial and final times. Much later, inspired by the work of Bonnor, Krasinski & Hellaby published a series of papers [27, 28, 29, 30] (Hereafter referred to as Paper I, II, III and IV respectively) in which they developed a procedure for constructing LT models from a combination of initial and final data, relaxing the aforementioned assumptions of Bonnor. In Paper I, the authors proved that any two spherically symmetric density profiles specified on any two constant time slices can be joined by a LT evolution, and exact implicit formulae for the arbitrary functions that determine the resulting LT evolution were given. They then used this procedure to model, numerically, the formation of an Abell Cluster type structure. They found that such a structure can form in a realistic timescale - from recombination to the present time. Paper II extends the procedure given in the first to that which determines the arbitrary functions of the LT model which evolves from an initial velocity distribution to a final state that is determined either by a density distribution or a velocity distribution. Numerical examples of the evolution of various structures were investigated, such as; the creation of a galaxy cluster out of different velocity distributions; the creation of a galaxy cluster out of different density distributions; and the creation of a void. In

all cases the authors find it entirely possible for such structures to have evolved from initial fluctuations consistent with the CMB anisotropies. They also found that initial velocity fluctuations have a much bigger effect on the subsequent evolution than initial density fluctuations. Paper III applied the methods developed in previous papers to the formation of a galaxy with a central black hole, by two possible mechanisms - condensation around a pre-existing wormhole and the collapse of a spherical dust cloud. For this investigation, the first of its kind, the tools of GR were essential since it is not possible to describe a black hole in Newtonian gravity or as a perturbation around a FLRW background. They used the observationally determined mass of the black hole in M87 as the mass of the black hole at the final time, and were free to choose the profile inside the horizon as observations of such are fundamentally not possible. The exterior late time profile was a typical galaxy profile. At the initial time they used the temperature anisotropies in the CMB as an indirect measure of the density contrast. The profile choice was to be motivated by the angle of these anisotropies on the CMB sky, although the angular resolution of then current measurements was inadequate - about a factor 25 times greater than the angular diameter that a proto-galaxy would occupy on the CMB sky. Choosing a homogeneous initial velocity, they found both mechanisms can efficiently produce a galaxy with a black hole, but condensations around a wormhole occur much quicker. Paper IV goes on to generalise the model construction methods given in the previous three papers, to find the LT model which satisfies any two of the following 'boundary conditions': a simultaneous big bang, a homogeneous density or velocity distribution in the asymptotic future, a simultaneous big crunch, a simultaneous time of maximal expansion, a chosen density or velocity distribution in the asymptotic future, only growing or only decaying modes. Some of these new specification methods were used in [31] to model the Shapely Concentration and the Great Attractor. The importance of velocity profiles was highlighted in [32] were it was demonstrated that an initial over-density can evolve into a void, given a suitable initial velocity profile.

Another interesting family of inhomogeneous exact solutions are those found by Szekeres [33], in 1975. In general, these models have no symmetries (i.e. no killing-vectors [34]) and are defined by six arbitrary metric functions - representing a freedom to rescale the 'radial' coordinate and five degrees of freedom to model inhomogeneity. They are

perhaps the most sophisticated exact solutions with a dust source, and offer exciting prospects for modelling fairly complex cosmic structures. There are two classes of Szekeres models, the LT-type ($\beta_{,z} \neq 0$ or Class I) and the Kantowski-Sachs (KS) type ($\beta_{,z} = 0$ or Class II)[1] Bonnor [37, 38] showed an interior region of LT-type quasispherical Szekeres spacetime can be matched to the exterior Schwarzschild solution, even though the interior metric has no symmetry. Since the Schwarzschild solution does not contain any gravitational radiation, this implies that such Szekeres models do not radiate, and consequently proves the existence of configurations of collapsing dust clouds that have no symmetry and do not produce gravitational waves. Goode & Wainwright [39, 40] introduced a different representation of the Szekeres solutions in which many properties of both subfamilies can be considered together[2]. Furthermore, this formulation facilitates the separation of 'exact perturbations' from background FLRW dynamics. Recently, it has been used by Ishak & Peel [42] to study the evolution of large scale structure. Meures & Bruni [43] recently considered the KS-Type Szekeres solutions with $\Lambda \neq 0$, originally obtained by Barrow & Stein-Schabes [44], to model an arbitrary initial matter distribution along one line of sight. They re-parametrised the solutions into the Goode & Wainwright representation, and gave exact solutions for the growing and decaying modes of the metric perturbation, assuming a flat ΛCDM background.

Within the LT-type class there are three further subclasses, the most popular of which is the 'quasispherical' model, which we focus on here. The geometry of the 'quasi-pseudospherical' and 'quasiplanar' models is still poorly understood [45], perhaps due to our lack of understanding of non-spherical gravity, and so, have not been explored for cosmological applications. The quasispherical model can be thought of as a sequence of non-concentric mass shells, each with a density dipole distribution and its own evolution - a generalization of the LT model [46]. Soon after his publication of these solutions, Szekeres used the quasispherical model to study non-spherical gravitational collapse [47], and since then they have found cosmological application in the study of light propagation [48] as well as structure formation [49]. Bolejko [50] used the quasispherical model to study the evolution and interaction of a void with an adjoining galaxy cluster.

[1] For a comprehensive review of the two classes of Szekeres models, see §19.6 in [35] or, for a more historical account, see §2.4 in [36].

[2] The KS-Type was later shown to be a regular limit of the LT-Type [41]

He found that small voids surrounded by large overdensities evolve much slower than large isolated voids do. And similarly, large voids enhance the evolution of adjacent galaxy superclusters, causing them to evolve much faster than isolated ones. More recently, Sussman & Bolejko [51] presented an approach to describing the dynamics of Szekeres models in terms of 'quasi-local' scalar variables. In this formulation the field equations and basic physical and geometric quantities are formally identical to their corresponding expressions in the LT model, thus potentially allowing the generalisation of rigorous LT results to the non-spherical Szekeres geometry. They then used this formalism to investigate small dipole perturbations away from spherical symmetry, showing that such a configuration is in fact stable.

The aim of this thesis is to develop an algorithm by which one can construct realistic Szekeres models from some given data on the initial and final time surfaces. This will entail deriving expressions for the six arbitrary metric functions, which will completely define the Szekeres model between the initial and final time, from some physically more intuitive quantities. Here we choose to work with initial and final density data, although it is foreseeable that this approach can be extended to include velocity data. The structure of this thesis is as follows: §2 presents the LT model and a summary of the construction procedure; §3 presents the Szekeres model; §4 presents the derivation of expressions for the arbitrary functions, and outlines the model construction procedure; §5 presents the results of the numerical simulations using the procedure outlined in the previous chapter. Conclusions are then presented in §6, along with some comments on future work.

2

Lemaître-Tolman Models

The Lemaître-Tolman (LT) metric, originally derived and discussed in a 1933 paper by Lemaître [21], was the first inhomogeneous non-vacuum metric to be discovered. It is a spherically-symmetric, irrotational, non-static, inhomogeneous dust model, and has become the most popular choice for modelling cosmic inhomogeneity. Some of the numerous cosmological applications include: the formation structures such as black holes [29, 52], galaxy clusters [27, 28], superclusters [31] and cosmic voids [53, 32]; the interpretation of supernova observations [54, 55, 56, 57], CMB anisotropies [58, 59, 60] and redshift drift [61, 62]; and investigating the effect of averaging on spatial inhomogeneities [63].

Subsequent to Lemaître's original discovery, these models were popularised by Tolman [23] and Bondi [24] resulting in them becoming known as "Tolman" or "Tolman-Bondi" models. It has been suggested that this misnomer is perhaps due to a lack of inclination of the majority of the scientific community to look up non-English literature [36]. It was only much later, in 1997, that Lemaître's original paper was translated into English [22]. Currently much of the literature refers to these models as "Lemaître-Tolman-Bondi" or LTB models, however here we will keep our nomenclature in accordance with [36]. It should also be noted that Lemaître models refer to a more general case where the source is a perfect fluid with anisotropic pressure, which is not considered here. For a detailed historical review refer to §2.12 in [36]

This chapter will review some relevant aspects of LT models. Gaining an understanding of these models will provide helpful insight into understanding the Szekeres metric presented in the following chapter. Some of the basic properties of LT models are summarised in §2.1-§2.4 and a model construction algorithm is reviewed in §2.5.

2.1 The LT Metric

The LT metric, in geometric units ($G = c = 1$), is

$$ds^2 = -dt^2 + \frac{R'^2}{1+f}dr^2 + R^2 d\Omega^2 \tag{2.1}$$

where $d\Omega^2 = d\theta^2 + \sin^2\theta d\phi^2$ is the metric of a 2-sphere. $f = f(r)$ is an arbitrary function that determines the type of evolution and the local geometry [1]. The function $R = R(t, r)$ is known as the areal radius as it is related to the area of constant-(t, r) 2-surfaces, and $' \equiv \frac{\partial}{\partial r}$.

The dust source is described by an energy-momentum tensor for a pressure-free perfect fluid,

$$T^{ab} = \rho u^a u^b, \tag{2.2}$$

that is comoving with the coordinate system, such that

$$u^a = \delta^a_t. \tag{2.3}$$

Applying the EFEs to the metric yields two expressions - an equation of motion,

$$\dot{R}^2 = f + \frac{2M}{R} + \frac{\Lambda}{3}R^2, \tag{2.4}$$

and an expression for the energy density,

$$\kappa\rho = \frac{2M'}{R^2 R'}, \tag{2.5}$$

where $\dot{} \equiv \frac{\partial}{\partial t}$ and $M = M(r)$ is another arbitrary function that gives the gravitational mass within a comoving shell of 'radius' r. One can see that (2.4) is simply the Friedmann equation for dust, except that f and M are functions of r.

[1] $f(r)$ also represents twice the local energy density per unit mass of the dust particles, and is often written $f(r) = 2E(r)$.

The evolution of R depends on the value of f. When $\Lambda = 0$ the solutions of (2.4), in terms of the parameter η, are

Hyperbolic ($f > 0$)

$$R = \frac{M}{f}(\cosh\eta - 1)$$
$$(\sinh\eta - \eta) = \frac{f^{3/2}(t - t_b)}{M} \tag{2.6}$$

Parabolic ($f = 0$)

$$R = M\frac{\eta^2}{2}$$
$$\frac{\eta^3}{6} = \frac{t - t_b}{M} \tag{2.7}$$

Elliptic ($f < 0$)

$$R = \frac{M}{(-f)}(1 - \cos\eta)$$
$$(\eta - \sin\eta) = \frac{(-f)^{3/2}(t - t_b)}{M} \tag{2.8}$$

where $t_b = t_b(r)$ is the last arbitrary function - the 'bang time', which gives the local time of the initial singularity $t = t_b$ (i.e. when $R = 0$ on each worldline). So particle worldlines can emerge from the bang at different times, typically outer spheres before inner ones. One can see from the solutions above that worldlines can have either a hyperbolic, parabolic or elliptic evolution, depending on the sign of f[1]. Since $f = f(r)$, it is entirely possible to have adjacent regions of hyperbolic and elliptic evolution. These regions will be connected by a parabolic shell (or extended region) at the boundary, since f is required to be continuous. A nice example of adjacent elliptic and hyperbolic regions is a re-collapsing dust cloud surrounded by an ever-expanding universe [64]. See figure 2.1 for an illustration of these concepts. The time reversed parabolic and hyperbolic cases, obtained by writing $(t_b - t)$ instead of $(t - t_b)$, are also valid solutions.

[1]Near the origin, where $f \to 0$ and $M \to 0$, the evolution type is determined by the sign of Rf/M or $f/M^{2/3}$

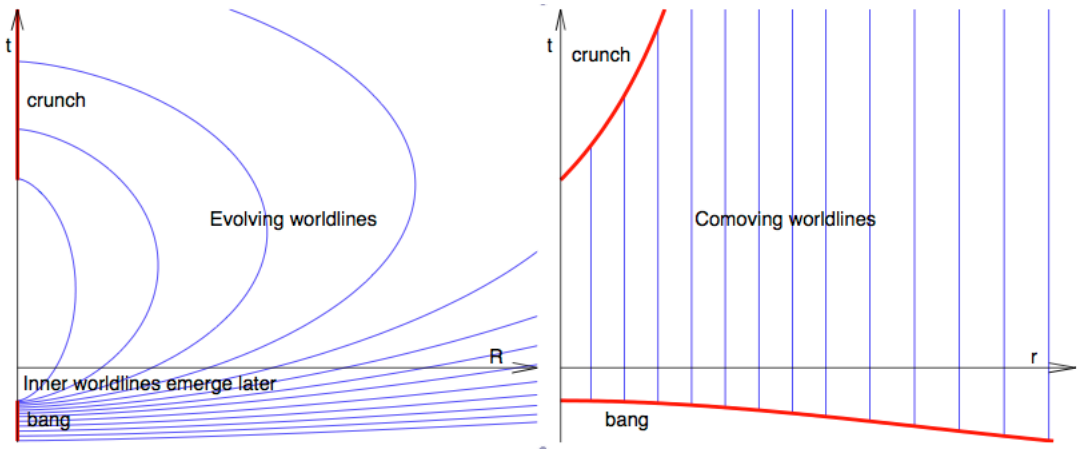

Figure 2.1: Evolving and comoving worldlines - Left panel shows expanding-collapsing (elliptic) worldlines as well as ever-expanding (hyperbolic) worldlines. Right panel illustrates outer shells emerging from the initial singularity before inner shells. *Image: Charles Hellaby*

By eliminating η from the solutions (2.6) (2.7) (2.8), one can write them in the following form

Hyperbolic $(f > 0)$

$$t = t_b + \frac{M}{f^{3/2}} \left[\sqrt{\left(1 + \frac{Rf}{M}\right)^2 - 1} - \operatorname{arccosh}\left(1 + \frac{Rf}{M}\right) \right] \tag{2.9}$$

Parabolic $(f = 0)$

$$t = t_b + \left(\frac{2}{9}\frac{R^3}{M}\right)^{1/2} \tag{2.10}$$

Elliptic $(f < 0,\ 0 \leq \eta \leq \pi)$

$$t = t_b + \frac{M}{(-f)^{3/2}} \left[\arccos\left(1 + \frac{Rf}{M}\right) - \sqrt{1 - \left(1 + \frac{Rf}{M}\right)^2} \right] \tag{2.11}$$

Elliptic $(f < 0,\ \pi \leq \eta \leq 2\pi)$

$$t = t_b + \frac{M}{(-f)^{3/2}} \left[2\pi - \arccos\left(1 + \frac{Rf}{M}\right) + \sqrt{1 - \left(1 + \frac{Rf}{M}\right)^2} \right] \tag{2.12}$$

These solutions will prove to be useful in the model construction procedure described in §2.5.2.

A useful expression for R' is [65]

$$R' = \left(\frac{M'}{M} - \frac{f'}{f}\right) R - \left[t_b' + \left(\frac{M'}{M} - \frac{3f'}{2f}(t - t_b)\right)\right] \dot{R}. \tag{2.13}$$

This is valid for all three expressions (2.6), (2.7)[1], and (2.8).

2.2 Singularities

Singularities are essentially the loci were the density (2.5) or curvature (2.14) diverge, and the assumptions of GR break down. The Kretschmann scalar for LT is

$$\begin{aligned} \mathcal{K} &= R_{abcd} R^{abcd} \\ &= \frac{48M^2}{R^6} + \frac{32MM'}{R^5 R'} + \frac{12M'^2}{R^4 R'^2} \end{aligned} \tag{2.14}$$

where R^{abcd} is the Riemann tensor. In LT models there are two hypersurfaces where such divergences occur; the loci of $R = 0$ and of $R' = 0$. The bang and crunch surfaces are characterised by $R = 0$[2], while $R' = 0$ represents a shell crossing[3] [67].

2.2.1 Bang and Crunch

All LT models have a big bang singularity, or a big crunch singularity, or both. The latter occurring only in the case of elliptic evolution. Hyperbolic and parabolic evolutions must either be ever-expanding away from the initial bang or collapsing toward the crunch (time reverse) and hence only experience one such event. At the big bang and big crunch, where $R = 0$, we see that both (2.14) and (2.5) diverge. These events occur at $t = t_b$ and $t = t_b + 2\pi M/f^{3/2}$ respectively, on spacelike surfaces. In some LT models it is possible for the first events of the big crunch, where the central worldlines reach the crunch surface, to emit light which can escape to infinity. This is referred to as a 'shell focusing' singularity.

[1] In 2.13, one need not set $f'/f = 0$ for the parabolic case, as claimed in [66]. On the boundary between hyperbolic and elliptical regions, one has $f = 0$ and $f' \neq 0$. An f' term remains in (2.13) if the parabolic limit is taken correctly.

[2] $R = 0$ also includes regular origins. See §2.3.2

[3] $R' = 0$ also includes regular spatial extrema, where $f = -1$. See §2.3.3

2.2.2 Shell Crossings

Shell crossings are timelike surfaces that occur where an inner spherical shell of matter collides with an adjacent outer shell, so that $R' = 0$ and the density diverges. Since the r coordinate is comoving, it becomes degenerate at such loci. Shell crossing have been extensively investigated by various authors, for example [65, 68]. In the case where $\Lambda = 0$, shell crossings can be entirely eliminated from the model by applying the conditions found by Hellaby & Lake [65] to the three arbitrary functions. These conditions are summarised in the Table 2.1. It is important to ensure there are no shell crossings if one wants a model that is well behaved everywhere.

2.3 Regularity Conditions

2.3.1 Regular Signature

In order for the metric (2.1) to retain a Lorentzian signature $(-+++)$, the g_{rr} metric component must always remain positive, and thus

$$f \geq -1 \tag{2.15}$$

is required, with the equality only occurring where $R' = 0$[1].

2.3.2 Regular Origins

In spherical coordinates, an origin is a locus r_0 where

$$R(t, r_0) = 0, \qquad \forall\, t \tag{2.16}$$

such that $\dot{R}(t, r_0) = 0$, $\ddot{R}(t, r_0) = 0$, etc. Regular origins require that on any constant t surface away from the bang or crunch, the density (2.5) and curvature (2.14) remain finite, and the time evolution at $r = r_0$ should be a smooth continuation of the immediate neighbourhood. Conditions on the arbitrary functions can be found by assuming $f(r)$ and $M(r)$ are analytic at $r = r_0$ and approximating them by polynomials in r. Taking the limit as $r \to r_0$ yields the following [32, 64]

$$M \sim R^3, \qquad f \sim R^2 \tag{2.17}$$

So with these conditions met, we have a regular origin. Hence the locus $R = 0$ includes both spacelike bang and crunch surfaces, and the timelike origin.

[1] $f = -1$ is required at a spatial extremum, where $R' = 0$, to avoid surface layers. See §2.3.3.

R'	f	M', f', t_b'
> 0	all	$M' \geq 0$
	≥ 0	$f' \geq 0$ $t_b' \leq 0$ but not all 3 equalities at once
	< 0	$\frac{2\pi M}{(-f)^{3/2}}\left(\frac{M'}{M} - \frac{3f'}{2f}\right) + t_b' \geq 0$ $t_b' \leq 0$ but not all 3 equalities at once
$= 0$ $R'' > 0$ neck	-1	$M' = 0$, $f' = 0$, $t_b' = 0$ $f = -1$ for no surface layer $\frac{2\pi M}{(-f)^{3/2}}\left(\frac{M''}{M} - \frac{3f''}{2f}\right) + t_b'' \geq 0$ $t_b'' \leq 0$
$= 0$ $R'' < 0$ belly		$M' = 0$, $f' = 0$, $t_b' = 0$ $f = -1$ for no surface layer $\frac{2\pi M}{(-f)^{3/2}}\left(\frac{M''}{M} - \frac{3f''}{2f}\right) + t_b'' \leq 0$ $t_b'' \leq 0$
< 0	all	$M' < 0$
	≥ 0	$f' < 0$ $t_b' \geq 0$ but not all 3 equalities at once
	< 0	$\frac{2\pi M}{(-f)^{3/2}}\left(\frac{M'}{M} - \frac{3f'}{2f}\right) + t_b' \leq 0$ $t_b' \geq 0$ but not all 3 equalities at once

Table 2.1: LT No Shell Crossing Conditions - The necessary and sufficient conditions on M', f' and t_b' to completely avoid shell crossings in $\Lambda = 0$ LT models.

2.3.3 Regular Spatial Extrema

At a fixed time t in any closed spherically symmetric model there exists a point r_m where $R(t, r_m)$ is maximal, and beyond which R decreases towards a second origin. This implies it is possible to have regular extrema in R along a constant time surface, that does not cause a shell crossing, provided the density and curvature do not diverge. At such an extremum, one obviously has

$$R'(t, r_m) = 0. \tag{2.18}$$

From (2.5), the requirement that the density does not diverge implies

$$M'(r_m) = 0 \tag{2.19}$$

wherever (2.18) holds. Now consider (4.4) evaluated at r_m. Since the coefficients of t_b' and f' are different functions of time, one requires that

$$t_b'(r_m) = 0 \tag{2.20}$$

and

$$f'(r_m) = 0 \tag{2.21}$$

must hold in order to satisfy (2.18). As a result, all the conditions (2.19) (2.20) (2.21) require the surface $R' = 0$ must remain on a comoving shell, i.e.

$$R'(t, r_m) = 0 \qquad \forall\, t. \tag{2.22}$$

However, this does not ensure there are no surface layers at $r = r_m$, even though the M, ρ and $g_{\alpha\beta}$ may all be continuous and finite through the layer [65, 64]. The further condition for the avoidance any surface layers is

$$f(r_m) = -1. \tag{2.23}$$

Hence, the requirements for a regular maximum are that (2.19), (2.20), (2.21) and (2.23) all hold at some r.

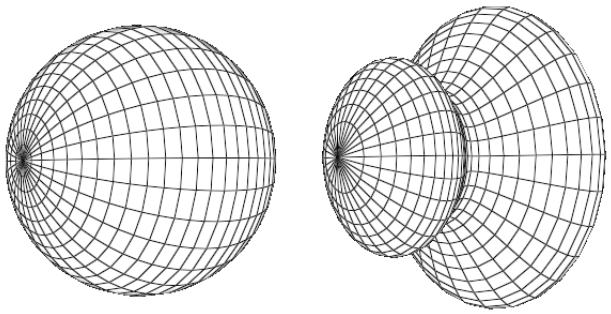

Figure 2.2: Some Closed Spatial Sections - Schematic examples of closed 2-spaces, each two origins and spatial maxima.

2.4 Special Cases

The LT metric contains a number of interesting special cases, some of which are shown in this section.

2.4.1 Dust Friedmann-Lemaitre-Roberson-Walker

The FLRW metric is spatially homogeneous and isotropic. In comoving coordinates it takes the form

$$ds^2 = -dt^2 + S^2(t)\left[\frac{dr^2}{1-kr^2} + r^2 d\Omega^2\right], \tag{2.24}$$

where $S(t)$ is the scale factor and k is curvature parameter, either -1, 0 or 1. The LT metric (2.1) contains the FLRW metric (2.24) with a dust equation of state as a special case. By substituting [64, 35]

$$\begin{aligned} f &\propto M^{2/3} \\ t_b' &= 0 \end{aligned} \tag{2.25}$$

into (2.4) and (2.5) one finds that $\dot{R}/M^{1/3}$ and ρ become independent of r. This can be written in standard FLRW coordinates as

$$\begin{aligned} M &= \frac{\kappa\rho_0 S_0^3}{6} r^3 \\ f &= -kr^2 \\ t_b &= 0 \\ R &= S(t)r \end{aligned} \tag{2.26}$$

where subscript-0 refers to quantities at the present time.

2.4.2 Schwarzschild

The spherically symmetric vacuum metric of Schwarzschild [69],

$$ds^2 = -\left(1 - \frac{2M}{R}\right) dT^2 + \left(1 - \frac{2M}{R}\right)^{-1} dR^2 + R^2 d\Omega, \tag{2.27}$$

can be found from the LT metric by setting $M' = 0$, with different choices of $f(r)$ and $t_b(r)$ resulting in different families of geodesic coordinates covering the manifold. In [70] the author derived Novikov coordinates[1] for the Schwarzschild-Kruskal spacetime from the LT metric. It was shown that in order to recover the full Schwarzschild-Kruskal-Szekeres topology, at the "throat" or "neck" (were $r = r_n$), one requires

$$f(r_n) = -1 \tag{2.28}$$

$$f'(r_n) = 0 \tag{2.29}$$

$$t_b'(r_n) = 0 \tag{2.30}$$

so that $R'(t, r_n) = 0$, and that t_b decreases and f increases on either side of r_n.

2.4.3 Vaidya

The spherically symmetric null dust metric of Vaidya [71, 72], describing radially directed incoherent radiation, has been shown to be a special case of the LT metric in the limit where particle energies go to infinity [73, 74]. The incoming Vaidya metric is

$$ds^2 = 2d\nu dR - \left(1 - \frac{2M}{R}\right) d\nu^2 + R^2 d\Omega^2 \tag{2.31}$$

where $d\Omega^2 = d\theta^2 + \sin^2\theta d\phi^2$ is the metric of a 2-sphere, R is the areal radius, and $M = M(\nu) > 0$ is an arbitrary function of the null coordinate ν which gives the active gravitational mass within ν. In [73] the author showed that the Vaidya metric can be obtained from the LT metric, by making suitable transformations and taking the null limit

$$f \to \infty, \tag{2.32}$$

Later, the author of [74] generalised the work of [73] relaxing a restrictive assumption, and hence showed that Vaidya limit cannot be extended to the origin of spherical

[1] The advantages of this coordinate system is that they clearly show the past and future singularities, the t and r coordinates are timelike and spacelike everywhere, and topological structure becomes quite obvious.

coordinates, since regularity conditions require that $f(0) = 0$ (See §2.3.2). Thus, it was shown that the only LT models which permit a Vaidya limit are those which have hollow central density.

2.4.4 Datt-Kantowski-Sachs

The closed Kantowsi-Sachs (KS) metric [75], describing homogeneous, synchronous, comoving dust, is

$$ds^2 = -dt^2 + X(t)^2 dr^2 + R(t)^2 d\Omega^2, \tag{2.33}$$

where

$$t - t_0 = \frac{A}{2}(\eta - \pi - \sin\eta), \tag{2.34}$$

$$R = \frac{A}{2}(1 - \cos\eta), \tag{2.35}$$

$$X = E + \left[\frac{E}{2}(\pi - \eta) - B\right] \frac{\sin\eta}{1 - \cos\eta}, \tag{2.36}$$

and A, B and E are constants. In these models the areal radius is just a function of time, $R = R(t)$, and thus $R' = 0$, unlike the more general LT case where $R = R(t, r)$. The KS metric (2.33) was, however, shown to be a well behaved limit of the LT metric (2.1) by setting

$$\frac{R'}{\sqrt{1+f}} = X(t), \tag{2.37}$$

and applying additional conditions which reduce the evolution of R' (2.13) to that of (2.36). Defining the arbitrary functions to be [76, 35]

$$M = \int M_1(r)\sqrt{1+f}dr + M_0, \tag{2.38}$$

$$t_b = \int t_{b1}(r)\sqrt{1+f}dr + t_{b0}, \tag{2.39}$$

and choosing $M_1(r)$ and $t_{b1}(r)$ such that E and B remain finite in the limit (i.e. M' and t_b' go to zero), and taking the limit

$$f \to -1, \tag{2.40}$$

one arrives at the KS metric with

$$E = 2M_1 \tag{2.41}$$

$$B = \pi M_1 + t_{b1} \tag{2.42}$$

$$A = 2M_0 \tag{2.43}$$

$$t_0 = t_{b0} + \pi M_0 \tag{2.44}$$

In addition, Datt models [77], which are inhomogeneous generalisations of KS models, have also been shown to be limits of the LT model [76].

2.5 Model Construction

The most obvious way to construct a LT model is to specify the arbitrary metric functions, $M(r)$, $f(r)$ and $t_b(r)$. More typically, one makes a coordinate choice and specifies the initial conditions - for example; the density $\rho(t_{,1}\, M)$ and velocity $R_{,t}\,(t_1, M)$ distributions at some initial time $t = t_1$. Since it is not always obvious what density distribution and model evolution will result from a particular choice of initial conditions, there are situations were it is preferable to determine the metric functions from a combination of initial *and* final data. In the series of articles [27, 28, 29, 30], the authors present a number of useful procedures to determine the LT metric functions when the evolution proceeds from a given; initial density profile to a final density profile [27], an initial velocity profile to a final density/velocity profile [28], and many other alternatives [30]. The focus of this section is on the methods described in the first article, as they will provide a starting point for the Szekeres procedure described in §4.

2.5.1 Coordinate Choice

It is convenient to choose the radial coordinate

$$\tilde{r} = M(r) \tag{2.45}$$

since, within the context of structure formation, one does not expect any 'necks' or 'bellies' where $M' = 0$, and so $M(r)$ should be a strictly growing function in the whole region under consideration. Doing so, however, does not allow one to model regions of vacuum, where $\rho = 0$, as it will cause $M' = 0$, and hence make the r coordinate

degenerate there. One can then write the terms with 'radial' derivatives instead with respect to M, as

$$\frac{\partial}{\partial r} = \frac{\partial}{\partial M} \tag{2.46}$$

Common terms like $R'$and M' then become

$$R' = \frac{\partial R}{\partial M} \tag{2.47}$$

$$M' = 1 \tag{2.48}$$

2.5.2 Initial and Final Density Profiles

In [27] the authors showed that any initial value of density at a specific position $(r, M) = const$ can be connected to any final value of density at the same position by one of the LT evolutions (either $f > 0$, or $f < 0$, or the exceptional case of $f = 0$). And thus, any two spherically symmetric density profiles specified on any two constant time slices can be joined by a LT evolution. Exact implicit formulas for the arbitrary functions that define the resulting LT model were given. Although it could not be guaranteed that the resulting model would be free of physical singularities, numerical experiments indicated that realistic choices of the two density profiles and the time difference are likely to generate reasonable models.

For definiteness, it is assumed in the following that the final instant t_2 is later than the initial instant t_1, and that the final density is smaller than the initial density, at the same M. That is

$$\rho(t_2, M) < \rho(t_1, M), \qquad t_2 > t_1 \tag{2.49}$$

This implies that matter has expanded along every world line, although the analysis can be easily adapted to the collapse situation. Suppose the initial and final density distributions at $t = t_1$ and $t = t_2$ are given by

$$\rho_1(M) = \rho(t_1, M), \qquad \rho_2(M) = \rho(t_2, M). \tag{2.50}$$

Rearranging and integrating (2.5), leads to an expression for the areal radius at the initial and final instant

$$R^3(t_i, M) - R^3_{min,i} = \int_{M_{min}}^{M} \frac{6}{\kappa\rho_i(M^*)} dM^* := R_i^3(M) \qquad i = 1, 2 \tag{2.51}$$

and one usually has $R_{min} = 0 = M_{min}$, certainly with a regular spherical type origin (see §2.3.2). Since M is comoving with particle worldlines, the coordinate choice $r = M$ allows one to determine R_1 and R_2 for each particle by (2.51). As a result of the assumption (2.49) one finds $R_2(M) > R_1(M)$. Defining the variables[1]

$$a_i = \frac{R_i}{M^{1/3}}, \qquad x = \frac{|f|}{M^{2/3}} \tag{2.52}$$

one can re-write the solutions (2.9) (2.11) (2.12), at the initial and final instant, in the following form

Hyperbolic (HX) ($f > 0$)

$$t_i = t_b + x^{-3/2}\left[\sqrt{(1+xa_i)^2 - 1} - \operatorname{arcosh}(1 + a_i x)\right] \tag{2.53}$$

Expanding Elliptic (EX) ($f < 0$, $0 \leq \eta \leq \pi$)

$$t_i = t_b + x^{-3/2}\left[\arccos(1+xa_i) - \sqrt{1-(1+xa_i)^2}\right] \tag{2.54}$$

Collapsing Elliptic (EC) ($f < 0$, $\pi \leq \eta \leq 2\pi$)

$$t_i = t_b + x^{-3/2}\left[2\pi - \arccos(1+xa_i) + \sqrt{1-(1+xa_i)^2}\right] \tag{2.55}$$

At the time t_2 each worldline is either hyperbolic and still expanding (HX), elliptic and still expanding (EX) or elliptic and already collapsing (EC). The borderline cases of two density profiles connected by a parabolic evolution (PX) or an elliptic evolution which is at maximal expansion at $t = t_2$ (EM), where $\eta = \pi$, require special treatment, and must be dealt with separately. Evaluating the expressions (2.53) (2.54) (2.55) at initial and final times and subtracting the two evolutions of the appropriate case allows one to eliminate t_b, leading to

$$\begin{aligned}\psi_{HX} :=& \sqrt{(1+a_2x)^2 - 1} - \operatorname{arcosh}(1+a_2x) \\ &- \sqrt{(1+a_1x)^2 - 1} + \operatorname{arcosh}(1+a_1x) - (t_2 - t_1)x^{3/2} = 0\end{aligned} \tag{2.56}$$

$$\begin{aligned}\psi_{EX} :=& \arccos(1-a_2x) - \sqrt{1-(1-a_2x)^2} \\ &- \arccos(1-a_1x) + \sqrt{1-(1-a_1x)^2} - (t_2 - t_1)x^{3/2} = 0\end{aligned} \tag{2.57}$$

[1] a and x have the advantage of being non-zero at the origin

$$\psi_{EC} := \pi + \arccos(-1 + a_2 x) + \sqrt{1 - (1 - a_2 x)^2} - \arccos(1 - a_1 x) + \sqrt{1 - (1 - a_1 x)^2} - (t_2 - t_1) x^{3/2} = 0 \tag{2.58}$$

Values of the parameters (a_1, a_2, t_1, t_2) for which the above equations (2.56) (2.57) (2.58) have a positive solution $x \neq 0$ can be found by considering their limiting behaviour. When considering the HX case, one finds that

$$\psi_{HX}(0) = 0, \qquad \text{and} \qquad \lim_{x \to \infty} \psi_{HX}(x) = -\infty \tag{2.59}$$

Thus, in order for $\psi_{HX}(x)$ to have a zero on the interval $(0, \infty)$ one requires it to be increasing at $x = 0$ (See Fig. 1 in [27]). Taking the derivative of $\psi_{HX}(x)$ with respect to x, and imposing that it be positive at $x = 0$, one finds that

$$t_2 - t_1 < \frac{\sqrt{2}}{3}(a_2^{3/2} - a_1^{3/2}) \tag{2.60}$$

The inequality (2.60) is a necessary condition for the existence of a non-trivial solution to (2.56). By comparison with (2.10), this is equivalent to the statement that between t_1 and t_2, $R(t, M)$ has increased more than it would have in a $f = 0$ LT model. Conditions for the existence of solutions to (2.57) and (2.58) can be found by following similar reasoning. In the case of EX, one finds the opposite of (2.60), namely

$$t_2 - t_1 > \frac{\sqrt{2}}{3}(a_2^{3/2} - a_1^{3/2}) \tag{2.61}$$

This means that between t_1 and t_2, $R(t, M)$ has increased less than it would have in a $f = 0$ LT model. In addition to this, one requires

$$t_2 - t_1 \leq (a_2/2)^{3/2} \left[\pi - \arccos(1 - 2a_1/a_2) + 2\sqrt{a_1/a_2 - (a_1/a_2)^2}\right] \tag{2.62}$$

The inequalities, (2.61) and (2.62) have been shown to be consistent (See Appendix A of [27]), and are thus necessary and sufficient conditions for (2.57) to define a function $f(M) < 0$ for which $R(t_2, M)$ is still in the expansion phase of the model. In the EC case one finds the opposite of (2.62):

$$t_2 - t_1 > (a_2/2)^{3/2} \left[\pi - \arccos(1 - 2a_1/a_2) + 2\sqrt{a_1/a_2 - (a_1/a_2)^2}\right] \tag{2.63}$$

Thus two densities can be connected by an $f < 0$ evolution that is recollapsing at time t_2 if (2.63) is obeyed. So, knowledge of a_i and t_i allows one to determine the evolution type that joins the two density profiles. It has been shown that the various equations (2.56) (2.57) (2.58) have just a single non-trivial solution, should the relevant inequalities (2.60), (2.61), (2.62), (2.63) hold. This means that there is a single LT evolution (choice of $f(M)$ and $t_B(M)$) which can evolve between the initial and final density profiles. The value of x which solves $\psi(x) = 0$, at each M value, can be found numerically using the bisection method. The range in x over which to bisect and a good starting value for the first guess, x_g, for each evolution type, are give in Table 2.2.

Evolution Type	Bisection Range
HX	$0..(\frac{a_2-a_1}{t_2-t_1})^2$
all other types	$0..\frac{2}{a_2}$

Table 2.2: Bisection Info - Showing, for various evolution types, the range for the bisection method which is used to solve the various $\psi(x) = 0$ equations.

Increasing numerical error in the exact expressions for $\psi(x)$ necessitate the use of series expansions, as the borderlines are approached. Thus, 'fat' borderline equations are used when solving for x in regions near and exactly PX or EM. The range over which these 'fat' borderline expressions are valid is assumed to be, approximately, the region where the ratio of the magnitude of the third order component of the series expansion, to that of the first, is less than 10^{-3}.

To summarise, the nature of the LT model that evolves between the initial and final time slice at a given M is

Hyperbolic ($f > 0$)

if

$$t_2 - t_1 < \frac{\sqrt{2}}{3}(a_2^{3/2} - a_1^{3/2}), \tag{2.64}$$

then, the energy function is given by

$$f = xM^{2/3}, \tag{2.65}$$

and the bang time by (2.53), where x solves

$$\begin{aligned} 0 = \psi_{HX}(x) =& \sqrt{(1+a_2x)^2 - 1} - \operatorname{arcosh}(1+a_2x) \\ & - \sqrt{(1+a_1x)^2 - 1} + \operatorname{arcosh}(1+a_1x) - (t_2 - t_1)x^{3/2}. \end{aligned} \tag{2.66}$$

Near Parabolic ($f \approx 0$)
if $(t_2 - t_1)$ is close to

$$t_2 - t_1 = \frac{\sqrt{2}}{3}(a_2^{3/2} - a_1^{3/2}), \tag{2.67}$$

then, the energy function is given by

$$f = xM^{2/3}, \tag{2.68}$$

and the bang time by

$$t_b = t_i - a_i^{3/2}\left(1 - \frac{3}{20}a_i x + \frac{9}{224}a_i^2 x^2\right), \tag{2.69}$$

where x solves

$$\begin{aligned} 0 = \psi_P(x) \approx \frac{\sqrt{2}x^{3/2}}{3}\Bigg[a_2^{3/2}\left(1 - \frac{3}{20}a_2 x + \frac{9}{224}a_2^2 x^2\right) \\ - a_1^{3/2}\left(1 - \frac{3}{20}a_1 x + \frac{9}{224}a_1^2 x^2\right) - (t_2 - t_1)\Bigg]. \end{aligned} \tag{2.70}$$

Elliptic and still expanding at t_2 ($f < 0$)
if

$$(a_2/2)^{3/2}\left[\pi - \arccos(1 - 2\alpha) + 2\sqrt{\alpha - \alpha^2}\right] > t_2 - t_1 > \frac{\sqrt{2}}{3}(a_2^{3/2} - a_1^{3/2}), \tag{2.71}$$

then, the energy function is given by

$$f = -xM^{2/3}, \tag{2.72}$$

and the bang time by (2.55), where x solves

$$\begin{aligned} 0 = \psi_X(x) = &\arccos(1 - a_2 x) - \sqrt{1 - (1 - a_2 x)^2} \\ &- \arccos(1 - a_1 x) + \sqrt{1 - (1 - a_1 x)^2} - (t_2 - t_1)x^{3/2}. \end{aligned} \tag{2.73}$$

Elliptic and near maximum expansion at t_2 ($f < 0$)
if $(t_2 - t_1)$ is close to

$$t_2 - t_1 = (a_2/2)^{3/2}\left[\pi - \arccos(1 - 2\alpha) + 2\sqrt{\alpha - \alpha^2}\right], \tag{2.74}$$

then, then energy function is given by

$$f = -xM^{2/3}, \tag{2.75}$$

and the bang time by

$$\begin{aligned} t_b &= t_1 - x^{-3/2}\left[\arccos(1-a_1x) - \sqrt{1-(1-a_1x)^2}\right] \\ &\approx t_2 - x^{-3/2}\left[\pi - 2^{3/2}(2-a_2x)^{1/2} + \frac{2^{3/2}}{12}(2-a_2x)^{3/2}\right], \end{aligned} \tag{2.76}$$

where x solves

$$\begin{aligned} 0 = \psi_M(x) =& \pi - 2^{3/2}(2-a_2x)^{1/2} + \frac{2^{3/2}}{12}(2-a_2x)^{3/2} \\ &- \arccos(1-a_1x) + \sqrt{a_1x(2-a_1x)} - (t_2-t_1)x^{3/2}. \end{aligned} \tag{2.77}$$

Elliptic and recollapsing at t_2 ($f < 0$)
if

$$t_2 - t_1 > (a_2/2)^{3/2}\left[\pi - \arccos(1-2\alpha) + 2\sqrt{\alpha-\alpha^2}\right], \tag{2.78}$$

then, the energy function is given by

$$f = -xM^{2/3}, \tag{2.79}$$

and the bang time by (2.54), where x solves

$$\begin{aligned} 0 = \psi_C(x) =& \pi + \arccos(-1+a_2x) + \sqrt{1-(1-a_2x)^2} \\ &- \arccos(1-a_1x) + \sqrt{1-(1-a_1x)^2} - (t_2-t_1)x^{3/2}. \end{aligned} \tag{2.80}$$

2.5.3 Limiting Values at $M = 0$

While several quantities have the value 0 at the origin, Krasinski & Hellaby [27] showed that the variables a_i and x have finite limits as $M \to 0$. Using the definition of a and R^3 and employing l'Hôpital's rule, they showed that the origin value of a is given by

$$a_i(0) = \left(\frac{6}{\kappa\rho_{LT}(t_i,0)}\right)^{1/3} \tag{2.81}$$

The value of x, calculated by solving the relevant $\psi(x) = 0$ equation, comes out non-zero automatically when non-zero values of $a_i(0)$ are used.

2.5.4 Reconstructing Model Evolution

When reconstructing the evolution of the model, it is convenient to re-write the LT solutions in terms of a and x [27]. The time evolution of the quantity a, for the various evolution types, is given below.

Elliptic:

$$a = \frac{1 - \cos\eta}{x}, \qquad t - t_b = \frac{(\eta - \sin\eta)}{x^{3/2}} \tag{2.82}$$

Parabolic or close to it:

$$a = \left(\frac{9}{2}\right)^{1/3} (t - t_b)^{2/3} \left(1 + \frac{x}{20}[6(t - t_b)]^{2/3} - \frac{3x^2}{2800}[6(t - t_b)]^{4/3} + \frac{23x^3}{504000}[6(t - t_b)]^2\right) \tag{2.83}$$

Hyperbolic:

$$a = \frac{\cosh\eta - 1}{x}, \qquad t - t_b = \frac{(\sinh\eta - \eta)}{x^{3/2}} \tag{2.84}$$

In all cases the density is given by

$$\rho_{LT} = \frac{1}{4\pi a^2 (a/3 + M a_{,M})} \tag{2.85}$$

3

Szekeres Models

In 1975 Szekeres published perhaps one of the most sophisticated GR solutions generalising the FLRW model [33, 47]. He solved the EFEs for a diagonal metric form for synchronous comoving dust with $\Lambda = 0$, and no further assumptions. In these models particle worldlines are geodesic and irrotational, $t = const$ hypersurfaces are conformally flat, in general there are no symmetries (i.e. no killing vectors [34]), and they emit no gravitational radiation. Also, any surface of constant coordinate 'radius' r can be matched to a vacuum metric with spherical, planar or pseudo-spherical symmetry. This means that Szekeres models generate a symmetric gravitational field 'outside' each and every constant r shell. They fall into what is known as the Szekeres-Szafron family of solutions, after Szafron generalised Szekeres' solutions for non-zero pressure two years later [78]. For a detailed review of this family of solutions see §2 in [36] or §19.5 in [35].

The only non-trivial solutions in the Szekeres-Szafron family that can be reasonably applied to post-recombination cosmology are the Szekeres metrics. They are a good model for the later phases of evolution of the Universe, in which gravitation plays a dominant role and large-scale hydrodynamical processes have come to an end. There are two families of Szekeres solutions, the LT-type solution (often referred to as the $\beta_{,z} \neq 0$ sub-case) and the KS-type ($\beta_{,z} = 0$ sub-case). Here, we consider only the LT-type Szekeres metric with attention focused on the quasi-spherical case, although the KS-type solution has been shown to be a regular limit of the LT-type solution (see 3.8.4).

3.1 The Szekeres Metric

The LT-type Szekeres metric [33, 47] is

$$ds^2 = -dt^2 + \frac{(R' - R\frac{E'}{E})^2}{\epsilon + f}dr^2 + \frac{R^2}{E^2}(dp^2 + dq^2) \tag{3.1}$$

where $\epsilon = \pm 1, 0$, $E = E(r, p, q)$, $f = f(r)$ is an arbitrary function that determines the type of evolution and the local geometry[1]. The function $R = R(t, r)$ is the areal radius[2], and $' \equiv \frac{\partial}{\partial r}$.

The function $E(r, p, q)$ is often given in the form

$$E(r, p, q) = A(p^2 + q^2) + 2B_1 p + 2B_2 q + C \tag{3.2}$$

where $A = A(r)$, $B_1 = B_1(r)$, $B_2 = B_2(r)$ and $C = C(r)$ are arbitrary functions that must obey

$$4(AC - B_1^2 - B_2^2) = \epsilon \tag{3.3}$$

However, a more convenient form for $E(r, p, q)$ is

$$E(r, p, q) = \frac{S}{2}\left[\left(\frac{p - P}{S}\right)^2 + \left(\frac{q - Q}{S}\right)^2 + \epsilon\right] \tag{3.4}$$

where $S = S(r)$, $P = P(r)$ and $Q = Q(r)$ are arbitrary functions. In this form, the condition (3.3) is automatically satisfied, so calculations are easier. Also S, P and Q have natural interpretations in the Riemann projection (see §3.2)

The dust source is described by the energy-momentum tensor for a pressure-free perfect fluid,

$$T^{ab} = \rho u^a u^b \tag{3.5}$$

that is comoving with the coordinates, such that

$$u^a = \delta^a_t \tag{3.6}$$

[1] $f(r)$ also represents twice the local energy density per unit mass of the dust particles, and is often written $f(r) = 2E(r)$.

[2] R is called the areal radius because it is related to the area of the spherical 2-surfaces. See §3.4.

Applying the EFEs to the metric yields two expressions. An equation of motion,

$$\dot{R}^2 = f + \frac{2M}{R} + \frac{\Lambda}{3}R^2 \tag{3.7}$$

and an expression for the energy density

$$\kappa\rho = \frac{2\left[M' - 3M\left(\frac{E'}{E}\right)\right]}{R^2\left[R' - R\left(\frac{E'}{E}\right)\right]} \tag{3.8}$$

where $\dot{} \equiv \frac{\partial}{\partial t}$ and $M = M(r)$ is another arbitrary function. With $\epsilon = +1$, the function $M(r)$ has the same interpretation as in the LT model - it gives the gravitational mass within a comoving shell of 'radius' r. However in the case where $\epsilon \leq 0$, $M(r)$ has no simple physical interpretation - the reasons for which will become apparent in the following section. The equation of motion (3.7), which determines the dynamics of R, is identical to that of the LT counterpart (2.4), and hence the solutions for $R(t, r)$ are also the same - refer to (2.6), (2.7) and (2.8).

3.2 Riemann Projection

The metric component $(dp^2 + dq^2)/E^2$ is a unit 2-sphere, plane or pseudo-2-sphere in Riemann projection. Depending on the value of ϵ, the p-q 2-surfaces are related to θ-ϕ 2-surfaces by one of the following transformations.

$\epsilon = +1$, either:

$$\left(\frac{p-P}{S}\right) = \cot\left(\frac{\theta}{2}\right)\cos(\phi) \qquad \left(\frac{q-Q}{S}\right) = \cot\left(\frac{\theta}{2}\right)\sin(\phi) \tag{3.9}$$

or

$$\left(\frac{p-P}{S}\right) = \tan\left(\frac{\theta}{2}\right)\cos(\phi) \qquad \left(\frac{q-Q}{S}\right) = \tan\left(\frac{\theta}{2}\right)\sin(\phi) \tag{3.10}$$

$\epsilon = 0$:

$$\left(\frac{p-P}{S}\right) = \left(\frac{2}{\theta}\right)\cos(\phi) \qquad \left(\frac{q-Q}{S}\right) = \left(\frac{2}{\theta}\right)\sin(\phi) \tag{3.11}$$

$\epsilon = -1$, $f > 0$:

$$\left(\frac{p-P}{S}\right) = \coth\left(\frac{\theta}{2}\right)\cos(\phi) \qquad \left(\frac{q-Q}{S}\right) = \coth\left(\frac{\theta}{2}\right)\sin(\phi) \tag{3.12}$$

$\epsilon = -1$, $f < 0$:

$$\left(\frac{p-P}{S}\right) = \tanh\left(\frac{\theta}{2}\right)\cos(\phi) \qquad \left(\frac{q-Q}{S}\right) = \tanh\left(\frac{\theta}{2}\right)\sin(\phi) \tag{3.13}$$

The transformed 2-metrics are then

$$\epsilon = +1, \qquad ds^2 = R^2(d\theta^2 + \sin^2(\theta)d\phi^2) \tag{3.14}$$

$$\epsilon = 0, \qquad ds^2 = R^2(d\theta^2 + \theta^2 d\phi^2) \tag{3.15}$$

$$\epsilon = -1, \qquad ds^2 = R^2(d\theta^2 + \sinh^2(\theta)d\phi^2) \tag{3.16}$$

From the transformation equations (3.9-3.13) it is evident that the factor ϵ determines the geometry of the p-q 2-surfaces, which can be either spherical ($\epsilon = +1$), planar ($\epsilon = 0$) or pseudo-spherical ($\epsilon = -1$). In the case where $\epsilon = +1$ each of the spherical transformations (3.9) and (3.10) cover the entire p-q plane with $0 \leq \theta \leq \pi$ and $0 \leq \phi \leq 2\pi$, so either can be used. When $\epsilon = -1$, both of the pseudo-spherical transformations (3.12) and (3.13) are required to cover the entire p-q plane once. Constant-r shells seem to be two-sheeted hyperboloids. Each of the transformations maps one of the hyperboloid sheets to the p-q plane, with $0 \leq \theta \leq \infty$ and $0 \leq \phi \leq 2\pi$. In order to distinguish between the two sheets one can choose θ positive on one sheet and negative on the other. In the $\epsilon = 0$ case the planar transformation (3.11) is sufficient to cover the entire p-q plane with $0 \leq \theta \leq \infty$ and $0 \leq \phi \leq 2\pi$. This transformation can be thought of as mapping a semi-infinite cylinder to a plane, or the inversion of a circle in a plane [64]. In the case of the planar and pseudo-spherical transformations, θ is not an angle but rather a measure of 'distance' along the hyperboloid/cylinder. See figures (3.1), (3.2) and (3.3) for illustrations of the projections.

3.3 Properties of E

3.3.1 The $E = 0$ locus

At any particular value of coordinate 'radius' r, the function $E(r, p, q)$ given in (3.4) has circular symmetry in the p-q plane about the point $(p, q) = (P, Q)$. This point of symmetry can change with r, since $P = P(r)$ and $Q = Q(r)$. Setting (3.4) equal to zero one finds the locus $E = 0$ to be

$$(p-P)^2 + (q-Q)^2 = -\epsilon S^2 \tag{3.17}$$

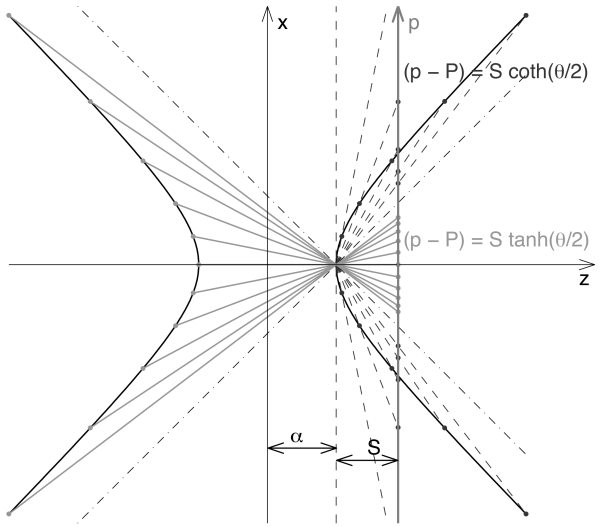

Figure 3.1: Pseudo-Spherical Riemann Projection - Showing the transformation between (p, q) and (θ, ϕ) coordinates for the $\epsilon = -1$ case. *Image: Charles Hellaby*

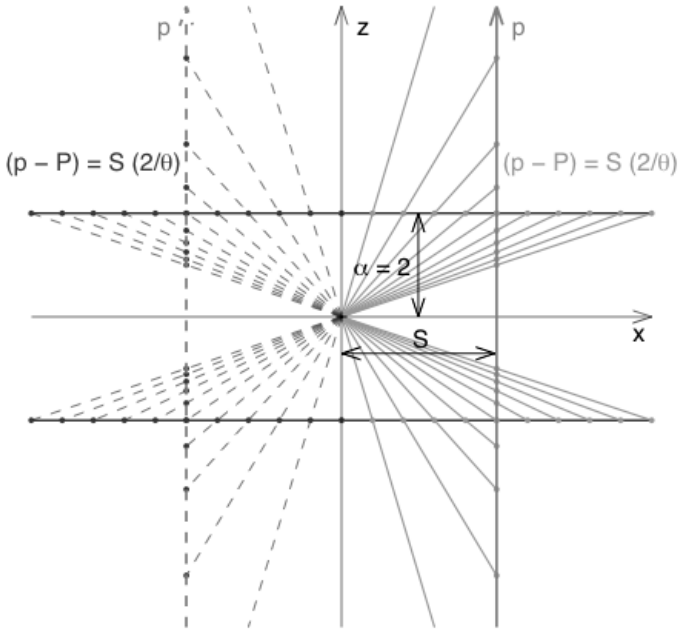

Figure 3.2: Planar Riemann Projection - Showing the transformation between (p, q) and (θ, ϕ) coordinates for the $\epsilon = 0$ case *Image: Charles Hellaby*

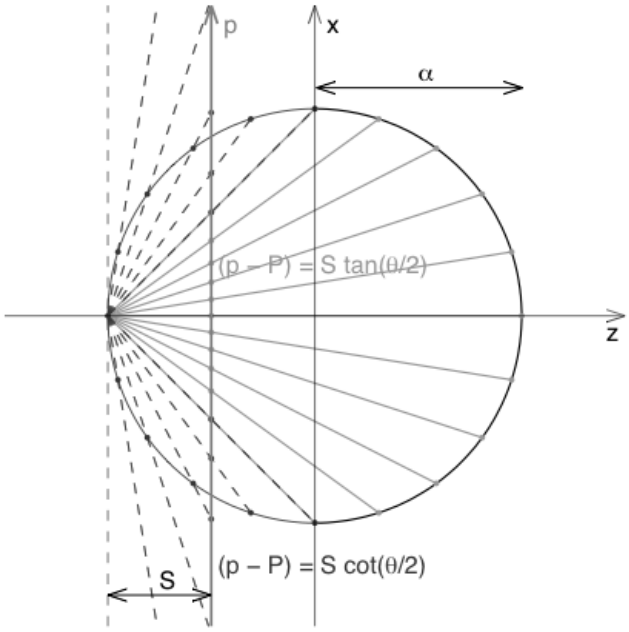

Figure 3.3: Spherical Riemann Projection - Showing the transformation between (p, q) and (θ, ϕ) coordinates for the $\epsilon = +1$ case. Each of the projection formulae, (3.9) and (3.10), maps the full sphere to the plane, but only half of each is shown, one as solid grey lines and the other as dashed black lines. The figure shows only the $\phi = 0$, π section. For the full projection the curves should be rotated about the z axis and the q dimension added. *Image: Charles Hellaby*

When $\epsilon = -1$ the locus (3.17) is a circle in the p-q plane centred at $(p, q) = (P, Q)$ with a radius equal to S. Outside this circle $E > 0$, and inside $E < 0$. In the $\epsilon = 0$ case the circle reduces to a single point, $(p, q) = (P, Q)$. Thus, $E > 0$ everywhere in the p-q plane except at the centre of symmetry, where $E = 0$. With $\epsilon = +1$ the locus (3.17) ceases to exist, and $E > 0$ everywhere in the p-q plane. [64]

3.3.2 The $E' = 0$ locus

Differentiating (3.4) with respect to r gives an expression for $E'(r, p, q)$, which can be written as

$$E' = \frac{S'}{2}\left[-\frac{(p-P)^2 + (q-Q)^2}{S^2} + \epsilon\right] - \frac{1}{S}\left[(p-P)P' + (q-Q)Q'\right] \tag{3.18}$$

Now, setting (3.18) equal to zero, one finds the locus $E' = 0$ is

$$\left[p - \left(P - P'\frac{S}{S'}\right)\right]^2 + \left[q - \left(Q - Q'\frac{S}{S'}\right)\right]^2 = S^2\left(\frac{P'^2 + Q'^2}{S'^2} + \epsilon\right) \tag{3.19}$$

This is the equation of a circle in the p-q plane centred at the point $(p, q) = (P - P'S/S', Q - Q'S/S')$ with radius $S\sqrt{(P'^2 + Q'^2)/S'^2 + \epsilon}$. When $S' > 0$, one finds $E' < 0$ inside the circle and $E' > 0$ outside [46]. The locus always exists in the $\epsilon \geq 0$ cases, and when $\epsilon = -1$ it only exists if

$$S'^2 < P'^2 + Q'^2 \tag{3.20}$$

If both the loci (3.17) and (3.19) exist, it can be shown that they will always intersect [64].

3.3.3 General Behaviour of E'/E

The loci (3.17) and (3.19) have the effect of creating poles and zeros in the function E'/E. One expects E'/E to diverge at the $E = 0$ locus, and to be zero at the $E' = 0$ locus. The only exception being at the intersection of the two loci, where $E'/E = 0/0$, and hence may take on a limiting value. However this can only happen in models where $\epsilon \leq 0$, since those are the only models in which both the loci can exist. When $\epsilon = +1$, one has $E > 0$ everywhere and hence the sign and zeros of E'/E are the same as for

E'. The $E'/E = 0$ locus is then given by (3.19), with $E'/E > 0$ outside[1] the circle and $E'/E < 0$ inside the circle when $S' > 0$.

3.4 Spatial Foliations

As was shown in §3.2, the value of ϵ determines the shape of the constant-(t, r) 2-surfaces. At each value of r, these 2-surfaces are multiplied by the factor $R = R(t, r)$, and hence, the r-p-q 3-spaces are constructed from a sequence of constant-(t, r) 2-surfaces which have a curvature scale related to R, and shape determined by ϵ. The g_{rr} component of the metric (3.1) is affected by p-q variations via the function E'/E (3.24), which means that the radial separation between two neighbouring surfaces of constant-(t, r) also has p-q variation, and thus these 2-surfaces are interpreted as being arranged non-symmetrically relative to each other. It is from these families of 2-surfaces that the various Szekeres models acquire their name, with the prefix *quasi-* denoting the fact that they are 'non-concentric'.

ϵ	constant-(t, r) 2-surfaces	Model Name
$+1$	sequence of Riemann spheres	quasi-spherical
0	sequence of Riemann planes	quasi-planar
-1	sequence of right Riemann hyperboloids	quasi-pseudospherical

Table 3.1: The Effect of ϵ - Showing the shape of constant-(r, t) 2-surfaces and the associated model name for the various values of ϵ

The area of a constant-(t, r) 2-surface is given by

$$A = R^2 \int\int \frac{dpdq}{E^2} \tag{3.21}$$

In the $\epsilon \leq 0$ cases, (3.21) is infinite and the constant-(t, r) surfaces are not closed. As a result M can no longer be interpreted as the gravitational mass within 'radius' r. When $\epsilon = +1$, one finds $A = 4\pi R^2$ which explains why R is called the areal radius.

In order for the metric (3.1) to retain a Lorentzian signature, we require $g_{rr} > 0$, and thus it follows that $\epsilon + f \geq 0$ must then always hold (See §3.7.1 for details). So, for

[1]The p-q plane is a sphere/plane/pseudo-sphere in Riemann projection. On the θ-ϕ 2-surfaces inside and outside are topologically equivalent [64]

the various evolution types only certain 2-surfaces are permitted to foliate the spatial sections. The possibilities are summarised below, in Table 3.2.

Evolution Type	f	ϵ	Permissible 2-surfaces
Hyperbolic	> 0	$+1, 0, -1$	spherical, planar, pseudo-spherical
Parabolic	$= 0$	$+1, 0$	spherical, planar
Elliptic	$\leq -1, < 0$	$+1$	spherical

Table 3.2: Permissible Spatial Foliations - Showing the permissible 2-surfaces of constant-(t, r) that can foliate a spatial section, for a given evolution type

It is possible to have all three types of foliation in one model. In fact, Szekeres' original formulation had $\epsilon = \epsilon(r)$. In this case it is possible to have regions of spherical foliation connected to those hyperbolic foliation, via a planar boundary [45].

3.5 Quasi-Spherical Case

From the family of Szekeres models it is the $\epsilon = +1$ quasi-spherical case that has received the most attention in the field of cosmology. They have found applications in the study of the early Universe [79, 80], structure formation [49, 50], the dimming of the supernovae [81, 82], light propagation [48], CMB observations [83] and volume averaging [84]. The $\epsilon \leq 0$ cases have been far less investigated [45, 85], the geometry is still not well understood, and are yet to find cosmological application. While these models may prove of some use in future, in this thesis we focus attention on the quasi-spherical case, in which we expect the generalisation of the LT model construction procedure to be easiest.

3.5.1 E'/E dipole

The function E'/E has a dipole variation around each constant-$(t,\ r)$ 2-sphere, with the extrema located at antipodal points. It is also antisymmetric, with $E'/E = 0$ on the 'equator' between the two 'poles'. In order to illustrate the variation of E'/E over a constant-$(t,\ r)$ 2-sphere we begin by transforming to $(\theta,\ \phi)$-coordinates. In the quasi-spherical case, expressions for $E(r, \theta, \phi)$ and $E'(r, \theta, \phi)$ are obtained by setting $\epsilon = +1$ and applying either of the spherical transformations (3.9) or (3.10) to (3.4) and

its derivative (3.18). This yields

$$E = \frac{S}{1-\cos\theta} \tag{3.22}$$

and

$$E' = -\frac{S'\cos\theta + \sin\theta(P'\cos\phi + Q'\sin\phi)}{1-\cos\theta} \tag{3.23}$$

An expression for E'/E in (θ, ϕ)-coordinates is found by dividing (3.23) by (3.22), to give

$$\frac{E'}{E} = -\frac{S'\cos\theta + \sin\theta(P'\cos\phi + Q'\sin\phi)}{S} \tag{3.24}$$

Setting (3.24) equal to zero, one finds the locus $E'/E = 0$, which is

$$S'\cos\theta + P'\sin\theta\cos\phi + Q'\sin\theta\sin\phi = 0 \tag{3.25}$$

Applying the rectangular transformations

$$x = \sin\theta\sin\phi, \qquad y = \sin\theta\cos\phi \qquad z = \cos\theta \tag{3.26}$$

to the result (3.25) allows for a natural interpretation. One finds

$$P'x + Q'y + S'z = 0 \tag{3.27}$$

which is the equation of an arbitrary plane passing through $(0,0,0)$. The locus $E'/E = 0$ is then the intersection of this plane with the unit 2-sphere. Since any such plane passing through $(0,0,0)$ must intersect the unit sphere along a great circle, the locus $E'/E = 0$ must then also be great circle. The unit normal to the plane (3.27) is

$$\vec{n} = \frac{(P', Q', S')}{\sqrt{(P')^2 + (Q')^2 + (S')^2}} \tag{3.28}$$

By setting (3.24) equal to a constant and employing the rectangular transformations mentioned above, one finds the loci E'/E =constant in the same form as (3.27). This gives

$$P'x + Q'y + S'z = kS \qquad k = constant \tag{3.29}$$

which is the equation of an arbitrary plane parallel to (3.27). This implies that all the loci E'/E =constant are small circles parallel to the $E' = 0$ great circle (3.25).

The location on the 2-sphere of the E'/E extrema (i.e. the poles) are found by finding where the partial derivatives of E'/E, with respect to θ and ϕ, are equal to zero. Denoting the location of the extrema by (θ_e, ϕ_e) one finds the extrema in ϕ as follows

$$\frac{\partial(E'/E)}{\partial\phi} = \frac{\sin\theta(P'\sin\phi - Q'\cos\phi)}{S} = 0$$

$$\Rightarrow \tan\phi_e = \frac{Q'}{P'} \tag{3.30}$$

$$\Rightarrow \cos\phi_e = \epsilon_1 \frac{P'}{\sqrt{P'^2 + Q'^2}}, \qquad \epsilon_1 = \pm 1 \tag{3.31}$$

and the extrema in θ as follows

$$\frac{\partial(E'/E)}{\partial\theta} = \frac{S'\sin\theta - P'\cos\theta\cos\phi - Q'\cos\theta\sin\phi}{S} = 0$$

$$\Rightarrow \tan\theta_e = \epsilon_1 \frac{\sqrt{P'^2 + Q'^2}}{S'} \tag{3.32}$$

$$\Rightarrow \cos\theta_e = \epsilon_2 \frac{S'}{\sqrt{S'^2 + P'^2 + Q'^2}}, \qquad \epsilon_2 = \pm 1 \tag{3.33}$$

Applying the transformation (3.26) to the expressions found above gives the location of the extrema in rectangular coordinates. One finds

$$(x_e, y_e, z_e) = \epsilon_2 \frac{(P', Q', S')}{\sqrt{(P')^2 + (Q')^2 + (S')^2}} \tag{3.34}$$

This vector points in the same direction as the vector normal to the plane of the great circle (3.28), so the extrema of E'/E are located at the poles of $E'/E = 0$ great circle. The extreme values of E'/E are found by substituting the location of the extrema (3.31) (3.33) into (3.24), which gives

$$\left(\frac{E'}{E}\right)_{extreme} = -\epsilon_2 \frac{\sqrt{S'^2 + P'^2 + Q'^2}}{S} \tag{3.35}$$

The parameters ϵ_2 and ϵ_1 are not independent[1]. The relationship between the two can be found by relating the sign of (3.32) to that of (3.33), as follows. Noting that θ is defined on the interval $[0, \pi]$, we have $\sin\theta \geq 0$, and hence

$$\begin{aligned} \text{sign}(\cos\theta_e) &= \text{sign}(\tan\theta_e) \\ \Rightarrow \text{sign}(\epsilon_2 S') &= \text{sign}(\epsilon_1 / S') \\ \Rightarrow \epsilon_1 &= \epsilon_2 \end{aligned} \tag{3.36}$$

[1] The presentation in [46] misses this point

This seems reasonable since we expect only two extrema. From (3.35) and (3.36), and assuming that $S > 0$ always holds, we deduce that $\epsilon_1 = \epsilon_2 = 1$ corresponds to a dipole minimum, while the dipole maximum is given by $\epsilon_1 = \epsilon_2 = -1$. From this, it is clear that

$$\left(\frac{E'}{E}\right)_{max} = -\left(\frac{E'}{E}\right)_{min} \tag{3.37}$$

And at the dipole maximum, the E'/E value is then

$$\left(\frac{E'}{E}\right)_{max} = \frac{\sqrt{S'^2 + P'^2 + Q'^2}}{S} \tag{3.38}$$

and the orientation angles are

$$\cos\phi_{max} = -\frac{P'}{\sqrt{P'^2 + Q'^2}} \tag{3.39}$$

$$\cos\theta_{max} = -\frac{S'}{\sqrt{S'^2 + P'^2 + Q'^2}} \tag{3.40}$$

3.5.2 Shell Separation

As pointed out in §3.4, the g_{rr} component of the metric (3.1) is sensitive to p-q (and hence θ-ϕ) variations via the function E'/E, and hence the constant-(t, r) 2-surfaces are interpreted as being arranged non-symmetrically. Writing the radial separation as

$$R' - R\frac{E'}{E} = R' + R\frac{S'\cos\theta + P'\sin\theta\cos\phi + Q'\sin\theta\sin\phi}{S} \tag{3.41}$$

we see that RE'/E is a correction term to the spherically symmetric radial separation, R', that an LT model would have. Clearly the separation between neighbouring shells depends on θ-ϕ, and hence p-q. This can be decomposed into a forward ($\theta = 0$) displacement RS'/S, and two sideways displacements RP'/S and RQ'/S in the directions ($\theta = \pi/2$, $\phi = 0$) and ($\theta = \pi/2$, $\phi = \pi/2$) respectively. The minimum radial separation between neighbouring constant-r shells obviously occurring where E'/E is maximum. Hence, $\epsilon = +1$ Szekeres 3-spaces are interpreted as being constructed from a sequence of non-concentric 2-spheres, with each shell having the exact density distribution required to generate a spherical field around the new centre. See figure 3.4 for illustrations of these concepts.

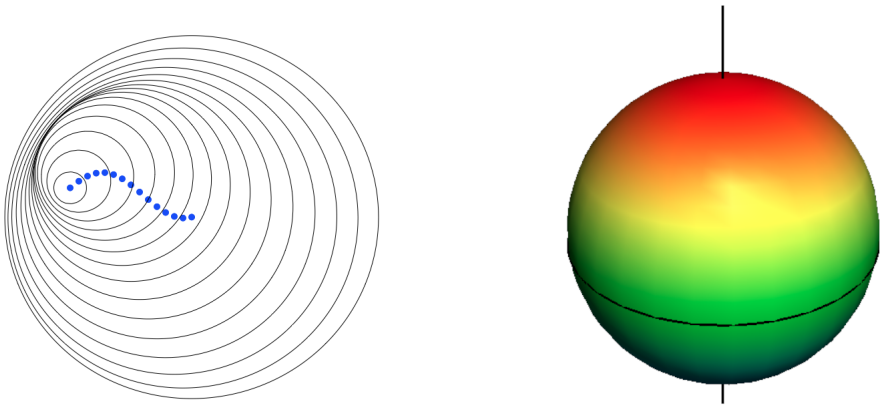

Figure 3.4: Shell Separation and the E'/E Dipole - *Left pane*: Showing the non-concentricity of various constant-(r,t) 2-spheres. Blue dots indicate the centres of the 2-sphere. *Right pane*: The E'/E dipole over a single 2-sphere.

3.5.3 Density Dipole

The dipole variation in E'/E around each constant-(t,r) 2-sphere causes a dipole variation in the density (3.8). At the equator, where $E'/E = 0$, we see that (3.8) reduces to the form

$$\kappa\rho_{LT} = \frac{2M'}{R^2R'} \tag{3.42}$$

which is identical to the expression for density in LT models (2.5). In the context of Szekeres models, we refer to the equatorial density (3.42) as the LT-density, denoted by the subscript LT. Szekeres [47], and then later de Souza [86] (also see p. 419 of [35] or p. 30 of [36]), showed that the density around any constant-$(t,r,)$ 2-sphere can be decomposed into a monopole and a dipole component

$$\rho = \rho_s + \Delta\rho \tag{3.43}$$

where the monopole is

$$\rho_s = \frac{2M'(A+C) - 6M(A'+C')}{R^2R'(A+C) - R^3(A'+C')} \tag{3.44}$$

and the dipole is

$$\Delta\rho = \frac{A'+C'-(A+C)E'/E}{R'-RE'/E}\,\frac{6MR'-3M'R}{R^2R'(A+C)-R^3(A'+C')} \tag{3.45}$$

The surface $\Delta\rho = 0$ intersects any constant-(t, r) 2-sphere where

$$\frac{E'}{E} = \frac{A' + C'}{A + C} = constant \tag{3.46}$$

which is a circle parallel to the $E'/E = 0$ great circle (see (3.29)). The dipole lacks the anti-symmetrical property, i.e. $\Delta\rho(-E'/E) \neq -\Delta\rho(E'/E)$, except when $A' + C' = 0$, in which case the $\Delta\rho = 0$ circle coincides with the $E'/E = 0$ great circle.

3.6 Singularities

Szekeres models contain the same singularities as in LT - those of the bang, the crunch and shell crossings. The Kretschmann scalar is

$$K = \kappa^2 \left(\frac{4}{3}\rho_{AV}^2 - \frac{8}{3}\rho_{AV}\rho + 3\rho^2 \right) + \frac{4\Lambda}{3}(2\Lambda + \kappa\rho) \tag{3.47}$$

where

$$\kappa\rho_{AV} \equiv \frac{6M}{R^3} \tag{3.48}$$

is referred to as the "internal average" density.

3.6.1 Bang and Crunch

The dynamics of R in Szekeres models (3.7) is identical to that of LT models (2.4), and hence the bang and crunch singularities are the same. All Szekeres models have a big bang singularity, or a big crunch singularity, or both. The latter occurring only in the case of elliptic evolution. Hyperbolic and parabolic evolutions must either be ever-expanding away from the initial bang or collapsing toward the crunch (time reverse) and hence only experience one such event. At the big bang and big crunch, where $R = 0$, both the density (3.8) and curvature (3.47) diverge. These events occur at $t = t_b$ and $t = t_b + 2\pi M/f^{3/2}$ respectively, on spacelike surfaces.

3.6.2 Shell Crossings

Shell crossings occur when inner shells of matter pass outer ones, causing the density to diverge and the radial coordinate, r, to become degenerate. In Szekeres models they are more complicated than in the spherically symmetric LT case, as non-concentricities

cause constant-r shells to pass through each other gradually, and one shell may intersect many others at any given time. They occur at the loci where

$$R' - R\frac{E'}{E} = 0 \tag{3.49}$$

provided

$$M' - 3M\frac{E'}{E} \neq 0 \neq \epsilon + f \tag{3.50}$$

Evaluating these conditions one finds the density (3.8) diverges, and the g_{rr} component of the metric (3.1) is zero. So to avoid shell crossing one requires, in addition to the LT conditions, further constraints on the 'radial' derivatives of the arbitrary functions S', P' and Q'. These conditions were investigated in [46] for the $\Lambda = 0$ case, and are summarised in Table 3.3.

3.7 Regularity Conditions

3.7.1 Regular Signature

For the metric (3.1) to retain Lorentzian signature $(-+++)$, the g_{rr} component must always remain positive, and thus

$$\epsilon + f \geq 0 \tag{3.51}$$

is required, with the equality only occurring where $R' - RE'/E = 0$. Clearly the geometry determined by f limits possible constant-$(t, r,)$ 2-surfaces that can foliate the spatial sections. See Table 3.2 for details.

3.7.2 Regular Origins

In the $\epsilon = +1$ case the origin of spherical coordinates is the locus $r = r_0$ where

$$R(t, r_0) = 0 \qquad \forall\, t \tag{3.52}$$

so that $\dot{R}(t, r_0) = 0$, $\ddot{R}(t, r_0) = 0$ etc. Regular origins require that on any constant t surface away from the bang or crunch, the density (3.8) and curvature (3.47) remain finite, and the time evolution at $r = r_0$ should be a smooth continuation of the immediate neighbourhood. Conditions on the arbitrary functions were investigated in [46]

ϵ	R'	f	M', f', t'_b	S', P', Q'
$+1$	> 0	all	$M' \geq 0$	$\frac{\sqrt{(S')^2+(P')^2+(Q')^2}}{S} \leq \frac{M'}{3M}$
		≥ 0	$f' \geq 0$ $t'_b \leq 0$ but not all 3 equalities at once	$\frac{\sqrt{(S')^2+(P')^2+(Q')^2}}{S} \leq \frac{f'}{2f}$ (no condition where $f = 0$)
		< 0	$\frac{2\pi M}{(-f)^{3/2}}\left(\frac{M'}{M} - \frac{3f'}{2f}\right) + t'_b \geq 0$ $t'_B \leq 0$ but not all 3 equalities at once	
	$= 0$ $R'' > 0$ neck	-1	$M' = 0$, $f' = 0$, $t'_b = 0$ $f = -1$ for no surface layer $\frac{2\pi M}{(-f)^{3/2}}\left(\frac{M''}{M} - \frac{3f''}{2f}\right) + t''_b \geq 0$ $t''_b \leq 0$	$S' = 0$, $P' = 0$, $Q' = 0$ $\frac{\sqrt{(S'')^2+(P'')^2+(Q'')^2}}{S} \leq \frac{M''}{3M}$
	$= 0$ $R'' < 0$ belly		$M' = 0$, $f' = 0$, $t'_b = 0$ $f = -1$ for no surface layer $\frac{2\pi M}{(-f)^{3/2}}\left(\frac{M''}{M} - \frac{3f''}{2f}\right) + t''_b \leq 0$ $t''_b \leq 0$	$S' = 0$, $P' = 0$, $Q' = 0$ $-\frac{\sqrt{(S'')^2+(P'')^2+(Q'')^2}}{S} \geq \frac{M''}{3M}$
	< 0	all	$M' < 0$	$-\frac{\sqrt{(S')^2+(P')^2+(Q')^2}}{S} \geq \frac{M'}{3M}$
		≥ 0	$f' < 0$ $t'_b \geq 0$ but not all 3 equalities at once	$-\frac{\sqrt{(S')^2+(P')^2+(Q')^2}}{S} \geq \frac{f'}{2f}$ (no condition where $f = 0$)
		< 0	$\frac{2\pi M}{(-f)^{3/2}}\left(\frac{M'}{M} - \frac{3f'}{2f}\right) + t'_b \leq 0$ $t'_b \geq 0$ but not all 3 equalities at once	

Table 3.3: Szekeres No Shell Crossing Conditions - The necessary and sufficient conditions on M', f', t'_b, S', P' and Q' to completely avoid shell crossings in $\Lambda = 0$ quasi-spherical Szekeres models.

by evaluating the limit $r \to r_0$ of the aforementioned quantities and ensuring they are well behaved. They found the regularity conditions require that near the origin

$$\begin{aligned} &M \sim R^3 \qquad f \sim R^2 \\ &S \sim R^n \qquad P \sim R^n \qquad Q \sim R^n \qquad 0 \leq n \leq 1 \end{aligned} \tag{3.53}$$

Of the five conditions above, the first two conditions are the same as in LT (2.17).

3.7.3 Regular Spatial Extrema

Extrema in R may occur in models with certain topologies. For example, closed spatial sections can have R increasing away from the origin until some point, say $r = r_m$, where R is maximal and beyond which R is decreasing toward a second origin. The conditions to ensure regularity of these loci were investigated in [46]. Ensuring $R' = 0$ at the maximum, thus ensuring no shell crossings, requires

$$\begin{aligned} &M'(t, r_m) = f'(t, r_m) = t'_B(t, r_m) = 0 \\ &S'(t, r_m) = P'(t, r_m) = Q'(t, r_m) = 0 \qquad \forall\, t \end{aligned} \tag{3.54}$$

Furthermore, to avoid any surface layers at $r = r_m$ requires

$$f = -\epsilon \tag{3.55}$$

With these conditions met, the density (3.8) and the g_{rr} component of the metric (3.1) remain positive and finite, thus ensuring regular extrema.

3.8 Special Cases

3.8.1 Lemaître-Tolman

The LT metric (2.1) is the spherically symmetric special case of the Szekeres metric (3.1), and can be found by setting

$$\begin{aligned} &\epsilon = +1 \\ &S = P = Q = constant \\ \Rightarrow &E = constant \\ \Rightarrow &E' = 0 \end{aligned} \tag{3.56}$$

The Szekeres metric therefore contains all the LT special cases given in §2.4, and has geometric possibilities that are at least as interesting.

3.8.2 Ellis Metrics

Ellis [87] solved the EFEs for a dust source and cosmological constant, and found all the solutions with a local rotational symmetry. These solutions, in the same notation as we use in previous sections, are given by

$$ds^2 = -dt^2 + \frac{R'^2}{\epsilon + f}dr^2 + R^2(d\theta^2 + h(\theta)^2 d\phi^2), \tag{3.57}$$

where,

$$\begin{aligned} &\epsilon = +1, && h(\theta) = \sin\theta && \text{for spherical symmetry} \\ &\epsilon = 0, && h(\theta) = \theta && \text{for plane symmetry} \\ &\epsilon = -1, && h(\theta) = \sinh\theta && \text{for hyperbolic symmetry} \end{aligned} \tag{3.58}$$

and the dynamics of R are identical to Szekeres (3.7) and LT (2.4) models. By setting $E' = 0$ in the Szekeres solutions, one recovers the Ellis family of solutions.

3.8.3 The Null Limit

The null limit of Szekeres models is found in the same manner as for LT, by letting the particle energy diverge while R and M remain finite

$$f \to \infty \qquad R, M \text{ finite} \tag{3.59}$$

By applying suitable transformations and taking the null limit, one finds the metric of the form

$$ds^2 = -\left[\epsilon - \frac{2M(\nu)}{R} - 2\sigma R\frac{E^*(\nu,p,q)}{E^*(\nu,p,q)}\right]d\nu^2 - 2\sigma d\nu dR + \frac{R^2}{E^2(\nu,p,q)}(dp^2 + dq^2) \tag{3.60}$$

This is the pure radiation Robinson-Trautman metric of Petrov type D, which contains the Vaidya metric and the Kinnersly rocket metric as special cases. By setting

$$\begin{aligned} &\epsilon = +1 \\ &E = 1 \\ &E^* = 0 \end{aligned} \tag{3.61}$$

one recovers the Vaidya metric. The Kinnersly rocket metric is then found by setting

$$\begin{aligned} &\epsilon = +1 \\ &\sigma = +1 \end{aligned} \tag{3.62}$$

The interpretation of this metric is a particle that emits radiation anisotropically in varying directions, so the particle accelerates arbitrarily in three dimensions. The $\epsilon \leq 0$ cases are then interpreted as singular 2-surfaces that emit radiation. [41]

3.8.4 Kantowski-Sachs Type Szekeres

The KS-type Szekeres metric, often referred to as the $\beta_{,z} = 0$ case, was shown in [41] to be a regular limit of the LT type ($\beta_{,z} \neq 0$) Szekeres metric (3.1), by choosing certain forms for the arbitrary functions, and taking the limit $f \to -\epsilon$. Defining the arbitrary functions in (3.2) to be [35]

$$A = \int \frac{1}{2} U(r) \sqrt{\epsilon + f} dr - \frac{1}{4} f, \tag{3.63}$$

$$B_1 = \int \frac{1}{2} V_1(r) \sqrt{\epsilon + f} dr, \qquad B_1 = \int \frac{1}{2} U(r) \sqrt{\epsilon + f} dr, \tag{3.64}$$

$$C = \int 2W(r) \sqrt{\epsilon + f} dr + 1, \tag{3.65}$$

$$M = M_1 \int X(r) \sqrt{\epsilon + f} dr + M_0, \tag{3.66}$$

$$t_b = \int t_{b1}(r) \sqrt{\epsilon + f} dr + t_{b0}, \tag{3.67}$$

and choosing the functions $t_{b1}(r)$, $U(r)$, $V_1(r)$, $V_2(r)$, $W(r)$ and $X(r)$ such that, in the limit, both $(R' - RE'/E)$ and $(\epsilon + f)$ go to zero together (thus ensuring the g_{rr} component of the metric remains finite), and then taking the limit

$$f \to -\epsilon, \tag{3.68}$$

one finds a metric of the form

$$ds^2 = -dt^2 + \left(\lambda + R \frac{E_1}{E_0} \right) dr^2 + \frac{R^2}{E_0^2} (dp^2 + dq^2) \tag{3.69}$$

where

$$E_1 \equiv 1 + \frac{1}{4} \epsilon (p^2 + q^2), \tag{3.70}$$

$$E_0 \equiv \frac{1}{2} U(r)(p^2 + q^2) + V_1(r) p + V_2(r) q + 2W(r), \tag{3.71}$$

and the evolution for a particular value of f is given by

$$\epsilon = +1 = -f: \qquad \lambda(t) = 2M_1 - (M_1\eta + \sigma t_{b1})\frac{\sin\eta}{1-\cos\eta} \tag{3.72}$$

$$\epsilon = 0 = f: \qquad \lambda(t) = \frac{M_1}{6}\eta^2 - \frac{2\sigma t_{b1}}{\eta} \tag{3.73}$$

$$\epsilon = -1 = -f: \qquad \lambda(t) = -2M_1 + (M_1\eta - \sigma t_{b1})\frac{\sinh\eta}{\cosh\eta - 1} \tag{3.74}$$

The metric (3.69) is KS-type Szekeres metric, thus unifying the two Szekeres metric types, showing that the KS-type metric is a special case of the LT-type.

4

Towards a Model Construction Procedure

In order to construct realistic Szekeres models one must specify the arbitrary functions associated with the model from some physical quantities. These functions, of which there are six in total, allow for a rescaling of the r coordinate, $\tilde{r} = \tilde{r}(r)$, plus five physical degrees of freedom to model inhomogeneity. By making a suitable coordinate choice the number of independent functions which must be specified is reduced to five. The LT arbitrary functions that are common to Szekeres models, f, M and t_b, will be found using a method similar to that of [27] (see §2.5), but, with a different coordinate choice. Determination of the remaining three functions, S P and Q, will require further information about the dipole orientation and intensity. Once one has obtained expressions for these six functions the Szekeres model will be completely specified. Special attention must be paid to the origin as certain variables have a value of zero there.

The first section of this chapter will outline what was done to arrive at analytic expressions for the three arbitrary functions, S, P and Q, in terms of some physically intuitive quantities. The second section investigates the origin behaviour of these expressions and the requirements to avoid their divergence. The third section will present a summary of the model construction algorithm.

4.1 Coordinate Choice

While it is convenient, when constructing LT models, to choose the mass function as a radial coordinate (see §2.5.1), we find, when constructing Szekeres models, it is more convenient to choose the areal radius, i.e.

$$\tilde{r} = R(t_2, r), \tag{4.1}$$

and thus

$$R'|_{t=t_2} = 1. \tag{4.2}$$

There are a couple of reasons why this choice is preferable. Firstly, the origin limit calculations for E'/E, shown in §4.3, are simpler when $R' = 1$. And secondly, the choice is less restrictive on the allowable density profiles which produce a finite origin value of E'/E.[1] This choice allows one to write the terms with 'radial' derivatives instead with respect to R_2, as

$$\frac{\partial}{\partial r} = \frac{\partial}{\partial R_2}, \tag{4.3}$$

and, hence, common terms like R' and M' are then given by

$$R' = \frac{\partial R}{\partial R_2} \tag{4.4}$$

and

$$M' = \frac{\partial M}{\partial R_2} \tag{4.5}$$

4.2 Obtaining the Arbitrary Functions

Since the expression for the Szekeres equatorial density (3.42) corresponds exactly with the LT density expression (2.5), and the dynamics of R are identical in both Szekeres (3.7) and LT models (2.4), the well known LT model construction procedure of Krasinski & Hellaby can be used to determine the arbitrary functions which are common in both models. Thus, specifying a Szekeres equatorial density profile (which, in the context of Szekeres models, we hereafter refer to as the LT-density) at some initial and final time,

[1] The reason for this will become clear in §4.2.3, where we derive an expression for E'/E in terms of the density profiles

t_1 and t_2, is sufficient to determine the arbitrary functions M, f and t_b according to the procedure described in §2.5. The arbitrary functions S, P and Q require further knowledge of the intensity and orientation of the dipole. These dipole parameters can be specified on only one of the 3-surfaces, t_1 or t_2 - we choose to do it at the later time as we expect one would know more about density detail at later times. Defining the density extrema on a particular shell to be

$$\rho_{min} \equiv \min_{\theta,\phi,r=const} [\rho(t_2, r, \theta, \phi)] \tag{4.6}$$

and

$$\rho_{max} \equiv \max_{\theta,\phi,r=const} [\rho(t_2, r, \theta, \phi)] \tag{4.7}$$

we specify the following:

- $\rho_{LT,1}(R_1)$ LT-density profile at $t = t_1$
- $\rho_{LT,2}(R_2)$ LT-density profile at $t = t_2$
- $\rho_{min}(R_2)$ Density minimum profile at $t = t_2$
- $\theta_{\rho_{min}}(R_2)$ Density minimum orientation angle, θ, at $t = t_2$
- $\phi_{\rho_{min}}(R_2)$ Density minimum orientation angle, ϕ, at $t = t_2$

From these quantities we will extract expressions for the six arbitrary metric functions, M, f, t_b, S, P and Q. This was done in two phases, concurrently. Namely, describing the E'/E dipole in terms of the density dipole (§4.2.3), and relating S, P and Q to E'/E and the orientation of the density dipole (§4.2.4). Before that work is presented, a small modification the LT model construction procedure is given (§4.2.1), and some initial misconceptions are mentioned (§4.2.2).

4.2.1 Finding M f and t_b

Since we choose the radial coordinate (4.1) and specify the input profiles as a function of R, in order to determine the arbitrary functions M, f and t_b, a slight modification to the LT model construction algorithm of Krasinski & Hellaby is necessary. An expression

relating the mass function, M, to the LT density is required. By rearranging (3.42) and integrating over R, one finds

$$M(t_i, R) = M_{min} + \frac{\kappa}{2}\int_{R_{min}}^{R} \rho_{LT,i} R^{*2} dR^* \qquad i = 1, 2, \tag{4.8}$$

though M_{min} and R_{min} will typically be zero, unless there is a central black hole. Since M values connect corresponding r shells at t_1 and t_2, evaluating (4.8) allows one to determine the corresponding values of R_1 and R_2. The procedure for finding f and t_b follows exactly as described in §2.5.2 from (2.52).

4.2.2 A Misconception

Previous literature ([46] - Equation 69) claimed to show the derivative of the density with respect to E'/E to be negative (i.e. $\rho_{,x} < 0$ with $x = E'/E$), implying that E'/E is a minimum at a density maximum, and a maximum at a density minimum. Moreover, since E'/E is antisymmetric (see §3.5.1), it implies that a density maximum corresponds to a negative E'/E value, and a density minimum to a positive E'/E (i.e. $E'/E|_{\rho_{max}} = E'/E|_{min} \leq 0$ and $E'/E|_{\rho_{min}} = E'/E|_{max} \geq 0$). This is in fact not the case [1]. Taking the derivative of the density (3.8) with respect to $x = E'/E$, we find

$$\begin{aligned}
\rho_{,x} &= \frac{2}{\kappa R^2}\left[\frac{-3M(R' - Rx) + R(M' - 3Mx)}{(R' - Rx)^2}\right] \\
&= \frac{2}{\kappa R^2}\left[\frac{M'R - 3MR'}{(R' - Rx)^2}\right] \\
&= RR'\frac{2}{\kappa R^3 R'}\left[\frac{M'R - 3MR'}{(R' - Rx)^2}\right] \\
&= RR'\left[\frac{\frac{2M'}{\kappa R^2 R'} - \frac{6M}{\kappa R^3}}{(R' - Rx)^2}\right] \\
&= RR'\left[\frac{(\rho_{LT} - \rho_{AV})}{(R' - Rx)^2}\right]
\end{aligned} \tag{4.9}$$

Clearly the sign of $\rho_{,x}$ is not always negative, as was previously thought, but rather it depends on the sign of $R'(\rho_{LT} - \rho_{AV})$, since $R/(R' - Rx)^2 > 0$ always holds. Thus, $E'/E|_{max}$ only occurs at the density minimum if $R'(\rho_{LT} - \rho_{AV}) < 0$.

[1] It took a number of unproductive calculations before this error was realised.

4.2.3 Solving for E'/E

In order to express E'/E in terms of density parameters, we begin by rearranging (3.8) such that E'/E is the subject, and one finds

$$\left(\frac{E'}{E}\right) = \frac{\kappa\rho R^2 R' - 2M'}{\kappa\rho R^3 - 6M}. \tag{4.10}$$

Now, dividing both numerator and denominator by κR^3 and substituting in (3.48) and (3.42), leads to

$$\begin{aligned}\Rightarrow \left(\frac{E'}{E}\right) &= \frac{\rho(\frac{R'}{R}) - \frac{2M'}{\kappa R^2 R'}(\frac{R'}{R})}{\rho - \frac{6M}{\kappa R^3}} \\ &= \frac{R'}{R}\left(\frac{\rho - \rho_{LT}}{\rho - \rho_{AV}}\right).\end{aligned} \tag{4.11}$$

It follows that E'/E at the density minimum can now easily be calculated by substituting $\rho = \rho_{min}$ into (4.11). This gives

$$\left(\frac{E'}{E}\right)_{\rho_{min}} = \frac{R'}{R}\left(\frac{\rho_{min} - \rho_{LT}}{\rho_{min} - \rho_{AV}}\right). \tag{4.12}$$

The anti-symmetric property of E'/E (3.37) allows one to express $E'/E|_{max}$ in terms of $E'/E|_{\rho_{min}}$, regardless of the sign of $R'(\rho_{LT} - \rho_{AV})$, as

$$\begin{aligned}\left(\frac{E'}{E}\right)_{max} &= \left|\left(\frac{E'}{E}\right)_{\rho_{min}}\right| \\ &= \left|\frac{R'}{R}\left(\frac{\rho_{min} - \rho_{LT}}{\rho_{min} - \rho_{AV}}\right)\right|.\end{aligned} \tag{4.13}$$

However, when relating the orientation angles of the density-dipole to the E'/E dipole, it is necessary to track the sign of $R'(\rho_{LT} - \rho_{AV})$. Since the poles of E'/E (and ρ) are antipodes on the 2-sphere, the orientation angles are easily related.

$$\begin{aligned}R'(\rho_{LT} - \rho_{AV}) > 0: \qquad & \theta_{max} = \pi - \theta_{\rho_{min}}, && \phi_{max} = \pi + \phi_{\rho_{min}} \\ & \sin\theta_{max} = \sin\theta_{\rho_{min}}, && \sin\phi_{max} = -\sin\phi_{\rho_{min}} \\ & \cos\theta_{max} = -\cos\theta_{\rho_{min}}, && \cos\phi_{max} = -\cos\phi_{\rho_{min}}\end{aligned} \tag{4.14}$$

$$\begin{aligned}R'(\rho_{LT} - \rho_{AV}) < 0: \qquad & \theta_{max} = \theta_{\rho_{min}}, && \phi_{max} = \phi_{\rho_{min}} \\ & \sin\theta_{max} = \sin\theta_{\rho_{min}}, && \sin\phi_{max} = \sin\phi_{\rho_{min}} \\ & \cos\theta_{max} = \cos\theta_{\rho_{min}}, && \cos\phi_{max} = \cos\phi_{\rho_{min}}\end{aligned} \tag{4.15}$$

We now have expressions for $E'/E|_{max}$, θ_{max}, ϕ_{max} as functions of r in terms of the physical quantities ρ_{LT}, ρ_{AV}, ρ_{min}, $\theta_{\rho_{min}}$ and $\phi_{\rho_{min}}$ at time t_2. We can thus go on to define the arbitrary functions, S, P and Q, using these expressions.

4.2.4 Solving for S, P and Q

Equations (3.39), (3.40) and (3.38) suggest that the radial derivatives of the three arbitrary functions, S', P' and Q', can be solved for in terms of the dipole orientation angles, θ_{max} and ϕ_{max}, and E'/E_{max}, since there are three equations and three unknowns. The metric functions, S P and Q, can then found by integrating the expressions for S', P' and Q' over a suitable radial coordinate. The resulting expressions will then contain quantities θ_{max}, ϕ_{max} and $E'/E|_{max}$, which can be related to the more physically intuitive quantities at the density minimum using the relations found in (4.13), (4.14) and (4.15). Solving the system of equations (3.39) (3.40) (3.38), we find the following.

Multiplying (3.38) by S, squaring both sides and rearranging leads to

$$\left(\frac{E'}{E}\right)^2_{max} S^2 = P'^2 + Q'^2 + S'^2$$
$$\Rightarrow S' = \pm\sqrt{\left(\frac{E'}{E}\right)^2_{max} S^2 - P'^2 - Q'^2} \tag{4.16}$$

Substituting this expression (4.16) into (3.40) eliminates the S' terms, to give

$$\cos\theta_{max} = \frac{\mp\sqrt{\left(\frac{E'}{E}\right)^2_{max} S^2 - P'^2 - Q'^2}}{\sqrt{P'^2 + Q'^2 + \left(\frac{E'}{E}\right)^2_{max} S^2 - P'^2 - Q'^2}}$$
$$= \frac{\mp\sqrt{\left(\frac{E'}{E}\right)^2_{max} S^2 - P'^2 - Q'^2}}{\left(\frac{E'}{E}\right)_{max} S} \tag{4.17}$$

Multiplying (4.17) by the RHS denominator, squaring and rearranging yields an expression for Q'^2 in term of only P'. One finds

$$\Rightarrow \cos\theta^2_{max}\left(\frac{E'}{E}\right)^2_{max} S^2 = \left(\frac{E'}{E}\right)^2_{max} S^2 - P'^2 - Q'^2$$
$$\Rightarrow Q'^2 = \left(\frac{E'}{E}\right)^2_{max} S^2(1 - \cos\theta^2_{max}) - P'^2$$
$$\Rightarrow Q'^2 = \left(\frac{E'}{E}\right)^2_{max} S^2 \sin\theta^2_{max} - P'^2 \tag{4.18}$$

Now Q'^2 can be entirely eliminated from (3.39) by substituting into it the expression obtained above (4.18), which gives

$$\begin{aligned}\cos\phi_{max} &= -\frac{P'}{\sqrt{P'^2 + \left(\frac{E'}{E}\right)^2_{max} S^2 \sin\theta^2_{max} - P'^2}} \\ &= -\frac{P'}{\left(\frac{E'}{E}\right)_{max} S \sin\theta_{max}}\end{aligned} \tag{4.19}$$

Rearranging (4.19) then gives an expression for P'

$$\Rightarrow P' = -\sin\theta_{max}\cos\phi_{max}\left(\frac{E'}{E}\right)_{max} S \tag{4.20}$$

By substituting this expression (4.20) into (3.39) one eliminates P', and finds

$$\cos\phi_{max} = \frac{\sin\theta_{max}\cos\phi_{max}\left(\frac{E'}{E}\right)_{max} S}{\sqrt{Q'^2 + \sin\theta^2_{max}\cos\phi^2_{max}\left(\frac{E'}{E}\right)^2_{max} S^2}} \tag{4.21}$$

An expression for Q' is now obtained by multiplying (4.21) by the denominator, squaring and rearranging, to give

$$\begin{aligned}&\Rightarrow Q'^2 + \sin\theta^2_{max}\cos\phi^2_{max}\left(\frac{E'}{E}\right)^2_{max} S^2 = \sin\theta^2_{max}\left(\frac{E'}{E}\right)^2_{max} S^2 \\ &\Rightarrow Q'^2 = \sin\theta^2_{max}\left(\frac{E'}{E}\right)^2_{max} S^2(1-\cos\phi^2_{max}) \\ &\Rightarrow Q' = \epsilon_3 \sin\theta_{max}\sin\phi_{max}\left(\frac{E'}{E}\right)_{max} S \qquad \epsilon_3 = \pm 1\end{aligned} \tag{4.22}$$

From (3.40) one can write S' as

$$S' = -\cos\theta_{max}\sqrt{P'^2 + Q'^2 + S'^2} \tag{4.23}$$

And from (3.38) one express the $\sqrt{P'^2 + Q'^2 + S'^2}$ term as:

$$\sqrt{P'^2 + Q'^2 + S'^2} = \left(\frac{E'}{E}\right)_{max} S \tag{4.24}$$

Now, substituting (4.24) into (4.23) yields an expression for S':

$$S' = -\cos\theta_{max}\left(\frac{E'}{E}\right)_{max} S \tag{4.25}$$

In (3.39 - 3.38) the Q' terms are all squared and as a result, the sign of Q' in (4.22) is undetermined. To lift this degeneracy one requires another expression containing Q'. Using (3.30) to resolve the sign, one obtains

$$\begin{aligned}\tan\phi_{max} &= \frac{Q'}{P'} \\ &= \frac{\epsilon_3 \sin\phi_{max} \sin\theta_{max} \left(\frac{E'}{E}\right)_{max} S}{-\cos\phi_{max} \sin\theta_{max} \left(\frac{E'}{E}\right)_{max} S} \\ &= -\epsilon_3 \tan\phi_{max} \end{aligned} \tag{4.26}$$

It is clear from (4.26) that $\epsilon_3 = -1$. Hence the final equations for S', P' and Q' are given by

$$S' = -\cos\theta_{max} \left(\frac{E'}{E}\right)_{max} S \tag{4.27}$$

$$P' = -\cos\phi_{max} \sin\theta_{max} \left(\frac{E'}{E}\right)_{max} S \tag{4.28}$$

$$Q' = -\sin\phi_{max} \sin\theta_{max} \left(\frac{E'}{E}\right)_{max} S \tag{4.29}$$

Expressions for the three arbitrary functions, $S(r)$ $P(r)$ and $Q(r)$, are now easily obtained by integrating (4.27), (4.28) and (4.29) over the 'radial' coordinate. For the function $S(r)$, from (4.27), one can write

$$\frac{dS}{S} = -\cos\theta_{max} \left(\frac{E'}{E}\right)_{max} dr \tag{4.30}$$

which is the standard form of a 1^{st} order separable ODE, the solution to which is

$$S(r) = S_0 \exp\left[-\int_{r_{min}}^{r} \cos\theta_{max} \left(\frac{E'}{E}\right)_{max} dr\right] \tag{4.31}$$

with

$$S(r_{min}) = S_0 \tag{4.32}$$

Since a constant rescaling of S has no physical effect on the metric, one is free to choose the value of S_0. For simplicity, we will use $S_0 = 1$.

The function $P(r)$ is found by integrating (4.28) directly, which gives

$$\begin{aligned} P(r) &= \int_{r_{min}}^{r} P' dr \\ &= -\int_{r_{min}}^{r} \cos\phi_{max} \sin\theta_{max} \left(\frac{E'}{E}\right)_{max} S dr \end{aligned} \tag{4.33}$$

Similarly, $Q(r)$ is found by integrating (4.29) to give

$$\begin{aligned} Q(r) &= \int_{r_{min}}^{r} Q' dr \\ &= -\int_{r_{min}}^{r} \sin\phi_{max} \sin\theta_{max} \left(\frac{E'}{E}\right)_{max} S dr \end{aligned} \tag{4.34}$$

One must first determine the function $S(r)$, as it appears in the integrands of both $P(r)$ and $Q(r)$. Since all the quantities in the integrands of (4.33), (4.34) and (4.31) are specified in terms of R_2, it is sensible to integrate these expressions over the same radial coordinate. The final expression for $S(R_2)$, $P(R_2)$ and $Q(R_2)$ are then given by

$$S(R_2) = S_0 \exp\left[-\int_{R_{min}}^{R_2} \cos\theta_{max} \left(\frac{E'}{E}\right)_{max} dR_2^*\right] \tag{4.35}$$

$$P(R_2) = -\int_{R_{min}}^{R_2} \cos\phi_{max} \sin\theta_{max} \left(\frac{E'}{E}\right)_{max} S dR_2^* \tag{4.36}$$

$$Q(R_2) = -\int_{R_{min}}^{R_2} \sin\phi_{max} \sin\theta_{max} \left(\frac{E'}{E}\right)_{max} S dR_2^* \tag{4.37}$$

Having obtained analytic expressions for the metric functions in terms of physical quantities, one can completely determine the Szekeres metric. While the quantities θ_{max}, ϕ_{max} and $(E'/E)_{max}$ are not physical, they are related to the physical quantities $\theta_{\rho_{min}}$, $\phi_{\rho_{min}}$, ρ_{min}, ρ_{LT} and ρ_{AV}, as was shown in §4.2.3.

4.3 Origin Behaviour

It is important to pay special attention to the origin behaviour of various quantities as it is normal for certain variables to take on a value of zero there. This is undesirable when calculating quantities numerically as it is common to find $0/0$. In this section we find analytic expressions for the origin values of these quantities in terms of non-zero variables, thereby allowing for numerical calculation.

4.3.1 E'/E and the Deviation function

As the origin is approached, by l'Hopital's rule $\rho_{AV} \to \rho_{LT}$, and we also expect $\rho_{min} \to \rho_{LT}$ since a pointlike dipole seems unphysical. Thus, it is apparent from (4.13) that the origin value of $(E'/E)_{max}$ goes to 0/0. We wish to find the conditions that ensure this quantity is finite at the origin. This can be achieved by writing the density profiles, ρ_{LT}, ρ_{min} and ρ_{AV}, as series expansions about $r = 0$, which can then be used in (4.13) to calculate the limit as $r \to 0$. On a constant time slice we make the co-ordinate choice $r = R$, and hence $R' = 1$. The series expansions for ρ_{LT} and ρ_{min} are then given by

$$\rho_{LT} = \rho_0 + \rho_1 R + \rho_2 R^2 + \rho_3 R^3 + ... \tag{4.38}$$

$$\rho_{min} = \zeta_0 + \zeta_1 R + \zeta_2 R^2 + \zeta_3 R^3 + ... \tag{4.39}$$

Rearranging (3.42) gives an expression for M' in terms of ρ_{LT},

$$\begin{aligned} M' &= \frac{\kappa}{2}\rho_{LT} R^2 R' \\ &= \frac{\kappa}{2}[\rho_0 R^2 + \rho_1 R^3 + \rho_2 R^4 + \rho_3 R^5 + ...], \end{aligned} \tag{4.40}$$

which can be integrated to yield an expression for M,

$$\begin{aligned} M &= \frac{\kappa}{2}[\frac{1}{3}\rho_0 R^3 + \frac{1}{4}\rho_1 R^4 + \frac{1}{5}\rho_2 R^5 + \frac{1}{6}\rho_3 R^6 + ...] \\ &= \frac{\kappa}{6}[\rho_0 R^3 + \frac{3}{4}\rho_1 R^4 + \frac{3}{5}\rho_2 R^5 + \frac{3}{6}\rho_3 R^6 + ...], \end{aligned} \tag{4.41}$$

which in turn can be directly used to find the series expansion for ρ_{AV}. Substituting (4.41) into (3.48) gives

$$\begin{aligned} \rho_{AV} &= \frac{6M}{\kappa R^3} \\ &= \rho_0 + \frac{3}{4}\rho_1 R + \frac{3}{5}\rho_2 R^2 + \frac{3}{6}\rho_3 R^3 + ... \end{aligned} \tag{4.42}$$

Now, substituting the series expansions (4.38), (4.39) and (4.42) into the expression for $(E'/E)_{max}$ (4.13) and taking the limit as $r \to 0$, one finds

$$\begin{aligned} \lim_{r\to 0}\left(\frac{E'}{E}\right)_{max} &= \lim_{r\to 0}\left|\left(\frac{1}{R}\frac{\rho_{min} - \rho_{LT}}{\rho_{min} - \rho_{AV}}\right)\right| \\ &= \lim_{r\to 0}\left|\left[\frac{1}{R}\frac{(\zeta_0 - \rho_0) + (\zeta_1 - \rho_1)R + (\zeta_2 - \rho_2)R^2 + (\zeta_3 - \rho_3)R^3 + ...}{(\zeta_0 - \rho_0) + (\zeta_1 - \frac{3}{4}\rho_1)R + (\zeta_2 - \frac{3}{5}\rho_2)R^2 + (\zeta_3 - \frac{3}{6}\rho_3)R^3 + ...}\right]\right|. \end{aligned} \tag{4.43}$$

In order to avoid divergence of (4.43) it is necessary to impose the condition

$$\zeta_0 = \rho_0. \tag{4.44}$$

This condition implies that no pointlike dipole can exist at $r = 0$, if one requires a finite E'/E value there. Whether a divergent E'/E at the origin is physically acceptable or not is yet to be seen. However, since we are interested in numerical calculations, we will require a finite origin value for E'/E. Applying (4.44) to (4.43), gives

$$\lim_{r\to 0}\left(\frac{E'}{E}\right)_{max} = \lim_{r\to 0}\left|\left[\frac{(\zeta_1-\rho_1)+(\zeta_2-\rho_2)R+(\zeta_3-\rho_3)R^2+(\zeta_4-\rho_4)R^3+...}{(\zeta_1-\tfrac{3}{4}\rho_1)R+(\zeta_2-\tfrac{3}{5}\rho_2)R^2+(\zeta_3-\tfrac{3}{6}\rho_3)R^3+...}\right]\right|. \tag{4.45}$$

In order to avoid divergence of (4.45) it is necessary to impose the condition

$$\zeta_1 = \rho_1, \tag{4.46}$$

which gives

$$\lim_{r\to 0}\left(\frac{E'}{E}\right)_{max} = \lim_{r\to 0}\left|\left[\frac{(\zeta_2-\rho_2)+(\zeta_3-\rho_3)R+(\zeta_4-\rho_4)R^2+(\zeta_5-\rho_5)R^3+...}{\tfrac{1}{4}\rho_1+(\zeta_2-\tfrac{3}{5}\rho_2)R+(\zeta_3-\tfrac{3}{6}\rho_3)R+(\zeta_4-\tfrac{3}{7}\rho_4)R^3+...}\right]\right| \tag{4.47}$$

$$= \left|4\left(\frac{\zeta_2-\rho_2}{\rho_1}\right)\right| \qquad \rho_1 \neq 0. \tag{4.48}$$

So with the conditions (4.44), (4.46) and $\rho_1 \neq 0$ satisfied, E'/E will have a finite origin value given by (4.48). However, (4.46) also implies that such an arrangement would have a non-smooth central density profile, or 'cusp', since $\rho_1 \neq 0$. In the case of smooth central density one has

$$\rho_1 = 0, \tag{4.49}$$

and so in order to avoid the divergence of (4.47), one must impose the condition

$$\zeta_2 = \rho_2. \tag{4.50}$$

Applying (4.49) and (4.50) to (4.47) yields

$$\lim_{r\to 0}\left(\frac{E'}{E}\right)_{max} = \lim_{r\to 0}\left|\left[\frac{(\zeta_3-\rho_3)+(\zeta_4-\rho_4)R+(\zeta_5-\rho_5)R^2+(\zeta_6-\rho_6)R^3+...}{\tfrac{2}{5}\rho_2+(\zeta_3-\tfrac{3}{6}\rho_3)R+(\zeta_4-\tfrac{3}{7}\rho_4)R^3+(\zeta_5-\tfrac{3}{8}\rho_5)R^4+...}\right]\right| \tag{4.51}$$

$$= \left|\frac{5}{2}\left(\frac{\zeta_3-\rho_3}{\rho_2}\right)\right| \qquad \rho_2 \neq 0. \tag{4.52}$$

So, if (4.44), (4.46), (4.49) (4.50) and $\rho_2 \neq 0$ are all satisfied, the model has a smooth central density profile and the E'/E value at the origin is finite, and given by (4.52). Applying the same reasoning as above to higher orders, one finds that the limiting value, in general, is given by

$$\lim_{r\to 0}\left(\frac{E'}{E}\right)_{max} = \left|\frac{n+3}{n}\left(\frac{\zeta_{n+1}-\rho_{n+1}}{\rho_n}\right)\right| \qquad \zeta_n = \rho_n \neq 0 \tag{4.53}$$

where n is the power in R of the first non-zero term of ρ_{LT} in (4.38). This implies that for a finite E'/E origin value, one requires $\rho_{min} = \rho_{LT}$ up to n^{th} order in R. Also, for a non-zero origin limit, $\zeta_{n+1} \neq \rho_{n+1}$. In order to avoid having to choose ρ_{min} in such a way, we instead define it in terms of ρ_{LT} and a 'deviation function', as follows.

$$\rho_{min}(R) = \rho_{LT}(R)\left[1-\mu(R)\right] \tag{4.54}$$

where μ satisfies

$$0 \leq \mu(R) \leq 1 \qquad \mu(0) = 0 \tag{4.55}$$

and

$$\frac{d^i\mu}{dR^i} = 0 \qquad i = 1..n \tag{4.56}$$

Choosing any function μ in this way is sufficient to ensure that the origin value of E'/E is finite. If, in addition to (4.55) and (4.56), one has

$$\frac{d^{n+1}\mu}{dR^{n+1}} \neq 0, \tag{4.57}$$

the origin value of E'/E will be given by (4.53). Clearly, if (4.57) is not satisfied, E'/E will have an origin value of zero.

It is worth noting that the origin value of E'/E is a coordinate dependant quantity (since it contains a prime), and the treatment above is only valid for the coordinate choice $r = R$. In our original formulation we made the coordinate choice $r = M$, which turned out to be far more restrictive on the allowable density profiles which produce a finite origin value E'/E . This is explained by the differing origin behaviour of R'/R (which is a factor in the expression for E'/E) in the various coordinates. With the choice $r = R$ one has $R' = 1$, and hence $R'/R \sim 1/R$. However, since regular origins

require $M \sim R^3$ (see §3.7.2), with the choice $r = M$ one has $R' \sim M^{-\frac{2}{3}} \sim 1/R^2$ and hence $R'/R \sim 1/R^3$. So, when $r = M$ the factor $(\rho_{min} - \rho_{LT})/(\rho_{min} - \rho_{AV})$ must approach zero like R^3, and when $r = R$ it must approach zero like R. As a result, in order to approach a finite origin limit with $r = M$, the condition (4.56) must hold for $i = 1..n+2$, and thus the first allowable non-zero component of the 'deviation function' is not of order $n + 1$, but rather $n + 3$.

4.3.2 LT Density

The LT-density, ρ_{LT}, will be specified on the initial and final time slices, as was done in [27]. When considering the time evolution of the model, the value of ρ_{LT} on intermediate time slices is calculated according to (2.85). Trouble arises when trying to evaluate this expression at the origin, as it contains terms in a whose limiting value (2.81) is given in terms of ρ_{LT}. So, clearly one cannot use (2.81) to calculate $a(0)$ on intermediate time slices. An available method for calculating the evolution of a at the origin is to use the applicable one of (2.82) (2.83) and (2.84), and then use (2.85) to find the evolution of $\rho_{LT}(0)$.

4.4 Some useful expressions

4.4.1 Expressing ρ_{max} in terms of ρ_{min} and ρ_{LT}

It will be useful to have an expression for the maximum density profile, ρ_{max}, in terms of the density profiles, ρ_{min} and ρ_{LT}, and which does not involve E'/E. It is found as follows. Rearranging (4.11) such that ρ is the subject, and separating the right hand side into two terms, one finds

$$\rho = \rho_{LT} + \frac{\frac{E'}{E}(\rho_{LT} - \rho_{AV})}{\frac{R'}{R} - \frac{E'}{E}} \tag{4.58}$$

Now, evaluating (4.58) at the density maximum and exploiting the anti-symmetrical property of E'/E (3.37), leads to

$$\begin{aligned} \rho_{max} &= \rho_{LT} + \frac{\frac{E'}{E}|_{\rho_{max}}(\rho_{LT} - \rho_{AV})}{\frac{R'}{R} - \frac{E'}{E}|_{\rho_{max}}} \\ &= \rho_{LT} - \frac{\frac{E'}{E}|_{\rho_{min}}(\rho_{LT} - \rho_{AV})}{\frac{R'}{R} + \frac{E'}{E}|_{\rho_{min}}} \end{aligned} \tag{4.59}$$

Substituting (4.12) in for $E'/E|_{\rho_{min}}$, and simplifying, one finds

$$\begin{aligned}\rho_{max} &= \rho_{LT} - \frac{\frac{R'}{R}\left(\frac{\rho_{min}-\rho_{LT}}{\rho_{min}-\rho_{AV}}\right)(\rho_{LT}-\rho_{AV})}{\frac{R'}{R}+\frac{R'}{R}\left(\frac{\rho_{min}-\rho_{LT}}{\rho_{min}-\rho_{AV}}\right)} \\ &= \rho_{LT} + \frac{(\rho_{LT}-\rho_{min})(\rho_{LT}-\rho_{AV})}{(\rho_{AV}-\rho_{min})+(\rho_{LT}-\rho_{min})} \end{aligned} \tag{4.60}$$

So, by specifying the minimum and LT density profiles, $\rho_{min}(r)$ and $\rho_{LT}(r)$, one fixes the maximum density profile, $\rho_{max}(r)$.

4.4.2 Reconstructing ρ_{min} from $(E'/E)_{max}$

When reconstructing the model evolution it will be convenient to have an expression for ρ_{min} in terms of $(E'/E)_{max}$ (instead of being in terms of $(E'/E)_{\rho_{min}}$). From the analysis of §4.2.3, we can relate $(E'/E)_{\rho_{min}}$ to $(E'/E)_{max}$ as follows:

$$\left(\frac{E'}{E}\right)_{\rho_{min}} = \chi\left(\frac{E'}{E}\right)_{max} \tag{4.61}$$

where

$$\chi \equiv -\text{sign}[R'(\rho_{LT}-\rho_{AV})] \tag{4.62}$$

Hence, setting $\rho = \rho_{min}$ in (4.58), and substituting in (4.61), gives an expression for ρ_{min} in term of $(E'/E)_{max}$. One finds

$$\rho_{min} = \rho_{LT} + \frac{\chi\left(\frac{E'}{E}\right)_{max}(\rho_{LT}-\rho_{AV})}{\frac{R'}{R}-\chi\left(\frac{E'}{E}\right)_{max}}. \tag{4.63}$$

Similarly, for ρ_{max}, one can write

$$\rho_{max} = \rho_{LT} - \frac{\chi\left(\frac{E'}{E}\right)_{max}(\rho_{LT}-\rho_{AV})}{\frac{R'}{R}+\chi\left(\frac{E'}{E}\right)_{max}}. \tag{4.64}$$

So, knowing the profiles $(E'/E)_{max}(M)$, $R(t,M)$, $R'(t,M)$ and $\rho_{LT}(t,M)$ is sufficient to reconstruct the minimum and maximum density profiles, $\rho_{min}(t,M)$ and $\rho_{max}(t,M)$.

4.4.3 Approximating R_1/R_2

Since we choose to specify, at the final time, the density profiles and dipole parameters as a function of R_2, it will be useful to know the approximate range of R_1 over which to specify the initial profile, such that it contains the same mass (i.e. the same particle worldlines). Thus, an expression for R_1/R_2 is needed. Rearranging (3.48) so that R is the subject gives

$$R = \left(\frac{6M}{\rho_{AV}}\right)^{1/3}. \tag{4.65}$$

Evaluating (4.65) at the initial and final time, and dividing the two, gives an expression for R_1/R_2 in terms of ρ_{AV} at the initial and final times. One finds:

$$\frac{R_1}{R_2} = \left(\frac{\rho_{AV,2}}{\rho_{AV,1}}\right)^{1/3} \tag{4.66}$$

The internal average is, however, not known prior to integrating the specified density profile, as it requires knowledge of both R and M. Since we wish to know over what range to specify the initial density profile, prior to integration, (4.66) is not helpful. The FLRW background density, ρ_{BG}, can be used as a zeroth order approximation to the internal average. Indeed, in the flat FLRW case, they are equal. So, assuming the inhomogeneities are not too strong, we can make the rather crude approximation

$$\rho_{AV} \approx \rho_{BG}, \tag{4.67}$$

and thus (4.66) gives

$$\frac{R_1}{R_2} \approx \left(\frac{\rho_{BG,2}}{\rho_{BG,1}}\right)^{1/3}. \tag{4.68}$$

With this expression one can hence approximate the range of R_1 which contains the same mass as the specified range of R_2, without having to first integrate the density profiles.

4.5 The Algorithm

The above analysis has equipped us with the tools to construct the Szekeres model that evolves between two time slices, given initial and final density data. The procedure is

broken into two parts. Firstly, obtaining the six arbitrary functions which define the metric from the specified initial and final data. And secondly, calculating the model evolution from those arbitrary functions. To begin, one must specify the following quantities:

- $\rho_{LT,1}(R_1)$: The LT-density profile at $t = t_1$
- $\rho_{LT,2}(R_2)$: The LT-density profile at $t = t_2$
- $\mu(R_2)$: The 'deviation function' at $t = t_2$
- $\theta_{\rho_{min}}(R_2)$: The density minimum orientation angle, θ, at $t = t_2$
- $\phi_{\rho_{min}}(R_2)$: The density minimum orientation angle, ϕ, at $t = t_2$

The approximate range of $\rho_{LT,1}$ is related to that of $\rho_{LT,2}$ by (4.68). Now, the metric functions $M(R_2)$, $f(R_2)$, $t_B(R_2)$, $S(R_2)$, $P(R_2)$ and $Q(R_2)$ are obtained as follows:

Evaluate the integral (4.8) at the initial and final times, to find $M(R_1)$ and $M(R_2)$. Interpolation then gives $R_1(M)$ and $R_2(M)$, for a set of worldlines. Now, for each particle worldline (at each M value):

- Calculate the quantities $a_1(M)$, $a_2(M)$ given by (2.52). In the case where $M_{min} = 0$, the origin value, $a(0)$, is given by (2.81).
- Evaluate the inequalities (2.64) (2.67),(2.71),(2.74) (2.78), and hence determine the evolution type of that worldline.
- Determine the value of x which solves the relevant $\psi(x) = 0$ equation, (2.66) (2.70) (2.73) (2.77) (2.80). A bisection method is good for this - Refer to Table 2.2 for the initial rage over which to bisect.
- Calculate the energy function, $f(M)$, using the one of (2.65) (2.68) (2.72) (2.75) (2.79) which is applicable to the evolution type
- Calculate the bang time, $t_b(M)$, using the one of (2.53) (2.69) (2.54) (2.76) (2.55) which is applicable to the evolution type.
- Calculate the minimum density profile on the final time slice, $\rho_{min,2}$, using (4.54).

- Calculate the internal average density on the initial and final time slices, $\rho_{AV,1}(M)$ and $\rho_{AV,2}(M)$, using (3.48). The origin values are the same as the LT-density - $\rho_{AV}(0) = \rho_{LT}(0)$.
- Calculate the function $E'/E|_{max}$ on the final time slice using (4.13). The origin value is given by (4.53) if (4.57) is satisfied. If (4.57) is not satisfied, the origin value of $E'/E|_{max}$ is zero.
- Calculate the minimum density profile on the initial time slice, $\rho_{min,1}$, using (3.8).
- Calculate the maximum density profiles on the initial and final time slices, $\rho_{max,1}$ and $\rho_{max,2}$, using (4.60).
- Determine the sign of $R'(\rho_{LT} - \rho_{AV})$ at the initial and final times, and hence calculate $\sin\theta_{max}$, $\sin\phi_{max}$, $\cos\theta_{max}$ and $\cos\phi_{max}$ using either (4.14) or (4.15).
- Calculate the arbitrary function S, P and Q using (4.35), (4.36) and (4.37).
- Calculate the 'radial' derivatives, M' f' and t_b', according to (4.3), and then evaluate the shell crossing conditions given in Table 3.3 to ensure the model is well behaved.

Having determined the metric functions, one can now calculate the model evolution as follows:

- Calculate the quantity $a(M)$ on intermediate time slices using the one of (2.82) (2.83) (2.84) which is applicable to the evolution type.
- Calculate the LT-density, $\rho_{LT}(M)$, on intermediate time slices using (2.85).
- Calculate the areal radius of each world line, $R(M)$, on intermediate time slices using (2.52).
- Calculate the 'radial' derivative of the areal radius, $R'(M)$, on intermediate time slices using (4.4).
- Calculate the internal average density profile, $\rho_{AV}(M)$, on intermediate time slices using (3.48)

- Calculate the quantity $\chi(M)$ on intermediate time slices, using (4.62).
- Calculate the minimum and maximum density profiles, $\rho_{min}(M)$ and $\rho_{max}(M)$, on intermediate time slices using (4.63) and (4.64).

5

Numerical Simulations

This sections details the numerical simulations that were carried out. §5.1 gives a brief description of how the procedure was implemented. The chosen model profiles are then listed in §5.2, followed by the simulation results in §5.3.

5.1 Implementation

A script was written in MATLAB to implement the algorithm outlined in §4.5 and is included in Appendix A. Some practical aspects of the implementation are outlined below.

- Evaluation of the integral in (4.8), to obtain $M(R_1)$ and $M(R_2)$, is computed using the adaptive Gauss-Kronrod quadrature package, *quadgk*. The inverses, $R_1(M)$ and $R_2(M)$, defined over approximately the same mass rage, are then found. The function *interp1* is used to interpolate the values of R_1 at the same M values for which R_2 is defined.

- The quantities a_1 and $\rho_{AV,1}$ are best calculated using the values of R and M given by the integration of (4.8), prior to interpolation. Once a_1 and $\rho_{AV,1}$ are known, the function *interp1* is the used to interpolate values corresponding to the same M values for which R_2 is defined.

- The function m-file *solve_phi_x.m* was written to solve the various $\psi(x) = 0$ equations by the bisection method.

- Evaluation of the integral in (4.35) is computed using the ODE solver *ode45*, while the integrals in (4.36) and (4.37) are computed using the adaptive Simpson quadrature package *quad*. The function m-file *myinerpfun.m* was written so that the intergrands in (4.35) (4.36) and (4.37) are continuously defined, and thus amenable to integration with *ode45* and *quad*.

- For non-parabolic world lines, the evolution of R is not given explicitly in terms of t, but instead it is parametrized by η. This necessitates the interpolation of R on constant time slices. Along constant-M slices an $N \times 1$ vector of η-values is created ranging from η_1 to η_2 [1], allowing $R(\eta)$ and the corresponding $t(\eta)$ to be calculated. Now we have $R(t)$ for each world line, but the trouble is that the t-values do not correspond except on the initial and final surfaces. A spline cure is fitted to $R(t)$ at each M value using *spline*, allowing interpolation of $R(M)$ on constant time slices.

- Derivatives, such as $R'(t, M)$, $\dot{R}(t, M)$ and $a_{,M}(t, M)$, are computed using the package *gradient*, which uses a 3-point finite difference method.

5.2 Model Profiles

Since the aims of this thesis are to develop a model construction procedure and implement it in software, investigating elaborate models using this software is thus outside our scope. Our choice of model profiles was therefore predominantly motivated by convenience, the intention being to sufficiently demonstrate the functioning of the software. We use geometric units, in which $c = 1 = G$ and fix the scale freedom of GR by considering $10^{15} M_\odot$ to be one mass unit, as in [27]. The corresponding geometric length and time units are related by

$$M_G = 1 \Rightarrow \qquad L_G = M_G \frac{G}{c^2}, \qquad T_G = M_G \frac{G}{c^3}, \tag{5.1}$$

and thus,

$$\begin{aligned} 1M_G &= 10^{15}\, M_\odot \\ \Rightarrow 1L_G &= 48\,\text{pc}, \\ \Rightarrow 1T_G &= 156\,\text{yr}. \end{aligned} \tag{5.2}$$

[1] For regions that are recollapsing at $t = t_2$, the final phase is given by $\eta_2 = 2\pi - \arccos(1 - a_2 x)$

In all of the simulations we choose the final time to be, approximately, the current age of the Universe, and the initial time to be, approximately, the time of recombination. That is

$$t_1 = 100\,\mathrm{k\,yr} = 641\,\mathrm{T_G}, \tag{5.3}$$

$$t_2 = 10\,\mathrm{G\,yr} = 6.41 \times 10^7\,\mathrm{T_G}. \tag{5.4}$$

And, the background density at the initial and final time is then

$$\rho_{BG,1} = 8 \times 10^{-17}\,\mathrm{kg/m^3} = 1.3 \times 10^{-}7\,\mathrm{M_G/L_G^3}, \tag{5.5}$$

$$\rho_{BG,2} = 8 \times 10^{-27}\,\mathrm{kg/m^3} = 1.3 \times 10^{-}17\,\mathrm{M_G/L_G^3}. \tag{5.6}$$

In all cases, the range of R_2 over which we simulate the chosen profiles is $10^6\,T_G$, which is equivalent to 48 Mpc.

5.2.1 Run #1

We first investigate the simple case where $E'/E|_{max}(0) = 0$, and thus choose the 'deviation function' such that it does not satisfy (4.57). The chosen profiles are

$$\begin{aligned}
\rho_{LT,1}(R_1) &= \rho_{BG,1}\left(\frac{1.00003 + (8\times10^{-5})R^3}{1 + (8\times10^{-5})R^3}\right)\\
\rho_{LT,2}(R_2) &= \rho_{BG,2}\left(\frac{10^5 + 10^{-10}R^2 + 10^{-17}R^3}{10 + 10^{-10}R^2 + 10^{-17}R^3}\right)\\
\mu(R_2) &= 10^{-23}R^4\exp\left(-(4\times10^{-24})R^4\right)\\
\theta_{\rho_{min}}(R_2) &= \frac{\pi}{4}\\
\phi_{\rho_{min}}(R_2) &= \frac{\pi}{4}
\end{aligned} \tag{5.7}$$

5.2.2 Run #2

Next, we investigate the case where $E'/E|_{max}(0) \neq 0$, and thus choose the 'deviation function' such that it does satisfy (4.57). The chosen profiles are

$$\begin{aligned}
\rho_{LT,1}(R_1) &= \rho_{BG,1}\left(\frac{1.00003 + (10^{-5})R^3}{1 + (10^{-5})R^3}\right) \\
\rho_{LT,2}(R_2) &= \rho_{BG,2}\left(\frac{(5 \times 10^4) + 10^{-10}R^2 + 10^{-17}R^3}{10 + 10^{-10}R^2 + 10^{-17}R^3}\right) \\
\mu(R_2) &= 10^{-17}R^3 \exp\left(-(4 \times 10^{-18})R^3\right) \\
\theta_{\rho_{min}}(R_2) &= \frac{\pi}{4} + (\frac{\pi}{2} \times 10^{-6})R \\
\phi_{\rho_{min}}(R_2) &= (2\pi \times 10^{-6})R
\end{aligned} \tag{5.8}$$

5.2.3 Run #3

Again, we investigate the case where $E'/E|_{max}(0) \neq 0$. The chosen profiles are

$$\begin{aligned}
\rho_{LT,1}(R_1) &= \rho_{BG,1}\left(\frac{1.00003 + (8 \times 10^{-5})R^3}{1 + (8 \times 10^{-5})R^3}\right) \\
\rho_{LT,2}(R_2) &= \rho_{BG,2}(10^-5)\left(\frac{1 + (2 \times 10^{-10})R^2 + (2.9 \times 10^{-17})R^3}{10 + (2 \times 10^{-10})R^2 + (2.9 \times 10^{-17})R^3}\right) \\
\mu(R_2) &= (2.2 \times 10^{-18})R^3 \exp\left(-(1.2 \times 10^{-17})R^3\right) \\
\theta_{\rho_{min}}(R_2) &= \frac{\pi}{4} + (\frac{\pi}{2} \times 10^{-6})R \\
\phi_{\rho_{min}}(R_2) &= (2\pi \times 10^{-6})R
\end{aligned} \tag{5.9}$$

5.3 Results and Discussion

5.3.1 Run #1

The density profiles ρ_{LT}, ρ_{min}, ρ_{max} and ρ_{AV} at the initial and final times are shown in Figures 5.1 and 5.2, respectively. Both have an over-density at the origin, resulting in $\rho_{AV} > \rho_{LT}$ for all (t, r), and thus the relationship between $E'/E|_{max}$ and $E'/E|_{\rho_{min}}$ is constant. At the final time, the large deviation in ρ_{min} away from ρ_{LT} (which was specified via the function μ) causes little deviation in ρ_{max} away from ρ_{LT}. The large deviation in ρ_{min} at the final time is sourced by much smaller deviation from the initial time. The function $E'/E|_{max}$, shown in Figure 5.3, has an origin value of zero, as expected from our choice of μ. Figure 5.4 shows the LT arbitrary functions, M, f

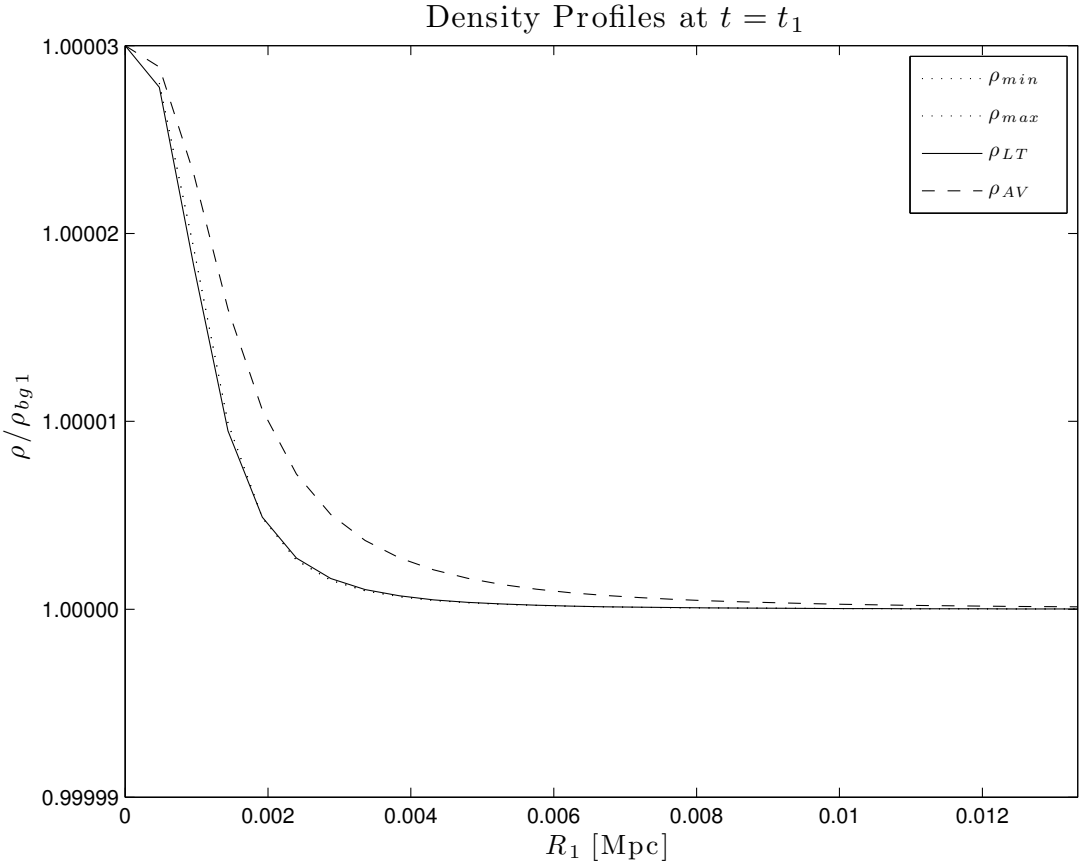

Figure 5.1: Initial Density Profiles from Run #1 - The minimum, maximum, internal average and LT density profiles at $t = t_1$ from Run #1. The LT-density was specified and the rest were calculated. (The profiles extend out to $R_1 = 0.27$)

and t_b. Since there are no regions where $\rho_{LT} = 0$, we see that M, in the top pane of Figure 5.4, is always increasing. The LT energy function in the centre pane has $f < 0$, and thus all worldlines are all elliptical. The bottom pane shows the bang time, which is decreasing close to the origin and then it becomes increasing further away. This would produce a shell crossing soon after the bang. The Szekeres arbitrary functions, S, P and Q, are shown in Figure 5.5. Surfaces showing the full time evolution of LT, minimum and maximum densities are shown in Figures 5.6 5.7 and 5.8, respectively.

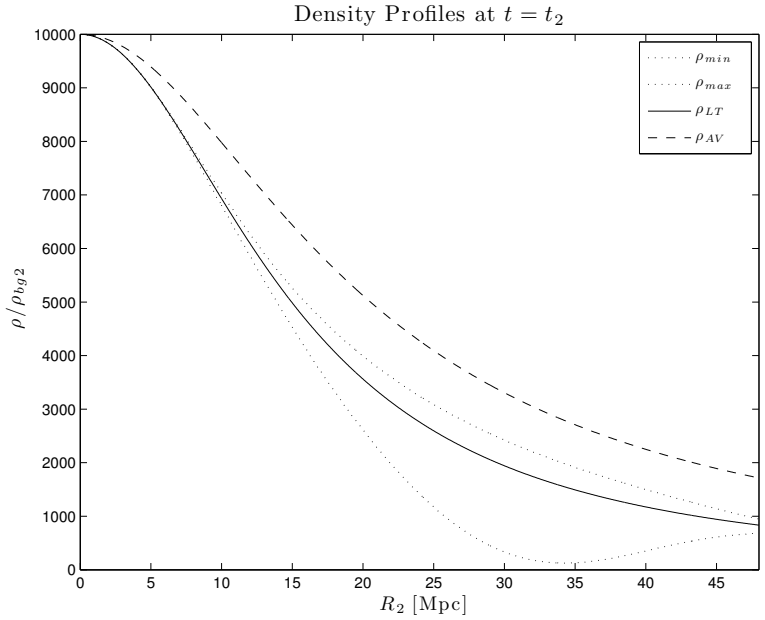

Figure 5.2: Final Density Profiles from Run #1 - The minimum, maximum, internal average and LT density profiles at $t = t_2$ from Run #1. The minimum and LT-density were specified. The rest were calculated.

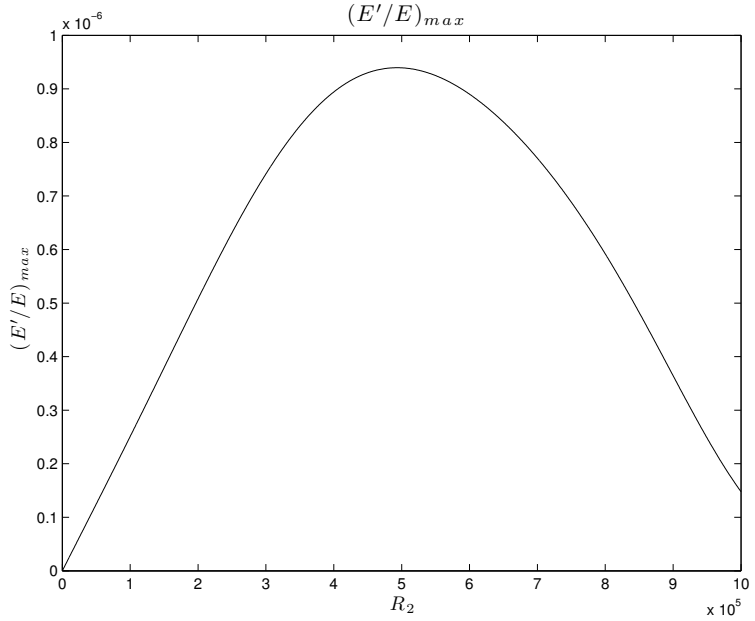

Figure 5.3: The Function $E'/E|_{max}$ from Run #1 - The dipole function $E'/E|_{max}$ from Run #1.

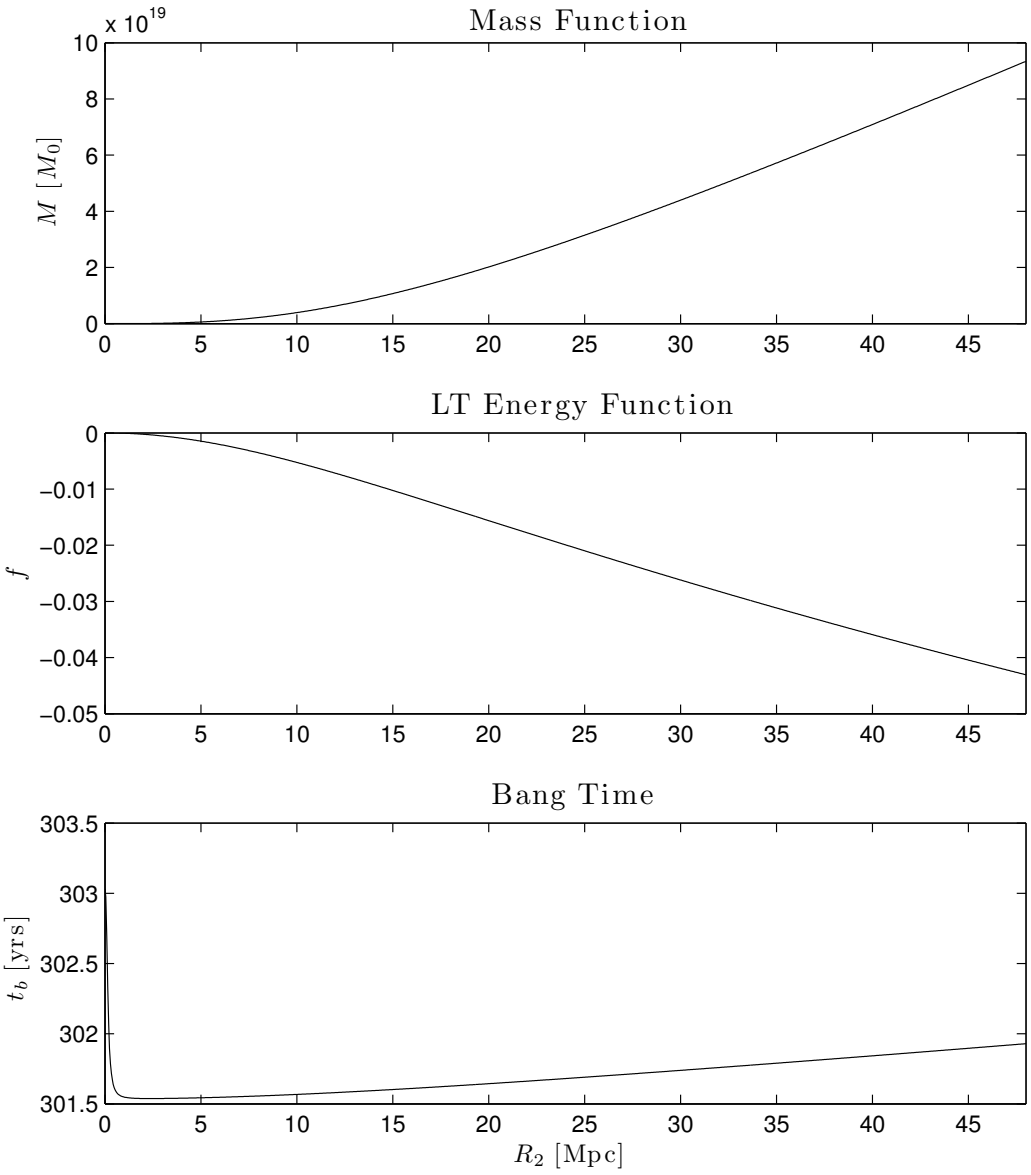

Figure 5.4: Arbitrary Functions M, f and t_b from Run #1 - The arbitrary functions which are common to both Szekeres and LT modes; M, f and t_b

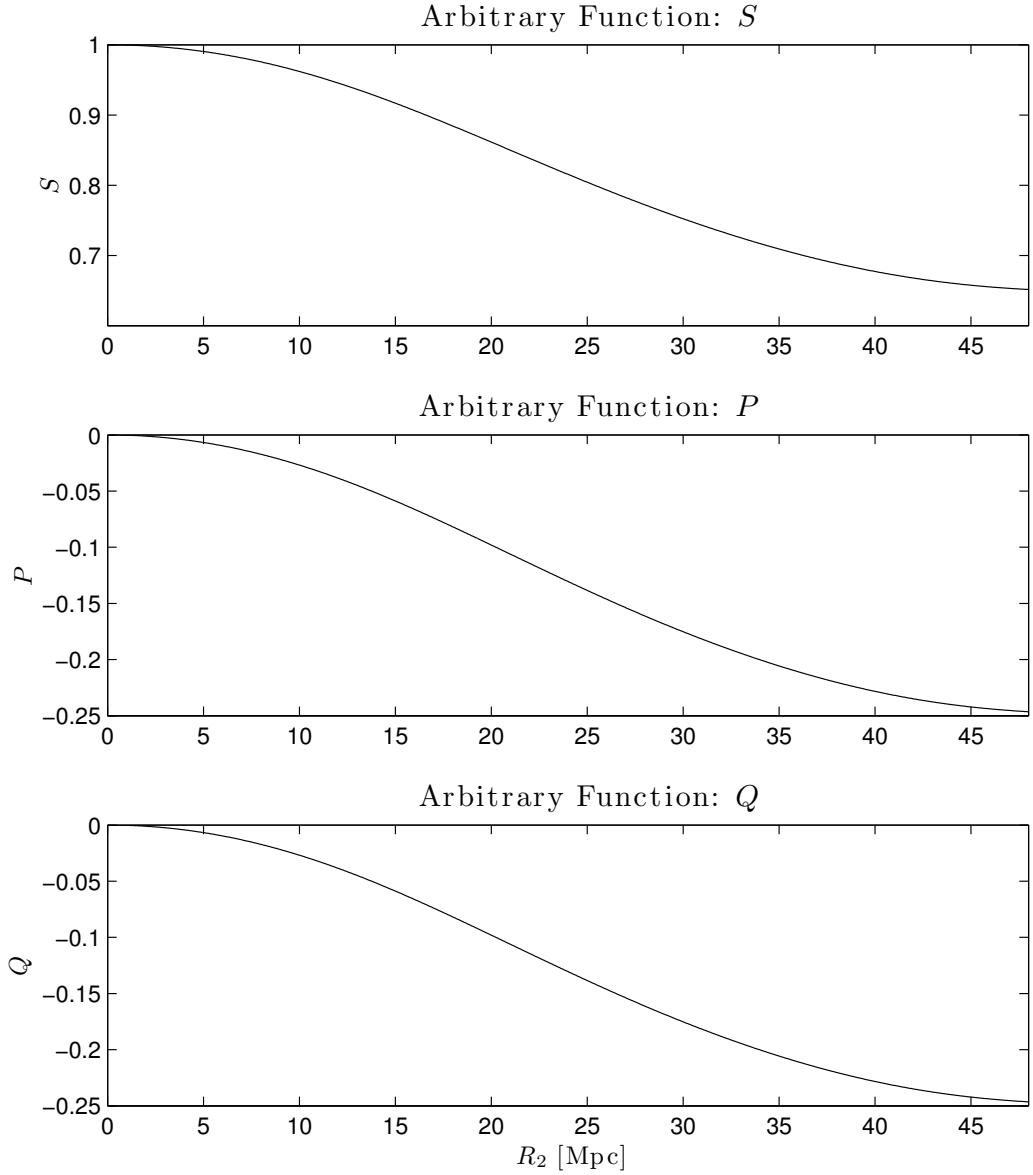

Figure 5.5: Arbitrary Functions S, P and Q from Run #1 - The arbitrary functions which are unique to Szekeres models; S, P and Q

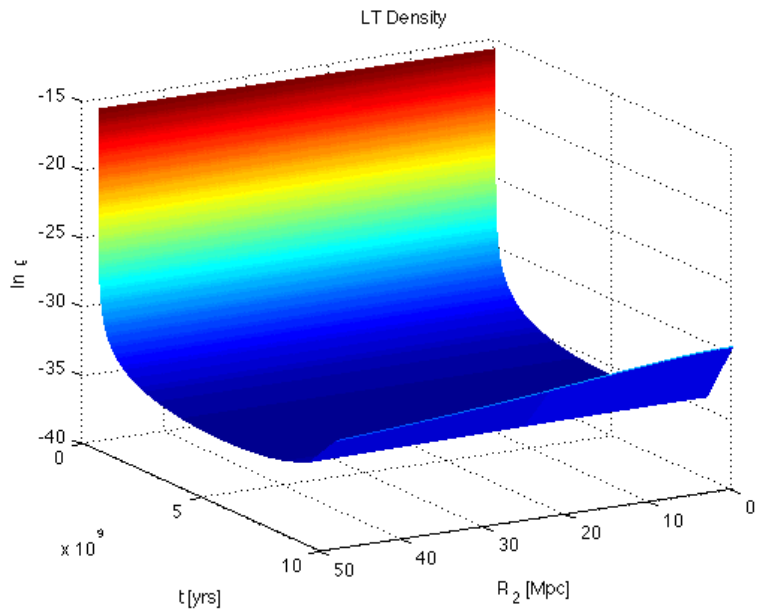

Figure 5.6: Evolution of the LT-density from Run #1 - The evolution of the LT-density profile, ρ_{LT}. Log scale

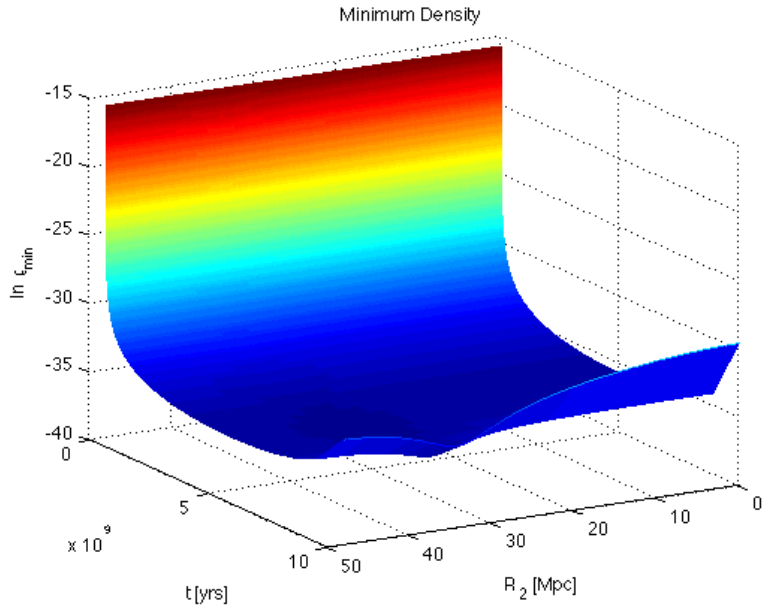

Figure 5.7: Density Dipole Minimum from Run #1 - The evolution of the density dipole minimum, ρ_{min}. Log scale

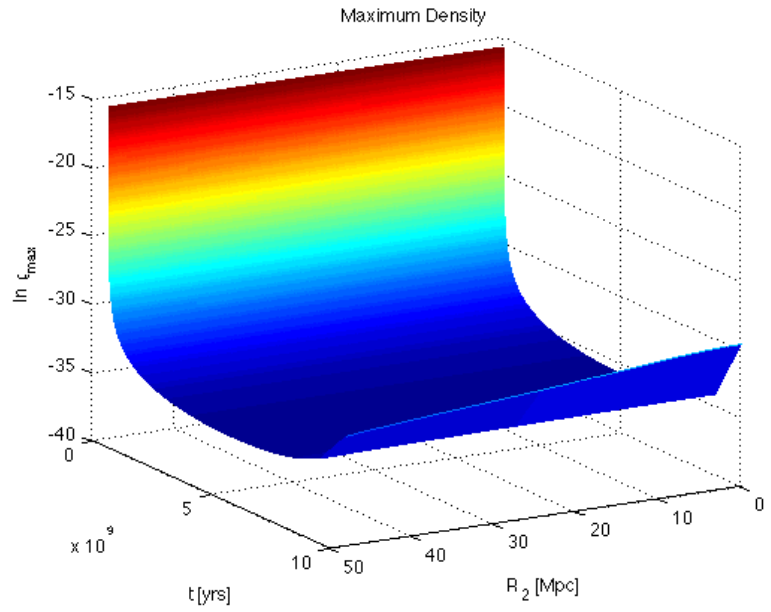

Figure 5.8: Density Dipole Maximum from Run #1 - The evolution of the density dipole maximum, ρ_{max}. Log scale

5.3.2 Run #2

The density profiles ρ_{LT}, ρ_{min}, ρ_{max} and ρ_{AV} at the initial and final times are shown in Figures 5.9 and 5.10, respectively. As in the case of Run #1, both have an over-density at the origin, resulting in $\rho_{AV} > \rho_{LT}$ for all (t, r), and thus the relationship between $E'/E|_{max}$ and $E'/E|_{\rho_{min}}$ is constant. Again, the large deviation of ρ_{min} away from ρ_{LT}, at the final time, causes little deviation of ρ_{max} away from ρ_{LT}. The function $E'/E|_{max}$, shown in Figure 5.11, approaches a finite origin value, as expected from our choice of μ. Figure 5.12 shows the LT arbitrary functions, M, f and t_b, which are similar to those from Run # 1. The Szekeres arbitrary functions, S, P and Q, are shown in Figure 5.13. The effect of varying the dipole orientation angles is evident in all of them. Surfaces showing the full time evolution of LT, minimum and maximum densities are shown in Figures 5.14, 5.15 and 5.16, respectively.

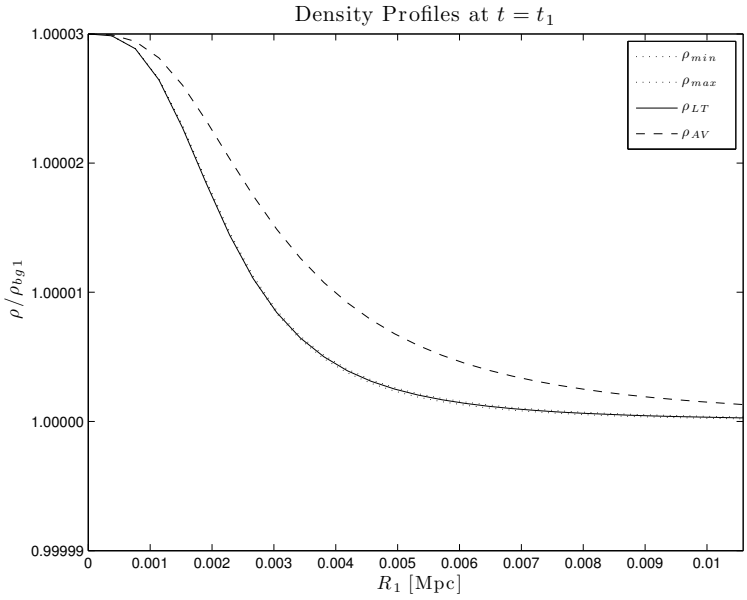

Figure 5.9: Initial Density Profiles from Run #2 - The minimum, maximum, internal average and LT density profiles at $t = t_1$ from Run #2. Only LT-density was specified. The rest were calculated. (The profiles extend out to $R_1 = 0.27$)

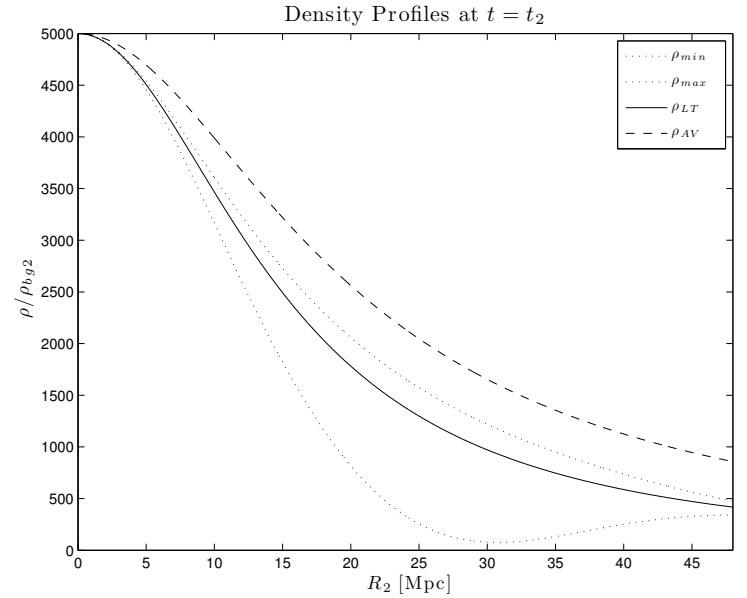

Figure 5.10: Final Density Profiles from Run #2 - The minimum, maximum, internal average and LT density profiles at $t = t_2$ from Run #2. The minimum and LT-density was specified. The rest were calculated.

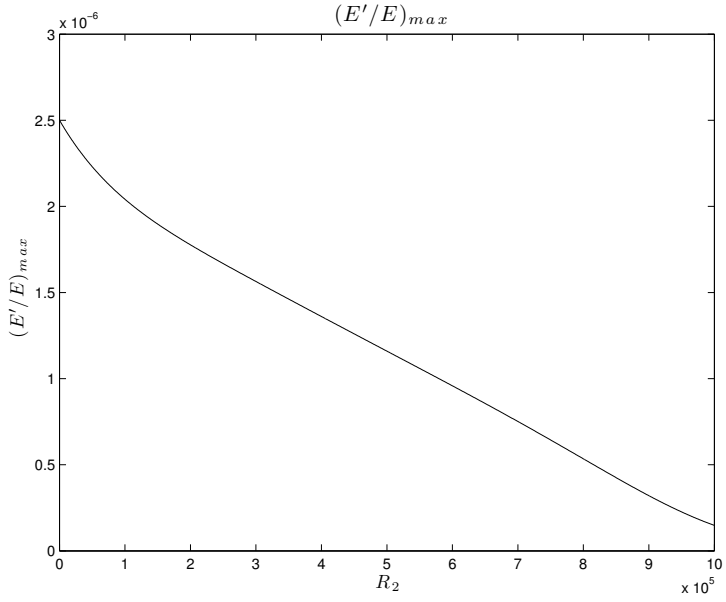

Figure 5.11: The Function $E'/E|_{max}$ from Run #2 - The dipole function $E'/E|_{max}$ from Run #2

5.3.3 Run #3

The density profiles ρ_{LT}, ρ_{min}, ρ_{max} and ρ_{AV} at the initial and final times are shown in Figures 5.17 and 5.18, respectively. Unlike the previous two cases, the initial over-density evolves into an under-density at the final time, causing the quantity $(\rho_{LT}-\rho_{AV})$ to change sign during the course of the evolution. Thus, the relationship between $E'/E|_{max}$ and $E'/E|_{\rho_{min}}$ is not constant for all (t, r) - a 'flip' takes place. At the final time, the 'deviation function ' produces a large difference between ρ_{LT} and ρ_{max}, but little between ρ_{LT} and ρ_{min}. This effect seems to be depend on the sign of $(\rho_{LT}-\rho_{AV})$. If $R'(\rho_{LT}-\rho_{AV}) > 0$, then the deviation in maximum density is enhanced as compared to the minimum density, and vice versa. Furthermore, the location of the peak in ρ_{max} corresponds to the location of the minimum in ρ_{min}, which, by definition, corresponds to the peak in the deviation function, μ. The function $E'/E|_{max}$, shown in Figure 5.19, approached a finite origin value, as expected from our choice of μ. Figure 5.20 shows the LT arbitrary functions, M, f and t_b. The Szekeres arbitrary functions, S, P and Q, are shown in Figure 5.21. Surfaces showing the full time evolution of LT, minimum and maximum densities are shown in Figures 5.22 5.23 and 5.24, respectively.

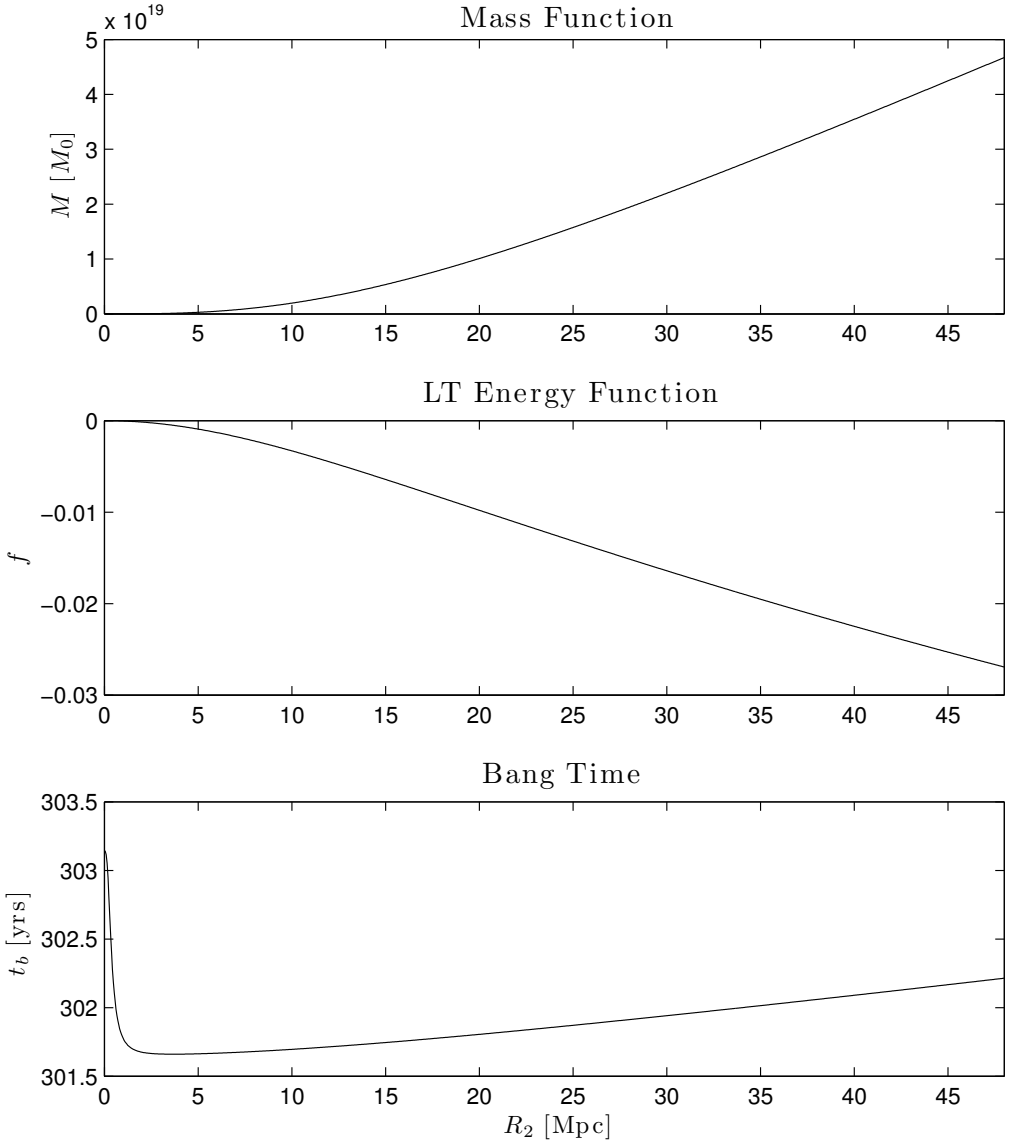

Figure 5.12: Arbitrary Functions M, f and t_b from Run #2 - The arbitrary functions which are common to both Szekeres and LT modes; M, f and t_b

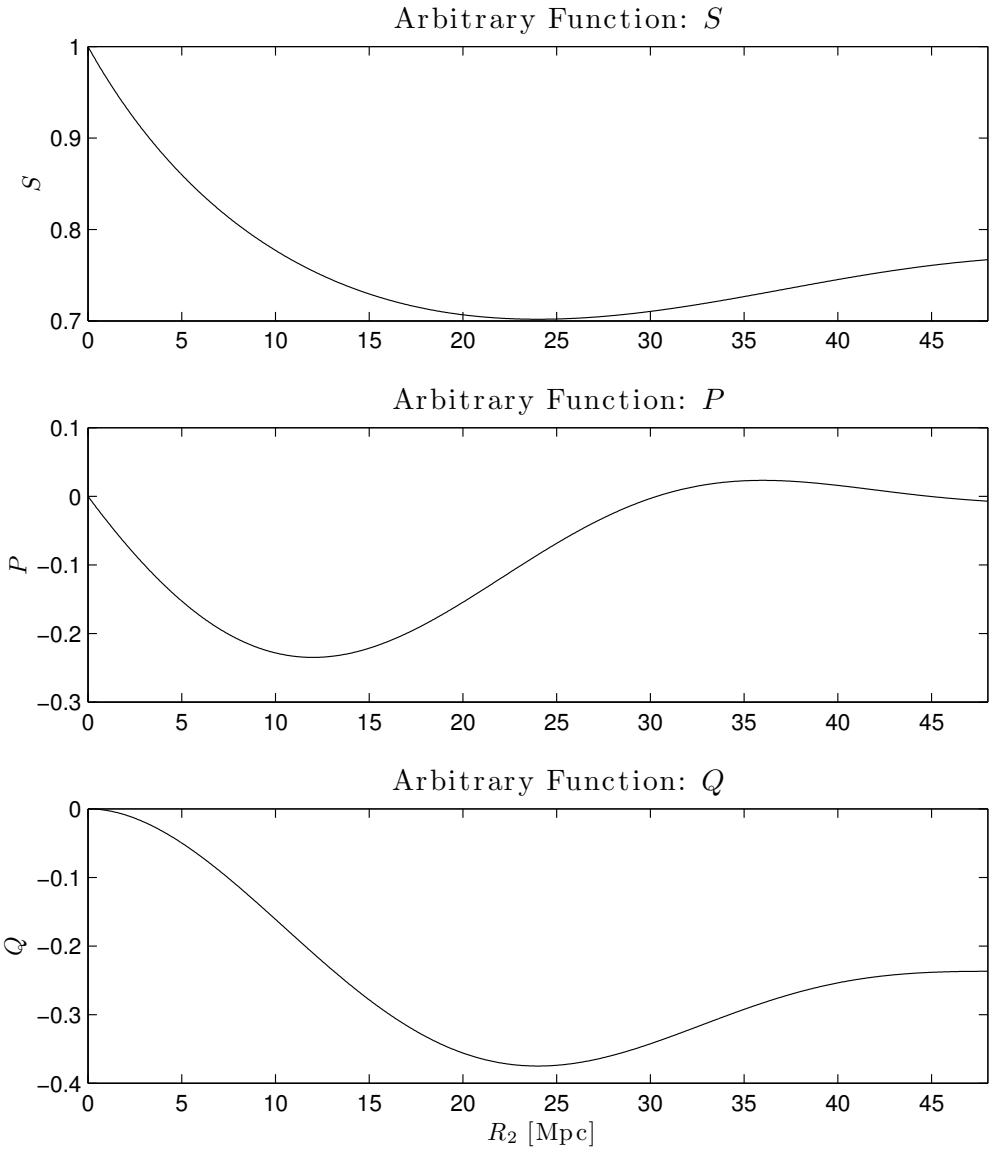

Figure 5.13: Arbitrary Functions S, P and Q from Run #2 - The arbitrary functions which are unique to Szekeres models; S, P and Q

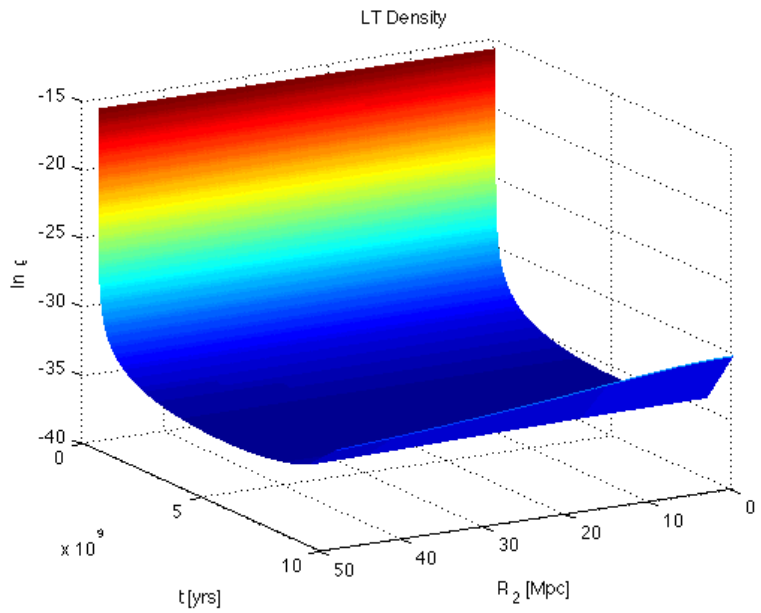

Figure 5.14: Evolution of the LT-density from Run #2 - The evolution of the LT-density profile, ρ_{LT}. Log scale

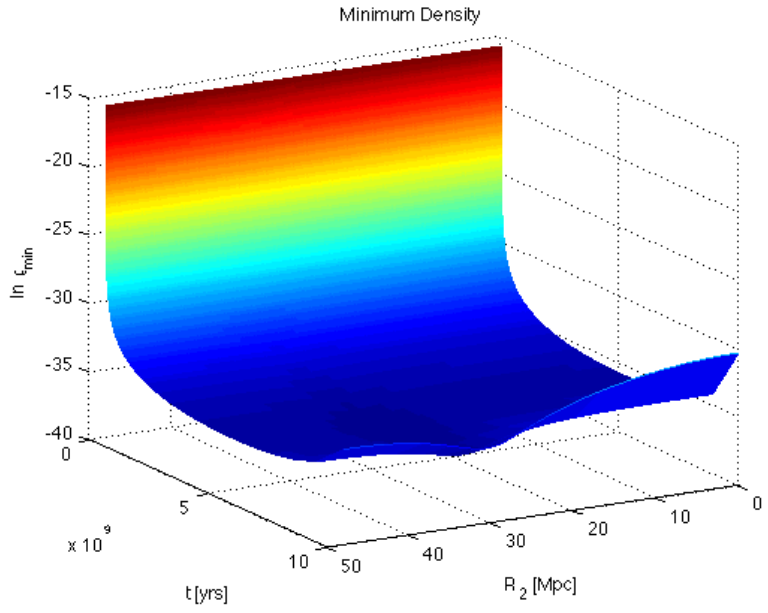

Figure 5.15: Density Dipole Minimum from Run #2 - The evolution of the density dipole minimum, ρ_{min}. Log scale

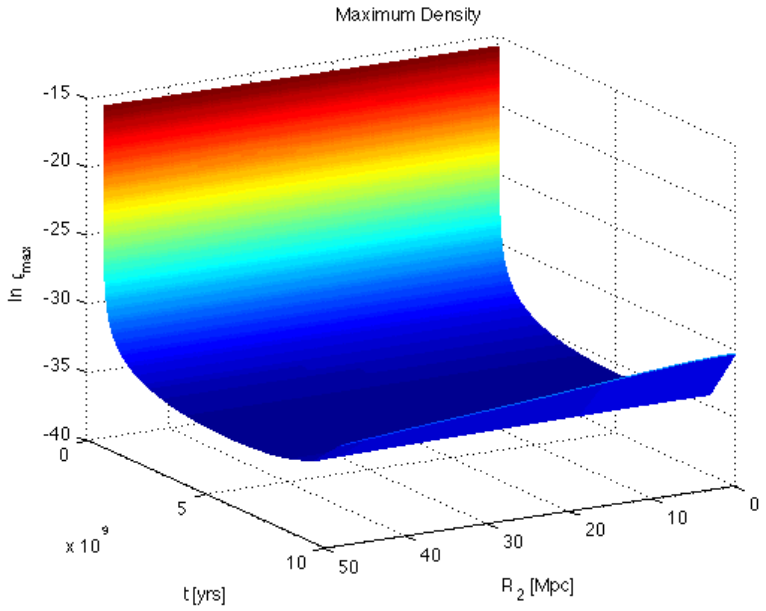

Figure 5.16: Density Dipole Maximum from Run #2 - The evolution of the density dipole maximum, ρ_{max}. Log scale

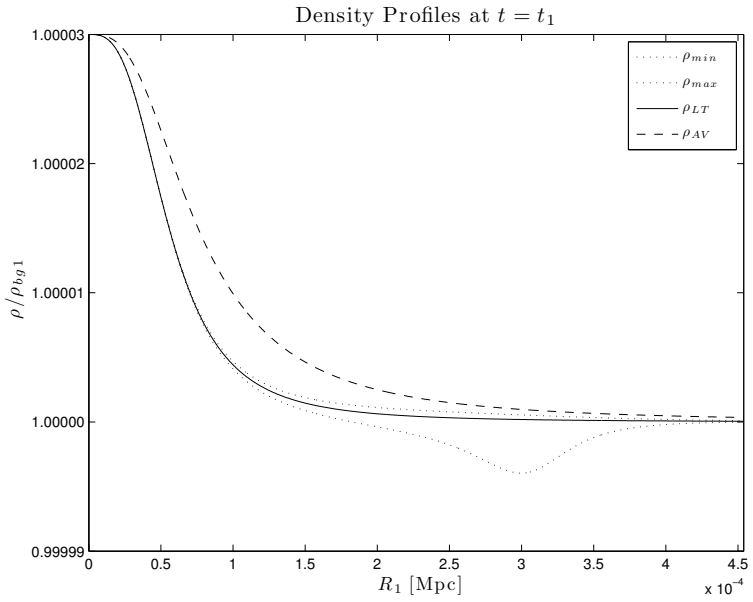

Figure 5.17: Initial Density Profiles from Run #3 - The minimum, maximum, internal average and LT density profiles at $t = t_1$ from Run #3. Only LT-density was specified. The rest were calculated.

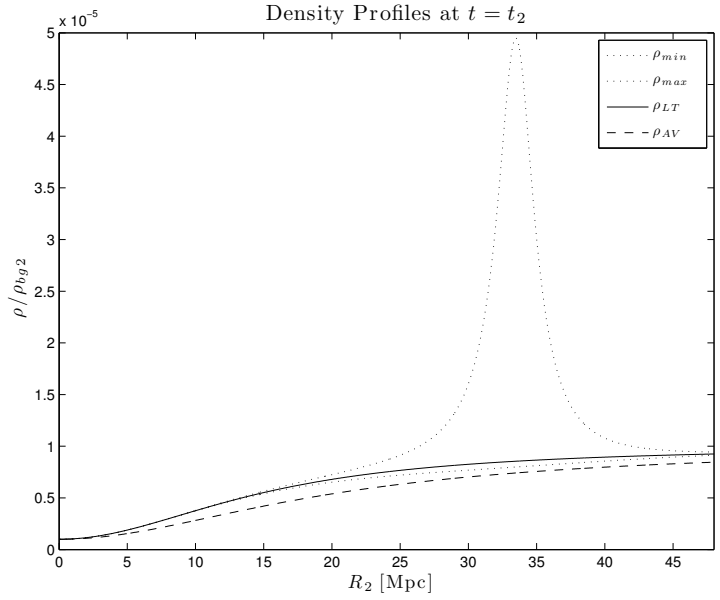

Figure 5.18: Final Density Profiles from Run #3 - The minimum, maximum, internal average and LT density profiles at $t = t_2$ from Run #3. The minimum and the LT-density was specified at t_1 and t_2. The rest were calculated.

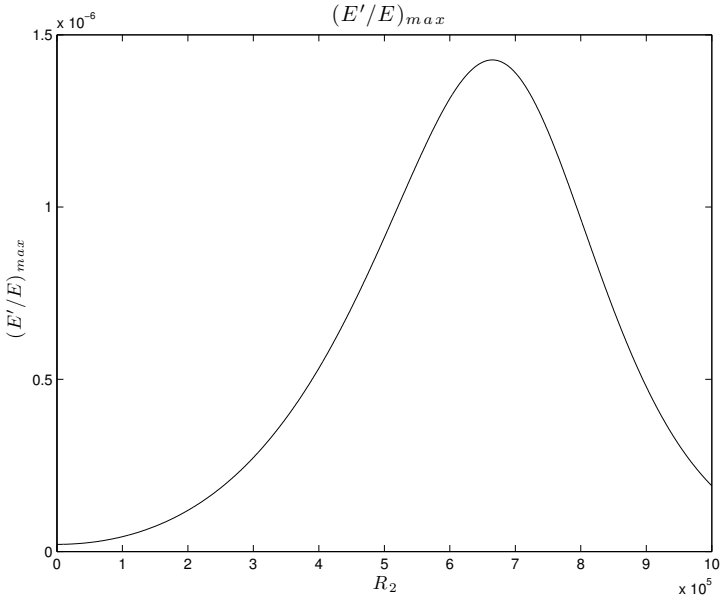

Figure 5.19: The Function $E'/E|_{max}$ from Run #3 - The dipole function $E'/E|_{max}$ from Run #3

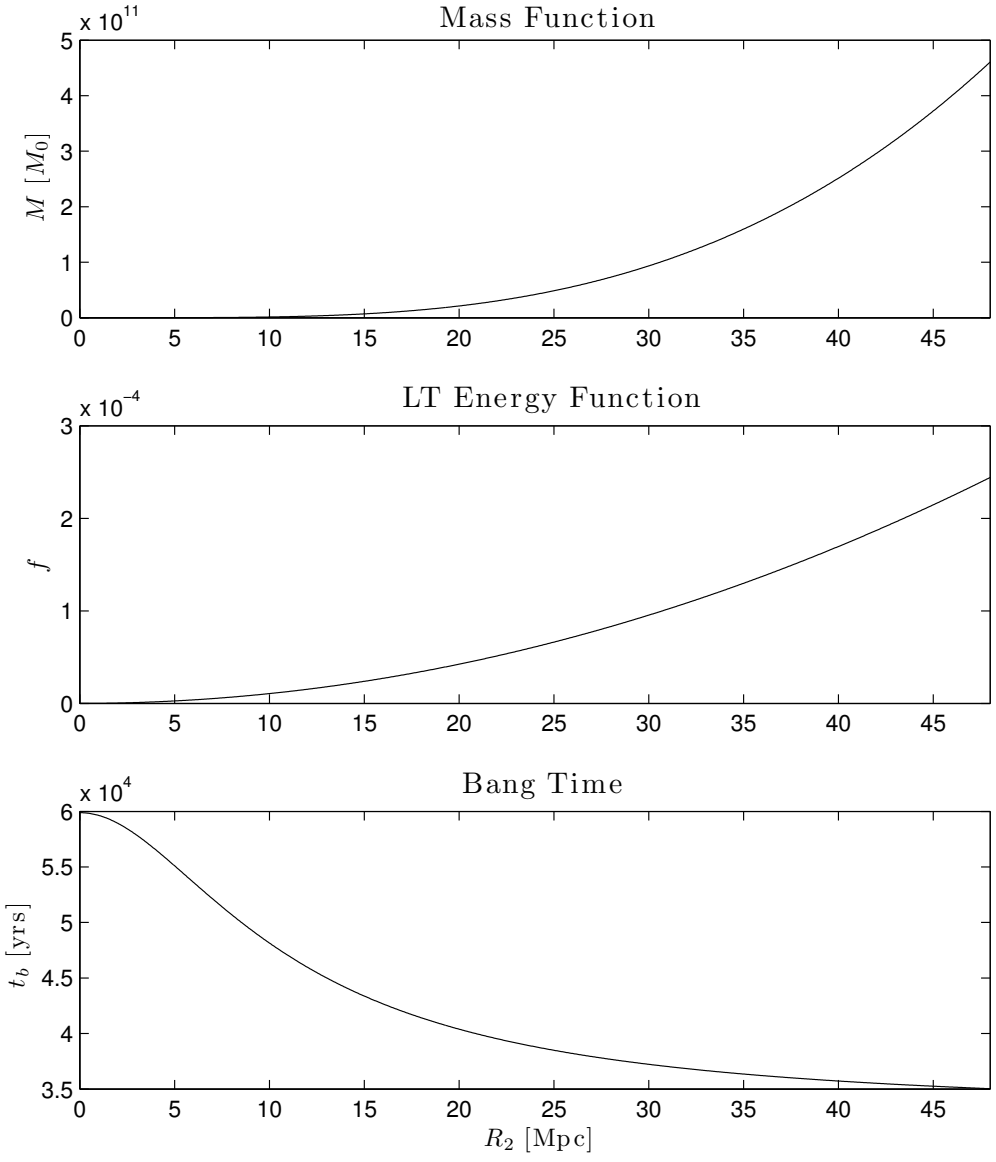

Figure 5.20: Arbitrary Functions M, f and t_b from Run #3 - The arbitrary functions which are common to both Szekeres and LT modes; M, f and t_b

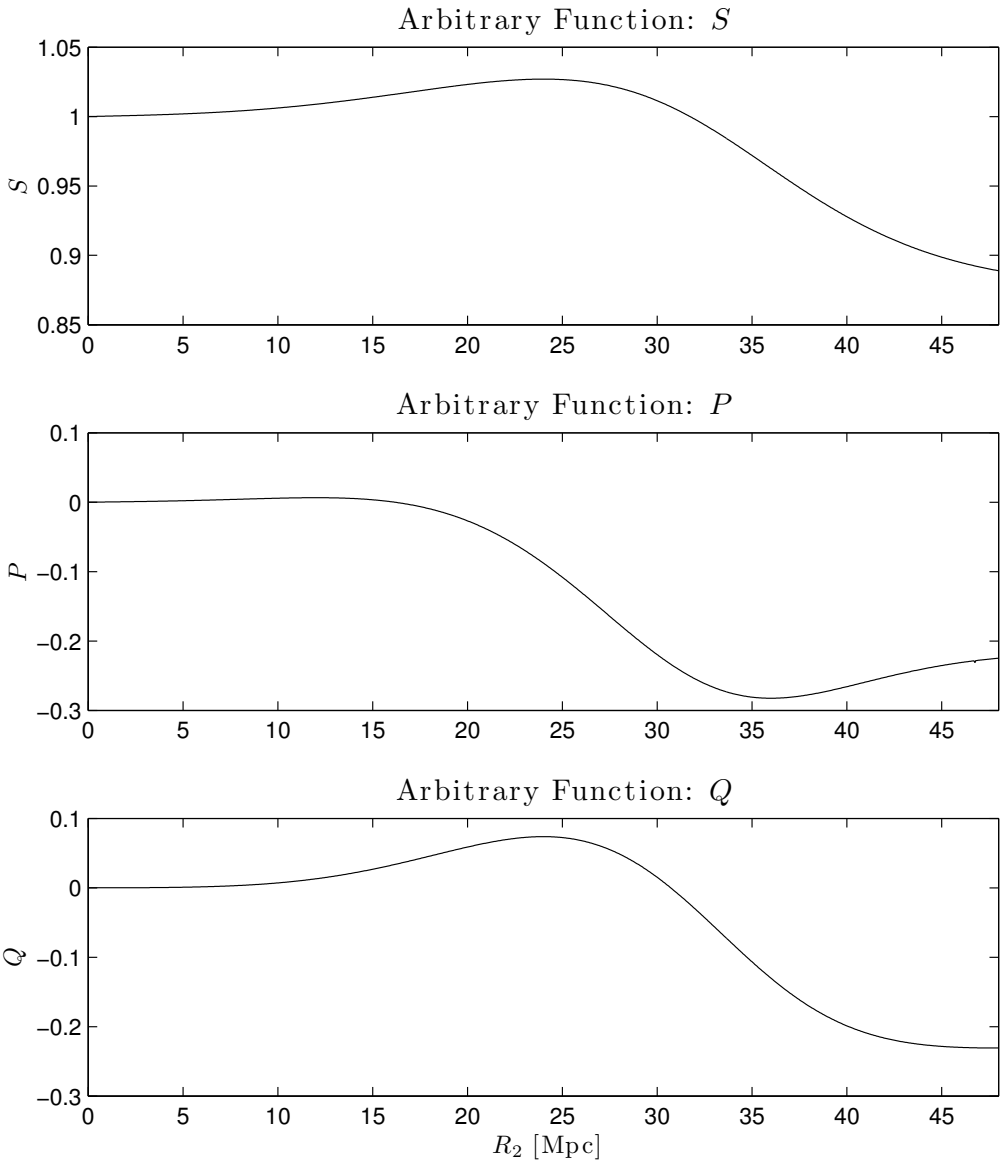

Figure 5.21: Arbitrary Functions S, P and Q from Run #3 - The arbitrary functions which are unique to Szekeres models; S, P and Q

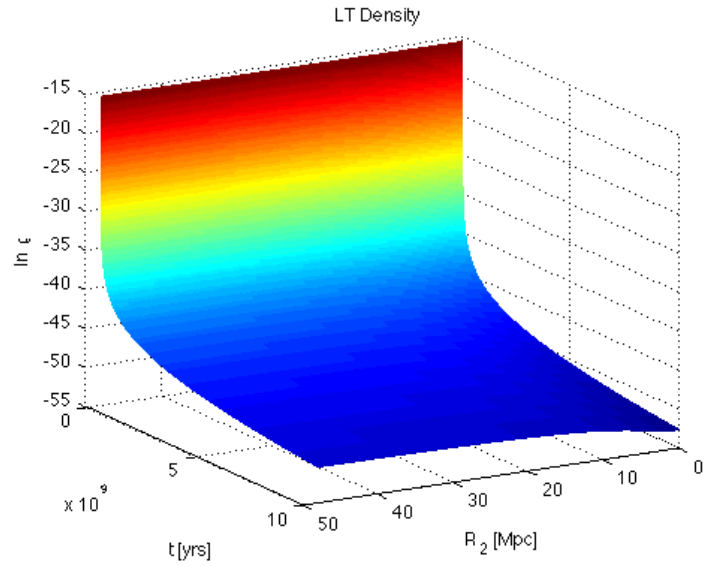

Figure 5.22: Evolution of the LT-density from Run #3 - The evolution of the LT-density profile, ρ_{LT}. Log scale

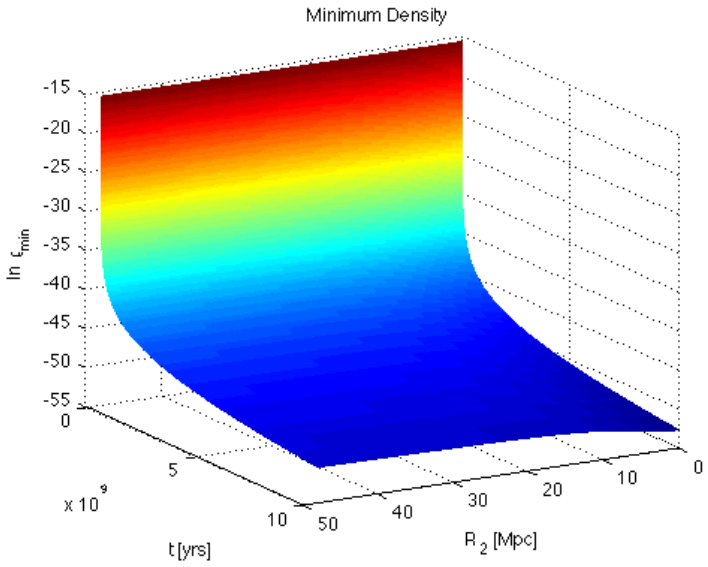

Figure 5.23: Density Dipole Minimum from Run #3 - The evolution of the density dipole minimum, ρ_{min}. Log scale

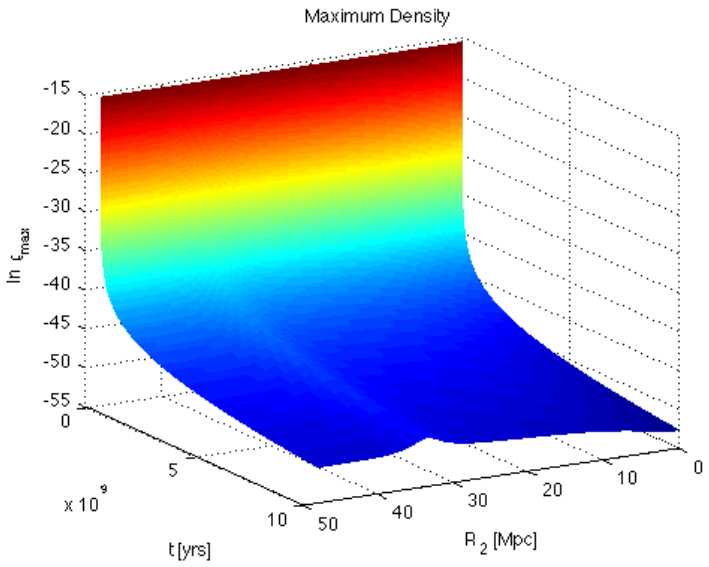

Figure 5.24: Density Dipole Maximum from Run #3 - The evolution of the density dipole maximum, ρ_{max}. Log scale

6

Conclusions

Modern cosmology, although having enjoyed a great number successes in the last century, is still faced with many open questions (e.g. the apparent dimming of distant supernovae). This has given rise to many highly speculative theories receiving much of the spotlight in recent years. While the importance of such research cannot be discounted, we should not loose sight of the full implications of the best current theory, GR. The consequences of the non-linearity of the EFE's have not yet been fully explored in cosmology, and, investigating exact solutions is an indispensable tool for doing this. In this respect, the Szekeres family of inhomogeneous solutions offers a wide range of possibilities for modelling cosmic structure. When attempting to construct a realistic model of the universe, or part thereof, it is of great utility to do so from physical quantities or data more directly accessible to observation than theoretical metric functions.

We considered quasispherical Szekeres models, outlining a model construction procedure using given density data at some initial and final time. These models are thought to be a sequence of non-concentric mass shells, each with density dipole. Consequently, the procedure requires one to specify 'radial' profiles of the equatorial density at the initial and final time, as well as dipole parameters (encoding the intensity and orientation), which we choose to do at the final time. Since, in Szekeres models, the dynamics of the areal radius is identical to that in LT models, the evolution of each shell can be determined by the equatorial density profiles, $\rho_{LT}(t_1, R)$ and $\rho_{LT}(t_2, R)$, as is in the case of LT models. We used a minor modification of the LT model construction

procedure of Krasinski & Hellaby to determine the arbitrary functions which are common to both - M, f and t_b. The dipole variations over each shell are encoded in the 'deviation function', $\mu(R)$, and the orientation angles, $\theta_{\rho_{min}}(R)$ and $\phi_{\rho_{min}}(R)$, of that minimum density. With knowledge of $\rho_{LT}(R)$ and $\mu(R)$ one can determine $\rho_{min}(R)$ and $\rho_{max}(R)$. For the determination of the metric functions unique to Szekeres models, S, P and Q, representing degrees of freedom pertaining to the dipole, we derive a new result - exact analytic expressions in terms of the dipole parameters, $\theta_{\rho_{min}}$, $\phi_{\rho_{min}}$ and $E'/E|_{max}$ (which is directly related to ρ_{min} and ρ_{LT}). So, by specifying the profiles $\rho_{LT}(t_1, R)$, $\rho_{LT}(t_2, R)$, $\mu(R)$, $\theta_{\rho_{min}}(R)$ and $\phi_{\rho_{min}}(R)$, and following the algorithm given in §4.5, one can determine the six arbitrary metric functions which completely define the Szekeres model. Special attention was paid to the origin limit of the dipole parameter E'/E, investigating the conditions which ensure it is finite and non-zero there. We corrected a claim made in previous literature that a maximum in E'/E corresponds to a density minimum (see Equation 69 in [46]) by showing that the derivative of the density with respect to E'/E is not always negative, but rather, it depends on the sign of $R'(\rho_{LT} - \rho_{AV})$. We found that a maximum in E'/E corresponds to a density minimum if $R'(\rho_{LT} - \rho_{AV}) < 0$, and density maximum if $R'(\rho_{LT} - \rho_{AV}) > 0$.

Using MATLAB, code was written to implement the procedure for determining these metric functions, as well as to simulate the model evolution. Since investigating elaborate models is beyond the scope of this work, we considered only three simple cases. All models spanned the time from recombination until the present, with the choice of initial density profile motivated by fluctuation consistent with CMB anisotropies. We then chose different profiles and orientation angles at the final time for each of the models. In all cases, when reconstructing the model evolution, the calculated metric functions reproduced the specified initial and final density profiles. In Runs #1 and #2 the initial and final profiles both have an over-density at the origin, causing the sign of $(\rho_{LT} - \rho_{AV})$ to be negative for all (t, r), and hence $E'/E|_{max}$ occurs at density minimum for all (t, r). In both cases, the deviation of ρ_{min} away from ρ_{LT} was much greater than that in ρ_{max}. In contrast, Run #3 had an initial over-density evolving into an under-density at the final time, which caused $(\rho_{LT} - \rho_{AV})$ to change sign during the course of the model evolution. Also, the deviation in ρ_{min} away from ρ_{LT}, at the final time, is much less than the deviation in ρ_{max}. The profile which shows the

biggest deviation away from ρ_{LT}, either ρ_{min} or ρ_{max}, seems to depend on the sign of $(\rho_{LT} - \rho_{AV})$.

In the future, plotting the density on constant time splices in rectangular coordinates will give one a better feel for the resulting spacetime. Since the constant-(t, r) mass shells are interpreted as being arranged non-concentrically, the distance from the origin to a given shell is not trivially related to areal radius, but instead, has (θ, ϕ) variations. Hence, plotting ρ_{min}, ρ_{max} and ρ_{LT} as a function of r, whatever one's choice for r may be, does not give one a sense of the density profile in any direction. In addition, the local (θ, ϕ) coordinates, which describe the dipole orientation on each shell, are not necessarily parallel. In order to understand the relationship between the coordinates on each shell some parallel transport operation may need to be performed. It is also foreseeable that, in the future, the model construction algorithm could be extended to include velocity profiles, as was done in [28] for the LT model.

Appendix A

MATLAB code

A.1 main.m

```
%   Specify all input density profiles and orientation angles in
%   input_profiles.m

%   Specify number of time steps
timesteps = 100;

%   Specify the range and resolution of R2
R_min = 0;
R_tot = 1;
R_length   = 501;
R2 = linspace(R_min, R_tot, R_length);

%   Load model specs from input_profiles.m
rho_LT2 = input_profiles(R2, 2);
rho_min2 = input_profiles(R2, 3);
theta_rho_min = input_profiles(R2, 4);
phi_rho_min = input_profiles(R2, 5);
R1_max = input_profiles(R2, 8);
t1 = input_profiles(R2, 9);
t2 = input_profiles(R2, 10);

%   Initialise vectors
R1_temp = linspace(R_min, R1_max, R_length);
t_vector = logspace(log10(t1), log10(t2), timesteps).';

%   Some constants
delta_t = t2 - t1;
delta_R = (R_tot - R_min)/R_length;
```

```
Rr2 = 1;
kappa = 8*pi;
S0 = 1;
x_tolerance = 1e-6;
t_tolerance = 1;
f_tolerance = 1e-3;

%   Initialise more empty vectors
type = '';
M = zeros(1, R_length);
M_temp = zeros(1, R_length);
ErErhomin1 = zeros(1, R_length);
tb = zeros(1, R_length);
f = zeros(1, R_length);
x = zeros(1, R_length);
S = zeros(1, R_length);
P = zeros(1, R_length);
Q = zeros(1, R_length);
a_mat = zeros(timesteps, R_length);

%   Integrate to get M(R2), and then R1(M)
for i = 1:R_length
    M(i) = quadgk(@fun2, R_min, R2(i));
    %M_temp(i) = quadgk(@fun1, R_min, R1_temp(i));
    %R1(i) = (quadgk(@fun1, M(1), M(i))).^(1/3);
end
for i = 1:length(R1_temp)
    M_temp(i) = quadgk(@fun1, R_min, R1_temp(i));
end

%   Interpolate R1 at the same M values as for R2
R1 = spline(M_temp, R1_temp, M);
rho_LT1 = input_profiles(R1, 1);
M_mat = ones(timesteps,1)*M;

%   Calculate a1, a2 and alpha
a1_temp = R1_temp./(M_temp.^(1/3));
a1_temp(1) = (6/(rho_LT1(1)*kappa))^(1/3);
a1 = spline(M_temp, a1_temp, M);
a2 = R2./(M.^(1/3));
a1(1) = (6/(rho_LT1(1)*kappa))^(1/3);
a2(1) = (6/(rho_LT2(1)*kappa))^(1/3);
Alpha = a1./a2;

%   Calculate borderlines for evolution types
```

```
Para = (sqrt(2)*a2.^(3/2)./3).*(1-Alpha.^(3/2));
Elip = (a2./2).^(3/2).*(pi - acos(1-2*Alpha)+2*sqrt(Alpha-Alpha.^2));

%   Determine evolution type. Solve phi(x)=0. Calculate f and tb
 for i = 1:R_length
%       Parabolic f=0
    if abs(delta_t - Para(i)) < t_tolerance
        type = [type 'p'];
        x(i) = solve_phi_x('p', a1(i), a2(i), delta_t, x_tolerance);
        f(i) = x(i)*M(i)^(2/3);
        tb(i) = t1 - (sqrt(2)/3)*a1(i)^(3/2)*(1-(3/20)*a1(i)*x(i)+(9/224)*(a1(i)*x(i))^2);

%       Elliptic f<0 and at maximum expansion at t=t2
    elseif abs(delta_t - Elip(i)) < t_tolerance
        type = [type 'm'];
        x(i) = solve_phi_x('m', a1(i), a2(i), delta_t, x_tolerance);
        f(i) = -x(i)*M(i)^(2/3);
        tb(i)= t1 - x(i)^(-3/2)*( acos(1-a1(i)*x(i)) - sqrt(1-(1-a1(i)*x(i))^2));

%       Hyperbolic f>0
    elseif delta_t < Para(i)
        type = [type 'h'];
        x(i) = solve_phi_x('h', a1(i), a2(i), delta_t, x_tolerance);
        f(i) = x(i)*M(i)^(2/3);
        tb(i)= t1 - x(i)^(-3/2)*(sqrt((1+a1(i)*x(i))^2-1) - acosh(1+a1(i)*x(i)));

%       Elliptic f<0 and still expanding at t=t2
    elseif delta_t > Para(i) && delta_t < Elip(i)
        type = [type 'x'];
        x(i) = solve_phi_x('x', a1(i), a2(i), delta_t, x_tolerance);
        f(i) = -x(i)*M(i)^(2/3);
        tb(i)= t1 - x(i)^(-3/2)*( acos(1-a1(i)*x(i)) - sqrt(1-(1-a1(i)*x(i))^2));

%       Elliptic f<0 and recollapsing at t=t2
    elseif delta_t > Elip(i)
        type = [type 'c'];
        x(i) = solve_phi_x('c', a1(i), a2(i), delta_t, x_tolerance);
        f(i) = -x(i)*M(i)^(2/3);
        tb(i)= t1 - x(i)^(-3/2)*( acos(1-a1(i)*x(i)) - sqrt(1-(1-a1(i)*x(i))^2));
    end
end

%   Calculate R' at t = t1 and t = t2
Rr1 = gradient(R1, R2);
%Rr2 = gradient(R2, M);
```

```
Mr = gradient(M, R2);

%   Calculate rho_AV at t = t1 and t = t2
rho_AV1_temp = 6*M_temp./(kappa.*R1_temp.^3);
rho_AV1_temp(1) = rho_LT1(1);
rho_AV1 = spline(M_temp, rho_AV1_temp, M);
rho_AV1(1) = rho_LT1(1);
rho_AV2 = 6*M./(kappa.*R2.^3);
rho_AV2(1) = rho_LT2(1);

%   Calculate E'/E|max (at t=t2)
temp2 = (rho_min2 - rho_LT2)./(rho_min2 - rho_AV2);
ErErhomin2 = ((rho_min2 - rho_LT2)./(rho_min2 - rho_AV2))./R2;
ErErhomin2(1) = input_profiles(R2, 6);
ErEmax = abs(ErErhomin2);
ErEmax_series = abs(input_profiles(R2, 7));

%   Caluclate the sign of R'(rho_LT - rho_AV) at t = t1 and t = t2
flip1 = sign(Rr1.*(rho_LT1 - rho_AV1));
flip2 = sign(Rr2.*(rho_LT2 - rho_AV2));

%   Calculate E'/E|max dipole orentation (at t=t2)
sin_theta_max = sin(theta_rho_min);
cos_theta_max = -cos(theta_rho_min).*flip2;
cos_theta_max(1) = -cos(theta_rho_min(1)).*flip2(2);
sin_phi_max = -sin(phi_rho_min).*flip2;
sin_phi_max(1) = -sin(phi_rho_min(1)).*flip2(2);
cos_phi_max = -cos(phi_rho_min).*flip2;
cos_phi_max(1) = -cos(phi_rho_min(1)).*flip2(2);

%   S, P and Q
[Rsol Ssol] = ode45(@(r2,s) myode(r2,s,R2,ErEmax.*cos_theta_max),R2,S0);
Sr = -ErEmax.*cos_theta_max;
Pr = -ErEmax.*cos_phi_max.*sin_theta_max.*Ssol';
Qr = -ErEmax.*sin_phi_max.*sin_theta_max.*Ssol';
for i= 1:R_length
    P(i) = quad(@(x)interp_func(Rsol, Pr, x),Rsol(1),Rsol(i));
    Q(i) = quad(@(x)interp_func(Rsol, Qr, x),Rsol(1),Rsol(i));
end

%   (E'/E)_max from S P Q
ErEmaxSPQ = sqrt(Sr.^2 + Pr.^2 + Qr.^2)./Ssol';
ErEmaxSPQ(1) = -flip2(2).*input_profiles(M, 6);
%ErEmaxSPQsol = sqrt(Sr.^2 + Pr.^2 + Qr.^2)./Ssol';
%ErErhominSPQ = -ErEmaxSPQ.*flip2;
```

```
%   Calculate rho_min at t = t1
%rho_min1 = (2*Mr - 6*M.*ErEmax)./(R1.^2.*Rr1 - (R1.^3).*ErEmax);
rho_min1 = rho_LT1 + (ErEmax.*(rho_LT1 - rho_AV1))./(Rr1./R1 - ErEmax);
rho_min1(1) = rho_LT1(1);
temp1 = (rho_min1 - rho_LT1)./(rho_min1 - rho_AV1);
%rho_min1SPQ = (2*Mr - 6*M.*ErErhominSPQ)./(R1.^2.*Rr1 - (R1.^3).*ErErhominSPQ);
rho_min1SPQ = rho_LT1 + (ErEmaxSPQ.*(rho_LT1 - rho_AV1))./(Rr1./R1 - ErEmaxSPQ);

%   Calculate rho_max at t = t1 and t = t2
rho_max1 = rho_LT1 -
((rho_min1 - rho_LT1).*(rho_LT1 - rho_AV1))./(2*rho_min1 - rho_AV1 - rho_LT1);
rho_max2 = rho_LT2 -
((rho_min2 - rho_LT2).*(rho_LT2 - rho_AV2))./(2*rho_min2 - rho_AV2 - rho_LT2);

%   Evaluate shell crossing conditions
fr = gradient(f, R2);
tbr = gradient(tb, R2);
scc1 = sign(Mr./(3*M) - ErEmax);
scc1SPQ = sign(Mr./(3*M) - ErEmaxSPQ);
scc2 = sign(fr./(2*f) - ErEmax);
scc2SPQ = sign(fr./(2*f) - ErEmaxSPQ);
scc3 = (2*pi*M./(-f).^(3/2)).*(Mr./M - 3*fr./(2*f)) + tbr;

for j = 1:R_length
    % for elliptic and recollapsing at t=t2
    if type(j) == 'c'
        eta = linspace(acos(1-a1(j)*x(j)), 2*pi - acos(1-a2(j).*x(j)), timesteps).';
        t = tb(j) + (eta - sin(eta))*x(j)^(-3/2);
        a = (1 - cos(eta))/x(j);
        a_mat(:,j) = spline(t, a, t_vector);

    % for elliptic and still expanding/max expansion at t=t2
    elseif (type(j) == 'x')||(type(j) == 'm')
        eta = linspace(acos(1-a1(j)*x(j)), acos(1-a2(j).*x(j)), timesteps).';
        t = tb(j) + (eta - sin(eta))*x(j)^(-3/2);
        a = (1 - cos(eta))/x(j);
        a_mat(:,j) = spline(t, a, t_vector);

    % for hyperbolic
    elseif type(j) == 'h'
        eta = linspace(acosh(a1(j).*x(j) + 1), acosh(a2(j).*x(j) + 1), timesteps).';
        t = tb(j) + (sinh(eta) - eta)*x(j)^(-3/2);
        a = (cosh(eta)-1)/x(j);
        a_mat(:,j) = spline(t, a, t_vector);
```

```
    %for parabolic
    elseif type(j) == 'p'
        delta_t_vec = t_vector - tb(j);
        a_mat(:,j) = (9/2)^(1/3)*(delta_t_vec).^(2/3).*(1 +
         (x(j)/20)*(6*deta_t_vec).^(2/3) - (3*x(j)^2/2800)*(6*delta_t_vec).^(4/3) +
         (23*x(j)^3/504000)*(6*delta_t_vec).^2);
    end
end

% Calculate the matrix quantities
rho_LT_mat = 1./(4*pi.*a_mat.^2.*(a_mat./3+M_mat.*(gradient(a_mat)./gradient(M_mat))));
R_mat = a_mat.*(M_mat.^(1/3));
Rr_mat = zeros(timesteps, R_length);
for j = 1:timesteps
    Rr_mat(j,:) = gradient(R_mat(j,:), R2);
end
ErEmax_mat = ones(timesteps,1)*ErEmax;
rho_AV_mat = 6*M_mat./(kappa*R_mat.^3);
flip_mat = -sign(Rr_mat.*(rho_LT_mat - rho_AV_mat));
rho_min_mat = rho_LT_mat +
(flip_mat.*ErEmax_mat.*(rho_LT_mat-rho_AV_mat))./(Rr_mat./R_mat-flip_mat.*ErEmax_mat);
rho_max_mat = rho_LT_mat +
(-flip_mat.*ErEmax_mat.*(rho_LT_mat-rho_AV_mat))./(Rr_mat./R_mat+flip_mat.*ErEmax_mat);
```

A.2 solve_phi_x.m

```
function x = solve_phi_x(type, a1, a2, delta_t, tolerance)
% Returns the solution to the equation phi(x)=0. The x value is determined
% by the bisection method.

if type == 'h'
    x_max = ((a2 - a1)/delta_t)^2;
else
    x_max = 2/a2;
end
x_min = 0;
x_g = (x_min + x_max)/2;

while abs(phi_x(type, a1, a2, delta_t, x_g)) > tolerance
    if phi_x(type, a1, a2, delta_t, x_g)*phi_x(type, a1, a2, delta_t, x_max) > 0
        x_max = x_g;
    else
        x_min = x_g;
```

```
    end
    x_g = (x_max - x_min)/2 + x_min;
end

x = x_g;
```

References

[1] R. V. Pound and G. A. Rebka, "Gravitational Red-Shift in Nuclear Resonance," *Physical Review Letters* **3** (Nov., 1959) 439–441. 1

[2] I. Shapiro, M. Ash, R. Ingalls, W. Smith, D. Campbell, *et al.*, "Fourth test of general relativity - new radar result," *Phys.Rev.Lett.* **26** (1971) 1132–1135. 1

[3] M. Kramer, I. H. Stairs, R. Manchester, M. McLaughlin, A. Lyne, *et al.*, "Tests of general relativity from timing the double pulsar," *Science* **314** (2006) 97–102, `arXiv:astro-ph/0609417 [astro-ph]`. 1

[4] A. Biswas and K. R. Mani, "Relativistic Perihelion Precession of Orbits of Venus and the Earth," `arXiv:0802.0176 [gr-qc]`. 1

[5] J. Weisberg, D. Nice, and J. Taylor, "Timing Measurements of the Relativistic Binary Pulsar PSR B1913+16," *Astrophys.J.* **722** (2010) 1030–1034, `arXiv:1011.0718 [astro-ph.GA]`. 1

[6] C. M. Will, *Theory and experiment in gravitational physics*. Cambridge University Press, 1993. 1

[7] H. Weyl., "Gravitation und Elektrizita t. Sitzungsber," *Preuss. Akad. d. Wiss. Teil* (1918) 465. 1

[8] T. Kaluza, "On the Problem of Unity in Physics," *Sitzungsber. Preuss. Akad. Wiss. Berlin (Math.Phys.)* **1921** (1921) 966–972. 1

[9] K. Akama, "An Early Proposal of 'Brane World'," *Lect.Notes Phys.* **176** (1982) 267–271, `arXiv:hep-th/0001113 [hep-th]`. 1

[10] M. V. E.S. Fradkin, "On the gravitational interaction of massless higher-spin fields," *Physics Letters B* **189** (1987) 89–95. 1

[11] R. P. Woodard, "Avoiding dark energy with 1/r modifications of gravity," *Lect.Notes Phys.* **720** (2007) 403–433, `arXiv:astro-ph/0601672 [astro-ph]`. 1

[12] T. Clifton, P. G. Ferreira, A. Padilla, and C. Skordis, "Modified Gravity and Cosmology," `arXiv:1106.2476 [astro-ph.CO]`. 1

[13] H. Stephani, D. Kramer, M. A. MacCallum, C. Hoenselaers, and E. Herlt, *Exact solutions of Einstein's field equations*. Cambridge University Press, 2nd ed., 2003. 1

[14] A. H. Guth, "The Inflationary Universe: A Possible Solution to the Horizon and Flatness Problems," *Phys.Rev.* **D23** (1981) 347–356. 1

[15] A. Liddle and D. Lyth, *Cosmological inflation and large-scale structure*. Cambridge University Press, 2000. 2

[16] K. Bolejko, A. Krasinski, C. Hellaby, and M.-N. Celerier, *Structures in the Universe by Exact Methods*. Cambridge Universiy Press, 2010. 2

[17] H. van Elst, C. Uggla, W. M. Lesame, G. F. Ellis, and R. Maartens, "Integrability of irrotational silent cosmological models," *Class.Quant.Grav.* **14** (1997) 1151–1162, `arXiv:gr-qc/9611002 [gr-qc]`. 3

[18] L. Bruna and J. Girbau, "Linearization stability of the Einstein equation for Robertson-Walker models I," *J.Math.Phys.* **40** (1999) 5117. 3

[19] L. Bruna and J. Girbau, "Linearization stability of the Einstein equation for Robertson-Walker models II," *J.Math.Phys.* **40** (1999) 5131. 3

[20] L. Bruna and J. Girbau, "Laplacian in the hyperbolic space H_n and linearization stability of the Einstein equation for Robertson-Walker models," *J.Math.Phys.* **46** (2005) 072501. 3

[21] G. Lemaître, "L'Univers en expansion," *Annales Soc. Sci. Brux.* **A53** (1933) 51. 3, 9

[22] G. Lemaître, "The expanding universe," *Gen.Rel.Grav.* **29** (1997) 641–680. 3, 9

[23] R. C. Tolman, "Effect of imhomogeneity on cosmological models," *Proc.Nat.Acad.Sci.* **20** (1934) 169–176. 3, 9

[24] H. Bondi, "Spherically symmetrical models in general relativity," *Mon.Not.Roy.Astron.Soc.* **107** (1947) 410–425. 3, 9

[25] G. Lemaître, "La formation des nebuleuses dans l'univers en expansion," *C.R.Acad.Sci.Paris* **196** (1933) no. 1085, 303. 3

[26] W. Bonnor, "Formation of the nebulae," *Z.Astrophys* **39** (1956) 143–159. 3

[27] A. Krasinski and C. Hellaby, "Structure formation in the Lemaitre-Tolman model," *Phys. Rev.* **D65** (2002) 023501, arXiv:gr-qc/0106096. 4, 9, 20, 21, 23, 26, 27, 49, 61, 68

[28] A. Krasinski and C. Hellaby, "More examples of structure formation in the Lemaitre-Tolman model," *Phys.Rev.* **D69** (2004) 023502, arXiv:gr-qc/0303016 [gr-qc]. 4, 9, 20, 91

[29] A. Krasinski and C. Hellaby, "Formation of a galaxy with a central black hole in the Lemaitre-Tolman model," *Phys.Rev.* **D69** (2004) 043502, arXiv:gr-qc/0309119 [gr-qc]. 4, 9, 20

[30] C. Hellaby and A. Krasinski, "Alternative methods of describing structure formation in the Lemaitre-Tolman model," *Phys.Rev.* **D73** (2006) 023518, arXiv:gr-qc/0510093 [gr-qc]. 4, 20

[31] K. Bolejko and C. Hellaby, "The Great Attractor and the Shapley Concentration," *Gen.Rel.Grav.* **40** (2008) 1771–1790, arXiv:astro-ph/0604402 [astro-ph]. 5, 9

[32] N. Mustapha and C. Hellaby, "Clumps into voids," *Gen.Rel.Grav.* **33** (2001) 455–477, arXiv:astro-ph/0006083 [astro-ph]. 5, 9, 14

[33] P. Szekeres, "A class of inhomogeneous cosmological models," *Comm. Math. Phys.* **41** (1975) 55–64. http://dx.doi.org/10.1007/BF01608547. 10.1007/BF01608547. 5, 29, 30

[34] W. Bonnor, A. Sulaiman, and N. Tomimura, "Szekeres's Space-Times Have No Killing Vectors," *Gen.Rel.Grav.* **8** (1977) 549–559. 5, 29

[35] J. Plebanski and A. Krasinski, *An introduction to general relativity and cosmology*. Cambridge Universiy Press, 2006. 6, 17, 19, 29, 41, 47

[36] A. Krasinski, *Inhomogeneous Cosmological Models*. Cambridge Universiy Press, 1997. 6, 9, 29, 41

[37] W. Bonnor, "Non-radiative solutions of Einstein's equations for dust," *Commun.Math.Phys.* **51** (1976) 191. 6

[38] W. Bonnor, "Do freely falling bodies radiate," *Nature* **263** (1976) 301. 6

[39] S. Goode and J. Wainwright, "Friedmann-like singularities in Szekeres' cosmological models," *Mon.Not.Roy.Astron.Soc.* **198** (1982) 83. 6

[40] S. Goode and J. Wainwright, "Singularities and evolution of the Szekeres cosmological models," *Phys.Rev.* **D26** (1982) 3315–3326. 6

[41] C. Hellaby, "The Null and KS Limits of the Szekeres Metric," *Class.Quant.Grav.* **13** (1996) 2537–2546. See corrections in W.B. Bonnor's review, Math.Rev.97:4592,1997. 6, 47

[42] M. Ishak and A. Peel, "The growth of structure in the Szekeres inhomogeneous cosmological models and the matter-dominated era," `arXiv:1104.2590 [astro-ph.CO]`. * Temporary entry *. 6

[43] N. Meures and M. Bruni, "Exact non-linear inhomogeneities in ΛCDM cosmology," *Phys.Rev.* **D83** (2011) 123519, `arXiv:1103.0501 [astro-ph.CO]`. 6

[44] J. D. Barrow and J. Stein-Schabes, "Inhomogeneous cosmologies with cosmological constant," *Phys.Lett.* **A103** (1984) 315. 6

[45] C. Hellaby and A. Krasinski, "Physical and Geometrical Interpretation of the $\epsilon \leq 0$ Szekeres Models," *Phys.Rev.* **D77** (2008) 023529, `arXiv:0710.2171 [gr-qc]`. 6, 37

[46] C. Hellaby and A. Krasinski, "You can't get through Szekeres wormholes: Or, regularity, topology and causality in quasispherical Szekeres models," *Phys.Rev.* **D66** (2002) 084011, arXiv:gr-qc/0206052 [gr-qc]. 6, 35, 39, 43, 45, 52, 90

[47] P. Szekeres, "Quasispherical Gravitational Collapse," *Phys.Rev.* **D12** (1975) 2941. 6, 29, 30, 41

[48] A. Krasinski and K. Bolejko, "Redshift propagation equations in the $\beta' \neq 0$ Szekeres models," *Phys.Rev.* **D83** (2011) 083503, arXiv:1007.2083 [gr-qc]. 6, 37

[49] K. Bolejko, "Structure formation in quasispherical Szekeres model," *Phys.Rev.* **D73** (2006) 123508, arXiv:astro-ph/0604490 [astro-ph]. 6, 37

[50] K. Bolejko, "Evolution of cosmic structures in different environments in the quasispherical Szekeres model," *Phys.Rev.* **D75** (2007) 043508, arXiv:astro-ph/0610292 [astro-ph]. 6, 37

[51] R. A. Sussman and K. Bolejko, "A Novel approach to the dynamics of Szekeres dust models," arXiv:1109.1178 [gr-qc]. 7

[52] J. Firouzjaee and R. Mansouri, "Asymptotically FRW black holes," *Gen.Rel.Grav.* **42** (2010) 2431–2452, arXiv:0812.5108 [astro-ph]. 9

[53] H. Sato and K.-i. Maeda, "The Expansion Law of the Void in the Expanding Universe," *Prog.Theor.Phys.* **70** (1983) 119–127. 9

[54] H. Iguchi, T. Nakamura, and K.-i. Nakao, "Is dark energy the only solution to the apparent acceleration of the present universe?," *Prog.Theor.Phys.* **108** (2002) 809–818, arXiv:astro-ph/0112419 [astro-ph]. 9

[55] D. J. Chung and A. E. Romano, "Mapping Luminosity-Redshift Relationship to LTB Cosmology," *Phys.Rev.* **D74** (2006) 103507, arXiv:astro-ph/0608403 [astro-ph]. 9

[56] H. Alnes and M. Amarzguioui, "The supernova Hubble diagram for off-center observers in a spherically symmetric inhomogeneous Universe," *Phys.Rev.* **D75** (2007) 023506, arXiv:astro-ph/0610331 [astro-ph]. 9

[57] K. Bolejko, "Supernovae Ia observations in the Lemaitre-Tolman model," *PMC Phys.* **A2** (2008) 1, arXiv:astro-ph/0512103 [astro-ph]. 9

[58] D. J. Raine and E. G. Thomas, "Large-scale inhomogeneity in the Universe and the anisotropy of the microwave background," *Mon. Not. Roy. Astr. Soc.* **195** (1981) 649–660. 9

[59] B. Paczynski and T. Piran, "A Dipole Moment of the Microwave Background as a Cosmological Effect," *Astrophys. J.* **364** (1990) 341–348. 9

[60] M. Panek, "Cosmic Background Radiation Anisotropies from Cosmic Structures: Models based on the Tolman Solution," *Astrophys. J.* **388** (1992) no. 225-233, . 9

[61] J.-P. Uzan, C. Clarkson, and G. F. Ellis, "Time drift of cosmological redshifts as a test of the Copernican principle," *Phys.Rev.Lett.* **100** (2008) 191303, arXiv:0801.0068 [astro-ph]. 9

[62] M. Araujo and W. Stoeger, "Obtaining the time evolution for spherically symmetric Lemaitre-Tolman-Bondi models given data on our past light cone," *Phys.Rev.* **D80** (2009) 123517, arXiv:0904.0730 [astro-ph.CO]. 9

[63] C. Hellaby, "Volume matching in tolman models," *General Relativity and Gravitation* **20** (1988) 1203–1217. http://dx.doi.org/10.1007/BF00756049. 10.1007/BF00756049. 9

[64] C. Hellaby, "Modelling Inhomogeneity in the Universe," *PoS* **ISFTG** (2009) 005, arXiv:0910.0350 [gr-qc]. 11, 14, 16, 17, 32, 35, 36

[65] C. Hellaby and K. Lake, "Shell crossings and the Tolman model," *Astrophys.J.* **290** (1985) 381. 13, 14, 16

[66] W. Bonnor, "Closed Tolman models of the Universe," *Class.Quant.Grav.* **2** (1985) 781–790. 13

[67] C. Hellaby and K. Lake, "The singularity of Eardley, Smarr and Christodoulou." Preprint 88/7, department of applied mathematics, university of cape town, 1988. 13

[68] A. Meszaros *Mon. Not. Roy. Astr Soc.* **253** (1991) 619. 14

[69] K. Schwarzschild, "Über das gravitationsfeld eines massenpunktes nach der einstein'schen theorie," *Sitzungsberichte der Königlich Preussischen Akademie der Wissenschaften* **1** (1916) 189–196. 18

[70] C. Hellaby, "A Kruskal-like model with finite density," *Class.Quant.Grav.* **4** (1987) 635–650. 18

[71] P. Vaidya, "The Gravitational Field of a Radiating Star," *Proc.Indian Acad.Sci.* **A33** (1951) 264. 18

[72] P. Vaidya, "Newtonian Time in General Relativity," *Nature* **171** (1953) 260–261. 18

[73] J. P. Lemos, "Naked singularities: Gravitationally collapsing configurations of dust or radiation in spherical symmetry. A Unified treatment," *Phys.Rev.Lett.* **68** (1992) 1447–1450. 18

[74] C. Hellaby, "On the Vaidya limit of the Tolman model," *Phys.Rev.* **D49** (1994) 6484, `arXiv:gr-qc/9907074 [gr-qc]`. 18

[75] R. Kantowski and R. Sachs, "Some spatially homogeneous anisotropic relativistic cosmological models," *J.Math.Phys.* **7** (1966) 443. 19

[76] C. Hellaby, "The nonsimultaneous nature of the Schwarzschild R=0 singularity," *J.Math.Phys.* **37** (1996) 2892. 19, 20

[77] B. Datt, "Über eine klasse von lösungen der gravitationsgleichungen der relativität," *Zeitschrift für Physik A Hadrons and Nuclei* **108** (1938) 314–321. `http://dx.doi.org/10.1007/BF01374951`. 10.1007/BF01374951. 20

[78] D. Szafron, "Inhomogeneous cosmologies: New exact solutions and their evolution," *J.Math.Phys.* **18** (1977) 1673–1677. 29

[79] O. Gron, "Isotropization and Homogenization of an Anisotropic and Inhomogeneous Cosmological Model During the Inflationary Era," *Phys.Rev.* **D32** (1985) 1586–1587. 37

[80] J. W. Moffat, "Inhomogeneous Cosmology, Inflation and Late-Time Accelerating Universe," `arXiv:astro-ph/0606124 [astro-ph]`. 37

[81] K. Bolejko and M.-N. Celerier, "Szekeres Swiss-Cheese model and supernova observations," *Phys.Rev.* **D82** (2010) 103510, arXiv:1005.2584 [astro-ph.CO]. 37

[82] M. Ishak, J. Richardson, D. Whittington, and D. Garred, "Dark Energy or Apparent Acceleration Due to a Relativistic Cosmological Model More Complex than FLRW?," *Phys.Rev.* **D78** (2008) 123531, arXiv:0708.2943 [astro-ph]. 37

[83] K. Bolejko, "The Szekeres Swiss Cheese model and the CMB observations," *Gen.Rel.Grav.* **41** (2009) 1737–1755, arXiv:0804.1846 [astro-ph]. 37

[84] K. Bolejko, "Volume averaging in the quasispherical Szekeres model," *Gen.Rel.Grav.* **41** (2009) 1585–1593, arXiv:0808.0376 [astro-ph]. 37

[85] A. Krasinski, "Geometry and topology of the quasi-plane Szekeres model," *Phys.Rev.* **D78** (2008) 064038, arXiv:0805.0529 [gr-qc]. 37

[86] M. M. de Souza, "Hidden symmetries of Szekeres quasi-spherical solutions," *Rev.Bras.Fis.* **15** (1985) 379. 41

[87] G. Ellis, "Dynamics of pressure free matter in general relativity," *J.Math.Phys.* **8** (1967) 1171–1194. 46